What do 3d-4f butterflies tell us?

Yan Peng [a,b,*], Annie K. Powell [a,b,c,*]

[a] Institute of Inorganic Chemistry, Karlsruhe Institute of Technology, Engesserstrasse 15, 76131 Karlsruhe, Germany
[b] Institute of Nanotechnology, Karlsruhe Institute of Technology, Postfach 3640, 76021 Karlsruhe, Germany
[c] Institute for Quantum Materials and Technologies, Karlsruhe Institute of Technology, Postfach 3640, 76021 Karlsruhe, Germany

ARTICLE INFO

ABSTRACT

The most studied examples of 3d-4f based single molecule magnets (SMMs) and their coordination cluster counterparts is that of the 3d-4f butterfly systems which provide a test-bed to facilitate the relevance of the 3d and 4f ions to the overall magnetic behavior of the molecules. This review examines the synthetic strategies used to obtain these butterfly molecules with a view to facilitate the design and synthesis of polynuclear 3d-4f clusters with different structures and enhanced SMM performance.

Contents

1. Introduction

Recently, the exploration of heterometallic *3d-4f* coordination clusters (CCs) has attracted intense attention because of their fascinating architectures and potential applications in various research fields including luminescence [1–3], catalysis [4,5], significant magneto-caloric effects [6–8] and single molecule magnetics (SMMs) [9–12]. The first studies of magnetism on *3d-4f* complexes were primarily focused on Cu[II]-Gd[III] clusters based on the pioneering work of Gatteschi and co-workers [13]. Subsequently, several *3d-4f* complexes were reported and in 2004, Matsumoto and coworkers successfully produced the first *3d-4f* SMM complex [Cu[II]TbL(hfac)$_2$]$_2$ (H$_3$L = 1-(2-hydroxybenzamido)-2-(2-hydroxy-3 -methoxy-benzylideneamino)-ethane) [14]. The success of this study revealed not only the nature of the Cu[II]-Ln ferromagnetic interaction but also the magnetic anisotropy of the system, demonstrating how a suitable molecular design can lead to the slow relaxation of the magnetisation at a molecular level, here with U_{eff} = 21 K and τ_0 = 2.7 × 10^{-8} s. Thus, the principle that *3d-4f* clusters could lead to SMMs was established.

To date, several synthetic strategies have been developed by chemists and many *3d-4f* coordination clusters with a diversity of nuclearities and topologies including ball, cage, disc, and wheel shape structures have been synthesized and their properties investigated [15].

Despite the fact that many *3d-4f* coordination clusters have been prepared, the directed development of *3d-4f* clusters with different nuclearities is still a challenge [16,17]. In fact, it is difficult to control the synthesis of *3d-4f* coordination clusters since the different coordination geometry preferences of *3d* and *4f* metal ions need to be taken into account. For example, *3d* metal ions tend to adopt coordination geometries largely steered by the influence of the interplay between electron configuration and the ligand field which mostly result in environments with coordination numbers of 4 to 7. On the other hand, for *4f* ions the concept of "ligand field stabilization" loses relevance and stable electronic ground states are generally directed through a balance of electrostatic and spin–orbit coupling effects. Marrying these different coordination preferences within a *3d-4f* coordination cluster requires taking these into account and adapting the synthetic strategies accordingly. A further aspect regards the nature of the cooperativity between the *3d* and *4f* ions. At least the existence of cooperativity can be established through removal and/or variation of the *3d* or *4f* ions and whether this makes a difference to the observed properties. In this review, we will concentrate on using the observed mag-

netic behavior to monitor this. In order to achieve these aims it is useful to develop and explore a large number of isostructural clusters to elucidate the nature of the *3d-4f* relationships amongst the resulting structures. Ultimately, if these relationships can be established it should be possible to synthesize target complexes showing specific properties, but clearly it is still a long journey towards this goal.

Although the magnetic properties of *3d-4f* clusters have been studied intensively, magneto-structural correlations have not yet been satisfactorily established. Establishing such correlations is regarded as the most useful way forward for constructing tailored *3d-4f* clusters showing improved magnetic properties. At present, *ab initio* calculations are widely regarded as a method of choice in providing some definitive answers. However, the fact that most of *3d-4f* systems comprise large numbers of unpaired electrons and that the *4f* ions are subject to large spin–orbit coupling effects places a significant hurdle to overcome in terms of using an *ab initio* approach. Some other physical measurement methods beyond standard magnetic measurements (dc and ac susceptibilities), such as EPR [18,19], Mössbauer [20], INS [21] and XMCD [22] spectroscopies have provided some useful insights which can also inform the results of such calculations. One factor which is becoming increasingly clear in the interplay between *3d* and *4f* ions is the importance of the dipolar fields which the *4f* ions can exert within the system as well as the extent of the *3d-4f* coupling which seems to affect the relative performance parameters of relaxation phenomena, usually gauged by Single Molecule Magnet behavior [23–25].

The {M$_2$Ln$_2$} butterfly family provides a useful test-bed system since a large number of examples are reported in the literature. In some cases the compounds are amenable to exploration using *ab initio* approaches along with some DFT treatments. These coordination clusters can have two arrangements [26]. **Type I** (see Fig. 1) has the *4f* (Ln) ions occupying the wingtip positions of the butterfly and the *3d* (M) ions the body, M-Ln coupling tends to steer the observed magnetic properties although the Ln single ion magnetics as well as the strength of any central M-M coupling balance this. This gives three different parameters in {(3d)$_2$Ln$_2$(μ$_2$-OR)$_4$(μ$_3$-OR′)$_2$} cores. When the central M is either diamagnetic or else not coupled to any significant extent to the *4f* ion we might expect the *4f* single ion properties to dominate the magnetism. When the *3d-4f* and *3d-3d* coupling parameters are present the system has to be treated as a cooperative entity. In addition, the role of the dipolar coupling and the relative anisotropies of the two types of ions must be considered. For the **Type II** case the M
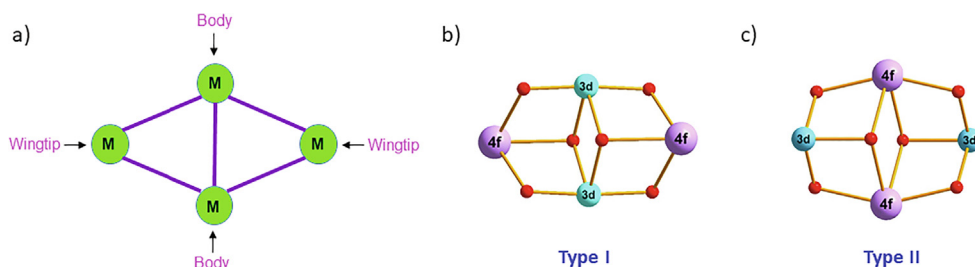
Fig. 1. The definition of the body and wingtip in butterfly M$_4$ cores (a); Ball and stick representation of the metal-oxo {(3d)$_2$Ln$_2$(μ$_2$-OR)$_4$(μ$_3$-OR′)$_2$} core of a 'defect dicubane' or 'butterfly' structure (b and c).

ions are at the wingtip positions and this effectively deletes the M-M interaction, but the M-Ln interaction as well as the single ion properties of the Ln ions are still relevant. Here we can expect the lanthanide single ion properties to dominate.

In this review, we have summarized and compared all the discrete *3d-4f* butterfly topology clusters showing slow relaxation of the magnetization (SMM properties) and wherever possible the isostructural analogues containing selective deletion of the *3d* or *4f* ions contribution through using diamagnetic ions. We hope that this summary will facilitate the design and synthesis of polynuclear *3d-4f* clusters with different structures and shed light on further rational design of better SMMs.

2. Scope of this review

The *3d-4f* butterfly cluster compounds in this review were identified by searching the CCDC database (web edition) in July 2019. The SMMs we consider are defined here as those *3d-4f* butterfly compounds showing slow relaxation and/or hysteresis loops in the magnetization. The specific case of {$Fe_2^{III}Ln_2$} butterfly SMMs has already been reviewed by us and will not discussed in detail here, but referred to where needed. Some of the SMMs discussed in this review are members of a family of isostructural compounds and do not necessarily have single crystal X-ray structural data deposited in the CCDC.

The supporting information contains the synthetic methodologies and a survey of the properties of *3d* and *4f* ions. Every compound described here has been subjected to a SHAPE [27–29] analysis to establish the best description of the coordination geometries of the metal ions.

3. Survey of *3d-4f* butterfly SMM complexes

The determination of the molecular structure of SMMs using single crystal X-ray diffraction measurements forms the basis for understanding the properties of SMMs. In this review we consider *3d-4f* butterfly compounds according to the position of the *3d* metal ions in the Periodic Table. Through gathering and comparing the fine tuning of complexes via subtle changes to the ligand field, we can begin to discover how to create SMMs by design rather than fortuity, at the same time trying to establish magneto-structural relationships within these molecules. Until recently it proved rather difficult to analyze compounds with such large Hilbert spaces using *ab initio* calculations, but now progress is being made in this area and available results will be discussed in the relevant sections. The analysis provided from *ab initio* calculations has been developed in accordance with the computational effort required for a given system. In order to assist the reader a summary of all the butterfly systems where *ab initio* calculations have been applied is given in Tables 2, 4 and 9 (also an overview in Table S9). The units for the result *J* values of calculations in the Tables 2, 4, 9 and Table S9 are cm^{-1}. As can be seen, for some systems broken symmetry DFT (BS-DFT) analysis, whereas for others just DFT approaches have been used. It can also be seen that *J* value contributions along with various versions of the spin Hamiltonian are suggested by several different groups. This makes comparison very tricky and it would be useful for a consensus to be formed. Tables 1, 3, 5, 6, 7, 8 and Tables S3–S8 list the selected structural features and parameters of *3d-4f* butterfly SMMs.

For research on potential SMMs two characterization techniques are of paramount importance. The first is single crystal X-ray

Table 1
Magnetic data and structural features of Cr^{III}-*4f* butterfly SMMs.

	Space group	Applied dc Field/ Oe	Relaxation processes					Ref
			Orbach		Raman	direct	QTM	
			U_{eff}/K (cm^{-1})	τ_0/s				
[Cr$_2^{III}$Dy$_2$(OMe)$_2$(mdea)$_2$ (O$_2$CPh)$_4$(NO$_3$)$_2$] **1**	P2$_1$/n	0	77 (ca. 54)	5.1 × 10^{-8}	–	–	–	[32]
[Cr$_2^{III}$Dy$_2$(OMe)$_2$(dea)$_2$ (O$_2$CPh)$_4$(MeOH)$_4$](NO$_3$)$_2$ **2**	P2$_1$/n	0	62.1 (43.2)	2.3 × 10^{-7}	–	–	–	[33]
[Cr$_2^{III}$Dy$_2$(OMe)(OH)(edea)$_2$ (O$_2$CPh)$_4$(NO$_3$)$_2$] **3**	P2$_1$/n	0	79.1 (55.0)	3.4 × 10^{-8}	–	–	–	[33]
[Cr$_2^{III}$Dy$_2$(OMe)$_2$(^{n}Budea)$_2$ (O$_2$CPh)$_4$(NO$_3$)$_2$] **4**	P2$_1$/n	0	61.6 (42.8)	1.1 × 10^{-7}	–	–	–	[33]
[Cr$_2^{III}$Dy$_2$(OMe)$_2$(teaH)$_2$ (O$_2$CPh)$_4$(NO$_3$)$_2$(MeOH)$_2$] **5**	P2$_1$/n	0	63.4 (44.1)	8.3 × 10^{-7}	–	–	–	[33]
[Cr$_2^{III}$Dy$_2$(OMe)$_2$(mdea)$_2$ (acac)$_4$(NO$_3$)$_2$] **6**	P-1	0	34.6 (24)	1.2 × 10^{-7}	–	–	–	[36]
[Cr$_2^{III}$Dy$_2$(OMe)$_2$(edea)$_2$ (acac)$_4$(NO$_3$)$_2$] **7**	P-1	0	41.6 (29)	9.2 × 10^{-8}	–	–	–	[36]
[Cr$_2^{III}$Dy$_2$(OMe)$_2$(^{n}Budea)$_2$ (acac)$_4$(NO$_3$)$_2$] **8**	P-1	0	37.5 (26)	3.1 × 10^{-7}	–	–	–	[36]
Cr$_2^{III}$Nd$_2$(OMe)$_2$(tea)$_2$ (O$_2$CPh)$_4$(NO$_3$)$_2$} **9**	P2$_1$/n	0	–	–	–	–	–	[37]
[Cr$_2^{III}$Tb$_2$(OMe)$_2$(mdea)$_2$ (O$_2$CPh)$_4$(NO$_3$)$_2$] **10**	P2$_1$/n	0	64 ± 1 (~44)	1.7 × 10^{-9}	–	–	–	[37]
[Cr$_2^{III}$Ho$_2$(OMe)$_2$(mdea)$_2$ (O$_2$CPh)$_4$(NO$_3$)$_2$] **11**	P2$_1$/n	0	52 ± 0.7 (~ 36)	1.1 × 10^{-9}	–	–	–	[37]
[Cr$_2^{III}$Er$_2$(OMe)$_2$(mdea)$_2$ (O$_2$CPh)$_4$(NO$_3$)$_2$] **12**	P2$_1$/n	0	–	–	–	–	–	[37]
[Cr$_2^{III}$Tb$_2$(OMe)$_{0.8}$(OH)$_{1.2}$ (mdea)$_2$(*o*-Cl-*p*,*m*-F-PhCO$_2$)$_4$ (NO$_3$)$_2$] **13**	P-1	0	63.3 (44)	7.7 × 10^{-9}	–	–	–	[41]
[Cr$_2^{III}$Dy$_2$(OMe)$_{1.4}$(OH)$_{0.6}$ (mdea)$_2$(*o*-Cl-*p*,*m*-F-PhCO$_2$)$_4$ (NO$_3$)$_2$] **14**	P-1	0	87.8 (61)	2.1 × 10^{-7}	–	–	–	[41]
[Cr$_2^{III}$Ho$_2$(OMe)$_{1.16}$(OH)$_{0.84}$ (mdea)$_2$(*o*-Cl-*p*,*m*-F-PhCO$_2$)$_4$ (NO$_3$)$_2$] **15**	P-1	0	51.8 (36)	6.8 × 10^{-9}	–	–	–	[41]
[Cr$_2^{III}$Dy$_2$(OMe)(OH) (^{t}Budea)$_2$(*p*-^{t}Bubenz)$_4$ (NO$_3$)$_2$] **16**	P-1	0	64.7 (45)	7.7 × 10^{-8}	–	–	–	[41]
[Cr$_2^{III}$Dy$_2$(OMe)$_2$(mdea)$_2$ (hfacac)$_6$] **17**	Pbca	0	41.7 (28.6)	1.6 × 10^{-7}	–	–	–	[43]

Lattice solvent molecules are not listed. – means multiple relaxation processes were not observed.

Table 2
The J values between paramagnetic centers obtained from theoretic calculation for {Cr$_2^{III}$Ln$_2$} system.

| | [Cr$_2^{III}$Dy$_2$(OMe)$_2$(O$_2$CPh)$_4$(mdea)$_2$(NO$_3$)$_2$] **1** | | | | [Cr$_2^{III}$Dy$_2$(OMe)$_2$(mdea)$_2$(acac)$_4$(NO$_3$)$_2$] **6** | | | |
| | Calculated | | Fitted | | Calculated | | Fitted | |
	J^{dip}	$J^{ex\,\ddagger}$	$J^{ex\,a}$	$J^{ex\,b}$	J^{dip}	$J^{ex\,\ddagger}$	$J^{ex\,a}$	$J^{ex\,b}$
$J_{Dy1-Dy1'}$	2.50	1.00	1.0	1.50	2.31	0.49	0.50	2.64
$J_{Cr1-Cr1'}$	0.34	0.12	0.10	0.12	0.01	0.04	0.04	0.03
$J_{Dy1-Cr1}$	5.20	26.0	20.50	20.30	0.45	11.27	11.25	11.24
$J_{Dy1-Cr1'}$	5.20	−32.5	17.00	16.70	0.43	8.35	8.35	8.33
	[Cr$_2^{III}$Dy$_2$(OMe)$_2$(edea)$_2$(acac)$_4$(NO$_3$)$_2$] **7**				[Cr$_2^{III}$Dy$_2$(OMe)$_2$(^{n}Budea)$_2$(acac)$_4$(NO$_3$)$_2$] **8**			
	Calculated		Fitted		Calculated		Fitted	
	J^{dip}	$J^{ex\,\ddagger}$	$J^{ex\,a}$	$J^{ex\,b}$	J^{dip}	$J^{ex\,\ddagger}$	$J^{ex\,a}$	$J^{ex\,b}$
$J_{Dy1-Dy1'}$	2.40	0.49	0.50	2.77	2.34	0.49	0.50	1.79
$J_{Cr1-Cr1'}$	0.01	0.01	0.01	0.02	0.01	0.05	0.05	0.06
$J_{Dy1-Cr1}$	0.46	11.83	11.85	11.83	0.45	10.55	10.55	10.48
$J_{Dy1-Cr1'}$	0.43	8.26	8.25	7.96	0.42	7.15	7.15	7.14

$\ddagger$ means BS-DFT.

$^a\hat{H} = \left(J_{dip}^{Dy1\ Dy1'} + J_{exch}^{Dy1\ Dy1'} \right)\hat{s}_{Dy1,Z}\hat{s}_{Dy1',Z}\ \left(J_{dip}^{Cr1\ Cr1'} + J_{exch}^{Cr1\ Cr1'} \right)S_{Cr1}S_{Cr1'}\ 3J_{dip}^{Cr1\ Cr1'}S_{Cr1,Z}S_{Cr1',Z}$
$J_{dip}^{Dy1\ Cr1}(1\ 3\cos^2\theta)\hat{s}_{Dy1,Z}S_{Cr1,Z}\ 3\sin\theta\cos\theta\hat{s}_{Dy1,Z}S_{Cr1,Y}\ J_{dip}^{Dy1'\ Cr1}(1\ 3\cos^2\theta)\hat{s}_{Cr1',Z}S_{Cr1,Z}+$
$3\sin\theta\cos\theta\hat{s}_{Cr1',Z}S_{Cr1,Y}\ J_{dip}^{Dy1\ Cr1'}(1\ 3\cos^2\theta)\hat{s}_{Dy1,Z}S_{Cr1',Z}\ 3\sin\theta\cos\theta\hat{s}_{Dy1,Z}S_{Cr1',y}\ J_{dip}^{Dy1'\ Cr1'}$
$\left[(1\ 3\cos^2\theta)\hat{s}_{Cr1',Z}S_{Cr1',Z} + 3\sin\theta\cos\theta\hat{s}_{Cr1',Z}S_{Cr1',y} \right]\ J_{exch}^{Dy1\ Cr1}\hat{s}_{Dy1,Z}S_{Cr1,Z}\ J_{exch}^{Dy1'\ Cr1}\hat{s}_{Dy1',Z}S_{Cr1,Z}\ J_{exch}^{Dy1\ Cr1'}\hat{s}_{Dy1,Z}S_{Cr1',Z}\ J_{exch}^{Dy1'\ Cr1'}\hat{s}_{Dy1',Z}S_{Cr1',Z}$ (eqn 1).
$J_{dip}^{Dy1\ Dy1'} = \mu_B^2 g_{Dy,Z}^2/R_{Dy1\ Dy1'}^3 ; J_{dip}^{Cr1\ Cr1'} = \mu_B^2 g_{Cr}^2/R_{Cr1\ Cr1'}^3 ; J_{dip}^{Dy_i\ Cr_i} = \mu_B^2 g_{Dy,Z}^2 g_{Cr}/R_{Dy_i\ Cr_i}^3$.
The dependence on the θ angle comes from the anisotropy of the dipolar magnetic interaction.

$^b\hat{H} =\ J_{Dy1\ Dy1'}\hat{s}_{Dy1,Z}\hat{s}_{Dy1',Z}\ J_{Dy1\ Cr1}\left(\hat{s}_{Dy1,Z}S_{Cr1,Z} + \hat{s}_{Dy1',Z}S_{Cr1',Z} \right)\ J_{Dy1\ Cr1'}\cdot$

$\left(\hat{s}_{Dy1,Z}S_{Cr1',Z} + \hat{s}_{Dy1',Z}S_{Cr1,Z} \right)\ J_{Cr1,Z\ Cr1',Z}S_{Cr1,Z}S_{Cr1',Z}$ (eqn 2).
$\hat{S}_{Dy}$ = ½, S_{Cr} = 3/2, The J constants from eqn (2) were calculated as combinations of the J^{ex} and J^{dip} parameters by fixing the angles θ in eqn (1).

Table 3
Magnetic data and structural features of Mn^{II,III}-4f butterfly SMMs.

| | Space group | Applied dc field/ Oe | Relaxation processes | | | | | Ref |
| | | | Orbach | | Raman | Direct | QTM | |
			U_{eff}/K (cm^{-1})	τ/s				
[Mn$_2^{II}$Tb$_2$(hmp)$_6$(NO$_3$)$_4$ (MeOH)$_2$] plus [Mn$_2^{II}$Tb$_2$(hmp)$_6$(NO$_3$)$_4$ (H$_2$O)$_2$] **18**	P-1	500	3.84* (2.67)	6.43 × 10^{-7*}	–	–	–	[44]
[Mn$_2^{II}$Dy$_2$(hmp)$_6$(NO$_3$)$_4$(MeOH)$_2$] plus [Mn$_2^{II}$Dy$_2$(hmp)$_6$(NO$_3$)$_4$(H$_2$O)$_2$] **19**	P-1	500	3.86* (2.67)	1.24 × 10^{-6*}	–	–	–	[44]
[Mn$_2^{II}$Dy$_2$(L2)$_4$(NO$_3$)$_2$ (DMF)$_2$] **20**	P-1	0	11* (7.6)	1.0 × 10^{-8*}	–	–	–	[45]
[NMe$_4$]$_2$[Mn$_2^{II}$Dy$_2$ (thme)$_2$(piv)$_4$(NO$_3$)$_4$] **21**	P2$_1$/c	0	15 (10.4)	3.2 × 10^{-7}	+	+	+	[46]
[Mn$_2^{III}$Ce$_2$(^{n}Budea)$_2$ (^{n}BudeaH)$_2$(piv)$_6$] **22**	P-1	0	–	–	–	–	–	[47]
[Mn$_2^{III}$Nd$_2$(^{n}Budea)$_2$ (^{n}BudeaH)$_2$(piv)$_6$] **23**	P-1	0	10 (6.95)	1.4 × 10^{-6}	–	–	–	[47]
[Mn$_2^{III}$Dy$_2$(OH)$_2$(NO$_3$)$_4$ (hmp)$_4$(H$_2$O)$_4$](NO$_3$)$_2$ **24**	C2/c	0	–	–	–	–	–	[48]
[Mn$_2^{III}$Tb$_2$(OH)$_2$(NO$_3$)$_4$ (hmp)$_4$(H$_2$O)$_4$](NO$_3$)$_2$ **25**	C2/c	0	–	–	–	–	–	[48]
[Mn$_2^{III}$Dy$_2$(dpm)$_6$ (MeO)$_6$] **26**	P-1	0	–	–	–	–	–	[49]
[Mn$_2^{III}$Tb$_2$(dpm)$_6$ (MeO)$_6$(MeOH)$_2$] **27**	P-1	0	–	–	–	–	–	[49]
[Et$_3$NH]$_2$[Mn$_2^{III}$Dy$_2$(O)$_2$ (piv)$_{10}$] **28**	P-1	0	29 (20.2)	4.6 × 10^{-6}	+	+	+	[50]
[Mn$_2^{III}$Dy$_2$(OH)$_2$(pdea)$_2$ (p-Me-PhCO$_2$)$_6$] **29**	P-1	0	19.32 (13.4)	5.64 × 10^{-8}	–	–	–	[24]

Lattice solvent molecules are not listed. + means multiple relaxation processes were observed but not analyzed. – means multiple relaxation processes were not observed.
* means the energy barriers obtained by fitting the equation bellow:
$\ln(\chi''/\chi') = \ln(\omega\tau_0) + U_{eff}/K_B T$ (eqn 3).

diffraction (SCXRD) in order to establish the molecular structure of the coordination cluster and the second bulk susceptibility studies which makes it possible to look for and assess any SMM properties. Whilst SCXRD has become a standard tool for coordination chemists, for the susceptibility work there are several potential pitfalls which have been noted over the years and we list these below.

1. Consistent sample preparation. Different groups have different preferences for preparing samples for measurement and use various means for holding the samples.

2. In the measurement of dc susceptibility saturation effects should be checked for by using different applied fields.
3. In magnetization measurements it is important to constrain the sample to avoid orientation effects which can lead to abnormally high values.
4. Allowances for small amounts of so-called "paramagnetic impurities" may need to be made. In many cases these are not impurities as such, but the result of uncompensated surface spins. These effects can look large for strongly antiferromagnetically coupled systems.

Table 4
The J values between paramagnetic centers obtained from theoretic calculation for {Mn$_2^{II,III}$Ln$_2$}, {Fe$_2^{III}$Dy$_2$}, {Co$_2^{II}$Dy$_2$} and {Ni$_2^{II}$Ln$_2$} systems.

Compounds	[Mn$_2^{II}$Dy$_2$(L2)$_4$(NO$_3$)$_2$(DMF)$_2$] 20 Fitted[c]	[Mn$_2^{III}$Dy$_2$(OH)$_2$(p-Me-PhCO$_2$)$_6$ (pdea)$_2$] 29 Fitted[d]	[Fe$_2^{III}$Dy$_2$(OH)$_2$(pdea)$_2$(p-Me-PhCO$_2$)$_6$] 37 Fitted[e]	Cr$_2^{III}$Dy$_2$(OH)$_2$(pdea)$_2$(p-Me-PhCO$_2$)$_6$]# Fitted[f]
J^{tot}_{3d-3d}	0.2	3.20	4.20	0.65
J^{ex}_{3d-3d}		2.10	3.00	0.50
J^{dip}_{3d-3d}		1.10	1.20	0.15
J^{tot}_{3d-Dy}	4.8	0.15	0.12	1.15
J^{ex}_{3d-Dy}		0.09	0.05	0.80
J^{dip}_{3d-Dy}		0.06	0.07	0.35
J^{tot}_{Dy-Dy}	5.5	0.035	0.060	0.405
J^{ex}_{Dy-Dy}		0.001	0.025	0.370
J^{dip}_{Dy-Dy}		0.036	0.035	0.035
zJ	–	–	–	0.045

	[Fe$_2^{III}$Dy$_2$(OH)$_2$ (teaH)$_2$(p-CN-PhCO$_2$)$_6$] 32		[Fe$_2^{III}$Dy$_2$(OH)$_2$ (teaH)$_2$(m-Me-PhCO$_2$)$_6$] 33		[Fe$_2^{III}$Dy$_2$(OH)$_2$ (teaH)$_2$(m-CN-PhCO$_2$)$_6$] 34		[Fe$_2^{III}$Dy$_2$(OH)$_2$ (teaH)$_2$(p-NO$_2$-PhCO$_2$)$_6$] 35		[Fe$_2^{III}$Dy$_2$(OH)$_2$ (teaH)$_2$(p-Me-PhCO$_2$)$_6$] 36	
	BS-DFT	Fitted[g]	BS-DFT	Fitted[g]	BS-DFT	Fitted[g]	BS-DFT	Fitted[g]	BS-DFT	Fitted[g]
$J_{Fe1-Fe1'}$	5.7	5.7	8.2	21.0 / 10*	8.6	8.6	6.3	6.3	8.8	14.0 / 9.5*
$J_{Fe1-Dy1}$	0.12	0.13	0.21	0.30 / 0.17*	0.31	0.31	0.088	0.0050	0.26	0.26 / 0.20*
$J_{Fe1-Dy1'}$	0.090	0.090	0.046	0.01 / 0.10*	0.17	0.17	0.11	0.0050	0.26	0.27 / 0.20*
$J_{Dy1-Dy1'}$	0.0067	0.0067	0.011	0.011 / 0.020*	0.024	0.024	0	0	0.011	0.010 / 0*
		Fitted[n]		Fitted[n]		Fitted[n]		Fitted[n]		Fitted[n]
J^{tot**}		0.035		0.02		0.03		0.61		0.65
J^{ising}		0.18		0.50		0.60		0		0
J^{dip}		0.53		0.48		0.57		0.61		0.65

	[Co$_2^{II}$Dy$_2$(L1)$_4$(NO$_3$)$_2$(THF)$_2$] 42	[Co$_2^{II}$Dy$_2$(L2)$_4$(NO$_3$)$_2$(DMF)$_2$] 45	[Ni$_2^{II}$Dy$_2$(H$_2$L4)$_2$(MeO)$_2$(MeCN)$_2$(NO$_3$)$_4$] 51		[Ni$_2^{II}$Tb$_2$(H$_2$L5)$_2$(MeO)$_2$(MeCN)$_2$(NO$_3$)$_4$] 52		[Ni$_2^{II}$Dy$_2$(H$_2$L5)$_2$(MeO)$_2$(MeCN)$_2$(NO$_3$)$_4$] 53	
	Fitted[h]	Fitted[i]	BS-DFT	Fitted[j]	Fitted[k]	BS-DFT	BS-DFT	Fitted[j]
J^{tot}_{3d-3d}	2.0	6.8	7.9	20.3	17.6	20.5	17.8	20.5
J^{tot}_{3d-Ln}	1.6	11.7	17.2	11.0	8.5	20.4	9.5	21.6
J^{tot}_{Ln-Ln}	–	2.0	4.7	7.1	5.3	6.8	4.9	5.7

\# means related compound for comparison. *A small rescaling of the experimental data is in principle justified given the possible experimental errors due to the absorption of solvent molecules or mass error. **Magnetic interactions between Dy^{III} corresponding to pseudospin of 1/2 of the ground KDs on the dysprosium sites.

[c] $\hat{H} = J^{tot}_{Dy1\ Dy2}\hat{s}_{Dy1}\hat{s}_{Dy2}\ J^{tot}_{Dy\ Mn}(\hat{s}_{Dy1}\hat{s}_{Mn1} + \hat{s}_{Dy1}\hat{s}_{Mn2} + \hat{s}_{Dy2}\hat{s}_{Mn1} + \hat{s}_{Dy2}\hat{s}_{Mn2})\ J^{tot}_{Mn\ Mn}\hat{s}_{Mn1}\hat{s}_{Mn2}$ (eqn 4).
$\hat{s}_{Dy} = ½, \hat{s}_{Mn} = 5/2, J^{tot} = J^{ex} + J^{dip}$.

[d] $\hat{H} = J^{tot}_{Dy1\ Dy2}\hat{s}_{Dy1}\hat{s}_{Dy2}\ J^{tot}_{Dy\ Mn}(\hat{s}_{Dy1}\hat{s}_{Mn1} + \hat{s}_{Dy1}\hat{s}_{Mn2} + \hat{s}_{Dy2}\hat{s}_{Mn1} + \hat{s}_{Dy2}\hat{s}_{Mn2})\ J^{tot}_{Mn\ Mn}\hat{s}_{Mn1}\hat{s}_{Mn2}$ (eqn 5)
$\hat{s}_{Dy} = ½, \hat{s}_{Mn} = 5/2, J^{tot} = J^{ex} + J^{dip}$

[e] $\hat{H} = J^{tot}_{Dy1\ Dy2}\hat{s}_{Dy1}\hat{s}_{Dy2}\ J^{tot}_{Dy\ Fe}(\hat{s}_{Dy1}\hat{s}_{Fe1} + \hat{s}_{Dy1}\hat{s}_{Fe2} + \hat{s}_{Dy2}\hat{s}_{Fe1} + \hat{s}_{Dy2}\hat{s}_{Fe2})\ J^{tot}_{Fe\ Fe}\hat{s}_{Fe1}\hat{s}_{Fe2}$ (eqn 6).
$\hat{s}_{Dy} = ½, \hat{s}_{Fe} = 5/2, J^{tot} = J^{ex} + J^{dip}$.

[f] $\hat{H} = J^{tot}_{Dy1\ Dy2}\hat{s}_{Dy1}\hat{s}_{Dy2}\ J^{tot}_{Dy\ Cr}(\hat{s}_{Dy1}\hat{s}_{Cr1} + \hat{s}_{Dy1}\hat{s}_{Cr2} + \hat{s}_{Dy2}\hat{s}_{Cr1} + \hat{s}_{Dy2}\hat{s}_{Cr2})\ J^{tot}_{Cr\ Cr}\hat{s}_{Cr1}\hat{s}_{Cr2}$ (eqn 7).
$\hat{s}_{Dy} = ½, \hat{s}_{Cr} = 3/2, J^{tot} = J^{ex} + J^{dip}$.

[g] $\hat{H} = J_{Dy1\ Dy1'}S_{Dy1}S_{Dy1'}\ J_{Dy1\ Fe1}(S_{Dy1}S_{Fe1} + S_{Dy1'}S_{Fe1'})\ J_{Dy1\ Fe1'}(S_{Dy1}S_{Fe1'} + S_{Dy1'}S_{Fe1})\ J_{Fe1\ Fe1'}S_{Fe1}S_{Fe1'}$ (eqn 8).
$S_{Dy} = 5/2$ and $S_{Fe} = 5/2$ $J^{tot} = J^{ex} + J^{dip}$.

[h] $\hat{H} = J_{Dy1\ Dy2}S_{Dy1}S\ J_{Dy\ Co}(S_{Dy1}S_{Co1} + S_{Dy1}S_{Co2} + S_{Dy2}S_{Co1} + S_{Dy2}S_{Co2})\ J_{Co\ Co}S_{Co1}S_{Co2}$ (eqn 9).
$S_{Dy} = 5/2$ and $S_{Co} = 3/2$.

[i] $\hat{H} = J^{tot}_{Dy1\ Dy2}\hat{s}_{Dy1}\hat{s}_{Dy2}\ J^{tot}_{Dy\ Co}(\hat{s}_{Dy1}\hat{s}_{Co1} + \hat{s}_{Dy1}\hat{s}_{Co2} + \hat{s}_{Dy2}\hat{s}_{Co1} + \hat{s}_{Dy2}\hat{s}_{Co2})\ J^{tot}_{Co\ Co}\hat{s}_{Co1}\hat{s}_{Co2}$ (eqn 10).
$\hat{s}_{Dy} = 1/2, \hat{s}_{Co} = 1/2\ J^{tot} = J^{ex} + J^{dip}$.

[j] $\hat{H} = J^{tot}_{Dy\ Dy}\hat{s}_{Dy1}\hat{s}_{Dy2}\ J^{tot}_{Dy\ Ni}(\hat{s}_{Dy1}\hat{s}_{Ni1} + \hat{s}_{Dy1}\hat{s}_{Ni2} + \hat{s}_{Dy2}\hat{s}_{Ni1} + \hat{s}_{Dy2}\hat{s}_{Ni2})\ J^{tot}_{Ni\ Ni}\hat{s}_{Ni1}\hat{s}_{Ni2}$ (eqn 11).
[k] $\hat{H} = J^{tot}_{Tb\ Tb}\hat{s}_{Tb1}\hat{s}_{Tb2}\ J^{tot}_{Tb\ Ni}(\hat{s}_{Tb1}\hat{s}_{Ni1} + \hat{s}_{Tb1}\hat{s}_{Ni2} + \hat{s}_{Tb2}\hat{s}_{Ni1} + \hat{s}_{Tb2}\hat{s}_{Ni2})\ J^{tot}_{Ni\ Ni}\hat{s}_{Ni1}\hat{s}_{Ni2}$ (eqn 12).
$\hat{s}_{Tb} = 1/2, \hat{s}_{Ni} = 1, J^{tot} = J^{ex} + J^{dip}$.

[n] $\hat{H} = J^{tot}_{Dy\ Dy}\hat{s}_{Dy1}\hat{s}_{Dy2}$ (eqn 13).
$\hat{s}_{Dy} = 1/2, J^{tot} = J^{ising} + J^{dip}$.

5. The type of magnetometer used may make a difference for certain measurements, for example the available frequency range for ac measurements.
6. If hysteresis measurements are possible on the bulk sample, care needs to be taken in terms of the sweep rate used.

The standard practice in handling data is to produce χT vs T plots and magnetization isotherms taken over 3 temperatures, usually 2 K, 3 K and 5 K. It can be useful to also look at χ vs T plots to identify the presence of paramagnetic impurities. For dynamic behaviour investigated using ac susceptibility measurements both temperature and frequency dependent data provide useful information.

Analysis of the ac data gives a means to explore the slow relaxation of the magnetization. Historically this led to the idea of using an Arrhenius fitting of data-points corresponding to the positions of the maxima in the out-of-phase data according to the equation:

Table 5
Magnetic data and structural features of Fe^{III}-4f butterfly SMMs.

	Space group	Applied dc field/Oe	Relaxation processes					Ref
			Orbach		Raman	Direct	QTM	
			U_{eff}/K (cm^{-1})	τ_0/s				
[Fe$^{III}_2$Ho$_2$(OH)$_2$(teaH)$_2$(PhCO$_2$)$_4$(NO$_3$)$_2$] **30**	P-1	–	–	–	–	–	–	[52]
[Fe$_2^{III}$Dy$_2$(OH)$_2$(teaH)$_2$(PhCO$_2$)$_6$] **31**	C2/c	1500	16.2 (11.3)	1.9 × 10^6	–	–	–	[53]
[Fe$_2^{III}$Dy$_2$(OH)$_2$(teaH)$_2$(p-CN-PhCO$_2$)$_6$] **32**	P2$_1$/c	0	8 (5.6)	7.68 × 10^6	–	–	–	[54]
		1000	13 (9.0)	2.71 × 10^6	–	–	–	
[Fe$_2^{III}$Dy$_2$(OH)$_2$(teaH)$_2$(m-Me-PhCO$_2$)$_6$] **33**	P2$_1$/c	1500	21.2 (14.7)	5.15 × 10^7	–	–	–	[54]
[Fe$_2^{III}$Dy$_2$(OH)$_2$(teaH)$_2$(m-CN-PhCO$_2$)$_6$] **34**	P-1	1000	22.8 (15.8)	1.28 × 10^6	–	–	–	[54]
		2000	6.3 (4.4)	3.02 × 10^5	–	–	–	
[Fe$_2^{III}$Dy$_2$(OH)$_2$(teaH)$_2$(p-NO$_2$-PhCO$_2$)$_6$] **35**	P-1	0	–	–	–	–	–	[54,55]
[Fe$_2^{III}$Dy$_2$(OH)$_2$(teaH)$_2$(p-Me-PhCO$_2$)$_6$] **36**	P-1	1000	24 (16.7)	1.71 × 10^7	–	–	–	[54,55]
[Fe$_2^{III}$Dy$_2$(OH)$_2$(pdea)$_2$(p-Me-PhCO$_2$)$_6$] **37**	C2/c	1000	16.2 (11.5)	2.60 × 10^6	–	–	–	[25]
[Fe$_2^{III}$Er$_2$(OH)$_2$(pdea)$_2$(p-Me-PhCO$_2$)$_6$] **38**	C2/c	1000	16.5 (11.5)	2.03 × 10^7	–	–	–	[23]
[Fe$_2^{III}$Dy$_2$(OH)$_2$(teg)$_2$(N$_3$)$_2$(PhCO$_2$)$_4$] **39**	P-1	0	–	–	–	–	–	[56]
[Fe$_2^{III}$Dy$_2$(OH)$_2$(dda)$_2$(Hpdf)$_2$(NO$_3$)$_4$(H$_2$O)$_{1.5}$(MeOH)$_{0.5}$] **40**	P2$_1$/n	0	–	–	–	–	–	[57]

Lattice solvent molecules are not listed. – means multiple relaxation processes not observed.

Table 6
Magnetic data and structural features of Co^{II}-4f butterfly SMMs.

	Space group	Applied dc field/Oe	Relaxation processes					Ref
			Orbach		Raman/ S^{-1}K^{-n}	Direct	QTM/ s	
			U_{eff}/K (cm^{-1})	τ_0/s				
[Co$_2^{II}$Gd$_2$(OH)$_2$(ovan)$_4$(NO$_3$)$_4$]·(C$_3$H$_6$O) **41**	P-1	–	–	–	–	–	–	[58]
[Co$_2^{II}$Dy$_2$(L1)$_4$(NO$_3$)$_2$(THF)$_2$] **42**	P-1	0	15.8 (11.0) and 118.1 (82.1)	7.7 × 10^4 and 6.2 × 10^7	–	–	–	[59]
[Co$_2^{II}$Dy$_2$(L1)$_4$(NO$_3$)$_2$(MeOH)$_2$] **43**	P2$_1$/c	0	17.9 (12.4) and 104.8 (72.8)	2.3 × 10^4 and 9.2 × 10^7	–	–	–	[60]
[Co$_2^{II}$Dy$_2$(L1)$_4$ (NO$_3$)$_2$(DMF)$_2$] **44**	P2$_1$/c	0	17.5 (12.2) and 94.5 (65.7)	1.5 × 10^4 and 1.2 × 10^6	–	–	–	[60]
[Co$_2^{II}$Dy$_2$(L2)$_4$(NO$_3$)$_2$(DMF)$_2$] **45**	P-1	0	88.8 (61.7) 125.1$^\epsilon$ (86.8)	2.29 × 10^6 2.67 × 10$^{6\epsilon}$	C = 0.301 n = 3.16	–	1000	[45]
[^{i}Pr$_2$NH$_2$]$_2$ [Co$_2^{II}$Dy$_2$(OH)$_2$(Piv)$_{10}$] **46**	P-1	0	–	–	–	–	–	[50]

Lattice solvent molecules are not listed. – means multiple relaxation processes were not observed. $^\epsilon$ fitted only Orbach process.

$$\tau^{-1} = \tau_0^{-1}\exp\left(\frac{-U_{eff}}{k_BT}\right) \qquad (eqn14)$$

Here, τ_0 is pre-exponential factor and k_B is Boltzmann's constant.

Many of the examples discussed here have been analyzed in this way. In more recent times, researchers have favoured using an equation which takes other relaxation processes into account:

$$\tau^{-1} = \frac{B_1}{1 + B_2H^2} + A_1H^mT + CT^n + \tau_0^{-1}\exp\left(\frac{-U_{eff}}{k_BT}\right) \qquad (eqn15)$$

The terms represent the QTM, direct, Raman and Orbach contributions to the relaxation time, respectively [30].

The drawback of this equation is the large number of parameters.

A further analytical tool used is to construct an Argand diagram, which is often called a Cole-Cole plot by the community [31], plotting the in-phase (χ') versus out-of-phase (χ'') data (real vs imaginary). If such a plot is analyzed using a generalized Debye model the deviation of the parameter α from the ideal value of 0 gives an indication of whether more than one relaxation process is in operation.

3.1. 3d (paramagnetic)-4f systems

3.1.1. {Cr$_2^{III}$Ln$_2$} systems

The Murray group reported the first Cr^{III}-4f butterfly SMM of **Type II** in 2013 [32], with formula [Cr$_2^{III}$Dy$_2$(OMe)$_2$(O$_2$CPh)$_4$(mdea)$_2$(NO$_3$)$_2$] **1** (see Fig. 2), which was synthesized by the reaction of Dy(NO$_3$)$_3$·6H$_2$O and CrCl$_3$·6H$_2$O with mdeaH$_2$ (N-methyldiethanolamine), benzoic acid and Et$_3$N in acetonitrile.

This compound crystallizes in the monoclinic space group P2$_1$/n. The {Cr$_2^{III}$Dy$_2$} molecule displays a planar butterfly topology of **Type II**, bridged by two μ_3-OMe ligands (see Fig. 2). Around the periphery of the cluster, two doubly deprotonated mdea^{2-} ligands displaying a

Table 7
Magnetic data and structural features of Ni^{II} and Cu^{II}-$4f$ butterfly SMMs.

	Space group	Applied dc field/Oe	Relaxation processes		Raman	Direct	QTM	Ref
			U_{eff} /K(cm^{-1})	τ_0/s				
$[Ni^{II}_2Dy_2(L1)_4(NO_3)_2(DMF)_2]$ **47**	$P2_1/n$	0	18.5 (12.9)	5.4×10^{-7}	–	–	–	[61]
$[Ni^{II}_2Dy_2(L1)_4(NO_3)_2(MeOH)_2]$ **48**	$P2_1/c$	0	21.3 (14.8)	1.5×10^{-6}	–	–	–	[61]
		4000	28.5 (19.8)	2.8×10^{-6}	–	–	–	
$[Ni^{II}_2Tb_2(L1)_4(NO_3)_2(DMF)_2]$ **49**	$P2_1/c$	–	–	–	–	–	–	[61]
$[Ni^{II}_2Dy_2(L2)_4(NO_3)_2(H_2O)_2]$ **50**	P-1	0	36.0 (25)	8×10^{-8}	–	–	–	[62]
$[Ni^{II}_2Dy_2(H_2L4)_2(MeO)_2(MeCN)_2(NO_3)_4]$ **51**	$P2_1/n$	0	48.5 (33.7)	3.6×10^{-8}	–	–	–	[63]
$[Ni^{II}_2Tb_2(H_2L5)_2(MeO)_2(MeCN)_2(NO_3)_4]$ **52**	P-1	0	86.8 (60.3)	2.3×10^{-7}	–	–	–	[63]
$[Ni^{II}_2Dy_2(H_2L5)_2(MeO)_2(MeCN)_2(NO_3)_4]$ **53**	P-1	0	57.0 (39.6)	3.3×10^{-8}	–	–	–	[63]
$[Et_3NH_2]_2[Ni^{II}_2Dy_2(OH)_2(Piv)_{10}]$ **54**	$C2/c$	0	20 (13.9)	6×10^{-7}	+	+	+	[50]
$[Et_3NH_2][Ni^{II}_2Er_2(OH)_2(Piv)_{10}]$ **55**	$C2/c$	1000	12 (8.3)	5×10^{-6}	+	+	+	[50]
$[^iPr_2NH_2]_2[Cu^{II}_2Dy_2(OH)_2(Piv)_{10}]$ **56**	P-1	–	–	–	–	–	–	[50]
$[^iPr_2NH_2]_2[Cu^{II}_2Er_2(OH)_2(Piv)_{10}]$ **57**	P-1	–	–	–	–	–	–	[50]
$[Cu^{II}_2Dy_2(OMe)_2(HL6)_2(NO_3)_4]$ **58**	$P2_1/n$	1500	16.5 (11.5)	4.5×10^{-7}	–	–	–	[64]

Lattice solvent molecules are not listed. + means multiple relaxation processes were observed but not analyzed. – means multiple relaxation processes were not observed.

μ_3-η^2:η^1:η^2 coordination mode chelate and bridge within the $\{Cr^{III}_2Dy_2\}$ core (Scheme S2). There are four bridging benzoate ligands connecting the outer Cr^{III} to the inner Dy^{III} ions and two chelating nitrates coordinate to each of the two Dy^{III} ions. Thus, the two Cr^{III} ions are six coordinate displaying octahedral geometry and the two Dy^{III} ions are eight coordinate displaying square anti-prismatic geometry (Table S3 for the estimated deviations for the idealized geometries).

The compound is described as showing ferrimagnetic coupling between the paramagnetic centers. Classic SMM behavior was observed with maxima in the out-of-phase ac susceptibilities versus temperature and frequency plots (Fig. 3) from which U_{eff} = 77 K (53.5 cm^{-1}) and τ_0 = 5.1 × 10^{-8} s were extracted (Fig. 4) using the Arrhenius law, which is linear over whole temperature range studied. This along with the small values and range from the fitting of the Cole-Cole plots suggest a single Orbach relaxation process (Fig. 4). Furthermore, magnetic hysteresis loops open up to ~ 3.5 K with wide coercive field of H_{dc} = 2.7 T at 1.8 K and were observed using sweep rates of 0.003 T s^{-1} (Fig. 4). *Ab initio* calculations reveal that the relatively long relaxation times originate from the fact that there are stronger antiferromagnetic interactions (J_{Cr-Dy} = −20.30 cm^{-1} and −16.7 cm^{-1}) than usually found between the Cr^{III} and Dy^{III} ions (Table 2). This gives a useful indication that increasing exchange coupling between $3d$ and $4f$ ions can help to slow down the usually very fast relaxation of $4f$ ions.

In order to investigate the effect of the organic ligand field on the properties of the $\{Cr^{III}_2Dy_2\}$ butterfly system, four related $\{Cr^{III}_2Dy_2\}$ complexes with formulae: $[Cr^{III}_2Dy_2(OMe)_2(O_2CPh)_4(dea)_2 (MeOH)_4](NO_3)_2$ **2**, $[Cr^{III}_2Dy_2(OMe) (OH)(O_2CPh)_4(edea)_2(NO_3)_2]$· $MeOH·Et_2O$ **3**, $[Cr^{III}_2Dy_2(OMe)_2(O_2CPh)_4(^nBudea)_2(NO_3)_2]$ **4** and $[Cr^{III}_2Dy_2(OMe)_2(O_2CPh)_4(teaH)_2(NO_3)_2(MeOH)_2]$ **5** were prepared by the same group. The effect arising from changes in R of the R-deaH$_2$ ligand (functionalized diethanolamine ligands, where R is H, diethanolamine (deaH$_2$), CH_3CH_2, *N*-ethyldiethanolamine (edeaH$_2$), $CH_3CH_2CH_2$ *N*-butyldiethanolamine (^{n}BudeaH$_2$), or $HOCH_2CH_2$, triethanolamine (teaH$_3$)) could thus be explored [33].

All four complexes crystallize isostructurally in the same monoclinic space group $P2_1/n$ as compound **1** and the $\{Cr^{III}_2Dy_2\}$ cores have the same planar **Type II** butterfly motif (see Fig. 5). Apart from

the differences introduced by changing R in the main ligand, in complex **3** the two bridging μ_3-OMe ligands are now a 1:1 mixture of μ_3-OH and μ_3-OMe ligands. A further variation is that the terminal ligands on the Dy^{III} ions are different. A single chelating NO_3^- is found for **3** as well as **4**, as was the case for compound **1**. However, for compound **2**, two MeOH molecules occupy the two oxygen sites taken by the chelating nitrate which results in two nitrate counterions being present in the lattice to balance the charge. In compound **5**, a monodentate NO_3^- and a MeOH occupy these sites on the Dy (Fig. 5). All the Cr^{III} ions and Dy^{III} ions display distorted octahedral geometry and distorted square anti-prismatic geometries, respectively (Table S3 for the estimated deviations for the idealized geometries).

Dc susceptibility measurements for all four complexes show similar behavior in χT vs T to that observed for compound **1**, but with a steeper decrease at low temperature for complex **3**, suggesting that the antiferromagnetic interactions are stronger between the Cr^{III} and Dy^{III} ions compared with **1**, **2**, **4**, and **5**. All four compounds show typical SMM behavior and at all temperatures the plots of $\ln(\tau)$ versus T^{-1} are linear confirming a single relaxation process without QTM in complexes **2**–**5**. Anisotropy barriers of 62.1 (43.2 cm^{-1}), 79.1 (55.0 cm^{-1}), 61.6 (42.8 cm^{-1}), and 63.4 (44.1 cm^{-1}) K, with τ_0 = 2.3 × 10^{-7}, 3.4 × 10^{-8}, 1.1 × 10^{-7}, and 8.3 × 10^{-7} s were found for **2**–**5**, respectively (Table 1). Whilst it might be conjectured that the size of the effective barrier can be related to the electronic properties of the different R groups, there is no clear trend here. This may be the result of the recently discussed ambiguities with fitting relaxation data to an Arrhenius law pointed out by Hill et al. [34,35].

Cole-Cole plots indicate single relaxation processes within all the compounds with small α values, in line with a single Orbach relaxation process. Open M(H) hysteresis loops at temperatures up to ~3.5 K were also observed for all the compounds with sweep rates of 0.002 T/s (0.003 T/s for **1**) (Fig. 6), again in line with what was observed for complex **1**. The results indicate the main ligands have a small influence on the strong intra-cluster magnetic interactions between Cr^{III} and Dy^{III} ions as shown by the χT vs T plots and the effective energy barriers. Furthermore, every compound shows magnetic hysteresis loops open with large coercive fields, which is a rare observation for $3d$-$4f$ based SMMs using a conven-

Table 8
Magnetic data and structural features of Zn^{II}, Co^{III}, Mg^{II} and Al^{III}-4f butterfly SMMs.

	Space group	Applied dc field/Oe	Relaxation processes		Raman/C/ s $^{-1}$ K ^{n} and n	Direct	QTM/s	Ref
			Orbach					
			U_{eff}/K (cm $^{-1}$)	τ_0/s				
$[Zn^{II}_2Dy_2(L1)_4(NO_3)_2(MeOH)_2]$ **59**	P-1	0	140.4 (97.6)	1.4×10^{-7}	C = 2.1×10^{-2} n = 4.1	–	1.50×10^{-2}	[60]
$[Zn^{II}_2Dy_2(L2)_4(NO_3)_2(MeOH)_2]$ **60**	P-1	0	115 (79.9)	2.35×10^{-6}	C = 0.116 n = 3.26	–	9.2×10^{-3}	[45]
$[Zn_2Dy_2(L3)_4(NO_3)_2(MeOH)_2]$ **61**	$P2_1/n$	0	112.2 (78)	8.2×10^{-5}	C = 1.47×10^{-4} n = 5.4	–	–	[69]
$[Zn^{II}_2Dy_2(L3)_4(OAc)_2(EtOH)_2]$ **62**	P-1	0	74.8 (52)	2.78×10^{-6}	–	–	2.5×10^{-4}	[69]
$[Zn^{II}_2Dy_2(L3)_4(OAc)_2(EtOH)_2]$ **63**	P-1	0	116.0 (80.6)	6.6×10^{-9}	C = 16.75 n = 2.02	–	4.1×10^{-4}	[70]
$[Zn^{II}_2Dy_2(L3)_4(OAc)_2(MeOH)_2]$ **64**	P-1	0	149.9 (104.2)	1.26×10^{-7}	C = 3.26×10^{-4} n = 5.67	–	2.02	[70]
$[Co^{III}_2Tb_2(OMe)_2(teaH)_2(O_2CPh)_4(MeOH)_4](NO_3)_2$ plus $[Co^{III}_2Tb_2(OMe)_2(teaH)_2(O_2CPh)_4(MeOH)_2(NO_3)_2]$ **65**	I41/a	10,000	14.3 (9.95)	2.84×10^{-6}	–	–	–	[71]
		17,500	19.0 (13.2)	6.02×10^{-6}	–	–	–	
$[Co^{III}_2Dy_2(OMe)_2(teaH)_2(O_2CPh)_4(MeOH)_4](NO_3)_2$ plus $[Co^{III}_2Dy_2(OMe)_2(teaH)_2(O_2CPh)_4(MeOH)_2(NO_3)_2]$ **66**	I41/a	0	88.2 (61.3)	5.64×10^{-8}	+	+	<1.5	[71]
$[Co^{III}_2Dy_2(OMe)_2(teaH)_2(acac)_4(NO_3)_2]$ **67**	P-1	0	27 (18.8)	8.1×10^{-6}	+	+	5.8×10^{-4}	[72]
$[Co^{III}_2Dy_2(OH)_2(teaH)_2(acac)_4(NO_3)_2]$ **68**	$P2_1/c$	0	28 (19.5)	7.4×10^{-6}	+	+	5.8×10^{-4}	[72]
$[Co^{III}_2Dy_2(OMe)_2(mdea)_2(acac)_4(NO_3)_2]$ **69**	P-1	0	38 (26.4)	2.6×10^{-6}	+	+	2.5×10^{-3}	[72]
$[Co^{III}_2Tb_2(OH)_2(^nBudea)_2(acac)_2(NO_3)_4]$ **70**	$P2_1/n$	5000	–	–	–	–	–	[73]
$[Co^{III}_2Dy_2(OH)_2(^nBudea)_2(acac)_2(NO_3)_4]$**71**	$P2_1/n$	0	169 (117.5)	1.47×10^{-7}	+	+	2.5×10^{-3}	[73]
$[Co^{III}_2Dy_2(OMe)_2(teaH)_2(Piv)_6]$ **72**	P-1	0	51 (35.4)	6.1×10^{-7}	–	–	7.3	[74,75]
			127 (88.3)	1.2×10^{-9}	C = 1.7×10^{-3} n = 5	–	–	
		1500	89[a] (61.9) 104[b] (72.3) –	5.4×10^{-8a} 5.4×10^{-8b}	C = 5.5×10^{-3a} n = 5[a] C = 1.7×10^{-4b} n = 7[b] C = 2.2×10^{-4c} n = 7[c]	–	–	
			59 (41)	1.7×10^{-7}	–	–	0.58	
			–	–	–	–	2.0×10^{-4}	
$[Co^{III}_2Tb_2(OMe)_2(teaH)_2(Piv)_6]$ **73**	P-1	1000	–	–	–	–	–	[76]
$[Co^{III}_2Ho_2(OMe)_2(teaH)_2(Piv)_6]$ **74**	P-1	3000	43.2 (30)	6.2×10^{-9}	–	–	–	[76]
$[Co^{III}_2Er_2(OMe)_2(teaH)_2(Piv)_6]$ **75**	P-1	1500	–	–	C = 3.5×10^{-2} n = 7	–	5.1×10^{-3}	[76]
$[Co^{III}_2Yb_2(OMe)_2(teaH)_2(Piv)_6]$ **76**	P-1	1500	33.1 (23)	2.1×10^{-6}	–	–	1.3×10^{-2}	[76]
$[Co^{III}_2Dy_2(OMe)_2(dea)_2(O_2CPh)_4(MeOH)_4](NO_3)_2$ **77**	$P2_1/n$	0	103.6 (72)	6.05×10^{-8}	+	+	0.12	[77]
$[Co^{III}_2Dy_2(OMe)_2(mdea)_2(O_2CPh)_4(NO_3)_2]$ **78**	$P2_1/n$	0	79.1 (55)	1.03×10^{-7}	+	+	0.2	[77]
$[Co^{III}_2Dy_2(OMe)_2(^nBudea)_2(O_2CPh)_4(MeOH)_4](NO_3)_2$ plus $[Co^{III}_2Dy_2(OMe)_2(^nBudea)_2(O_2CPh)_4(MeOH)_2(NO_3)_2]$ **79**	$P2_1/n$	0	115.1 (80)	3.38×10^{-8}	+	+	0.48	[77]
$[Co^{III}_2Dy_2(OH)_2(teaH)_2(acac)_6]$ **80**	P-1	0	71 (49) and 45 (31)	2.7×10^{-7} and 3.2×10^{-7}	–	–	7.6×10^{-2}	[78]
$[Co^{III}_2Dy_2(OH)_2(^nBudea)_2(acac)_6]$ **81**	Pccn	0	27 (19)	1.0×10^{-6}	–	–	1.4×10^{-3}	[78]
		500	38 (26)	2.7×10^{-7}				
$[Co^{III}_2Dy_2(OH)_2(edea)_2(acac)_6]$ **82**	P-1	1000	16 (11)	1.3×10^{-6}	–	–	–	[78]
$[Co^{III}_2Dy_2(OMe)_2(^nBudea)_2(o-Cl-PhCO_2)_4(NO_3)_2]$ **83**	P-1	0	115.7 (80.4)	1.8×10^{-8}	+	+	0.9	[43]
$[Co^{III}_2Dy_2(OMe)_2(^nBudea)_2(p-^tBu-PhCO_2)_4(NO_3)(MeOH)_3](NO_3)$ **84**	$P2_1/n$	0	110.6 (76.9) and 137.6 (95.6)	3.8×10^{-9} and 5.6×10^{-8}	+	+	0.5	[43]

Table 8 (*continued*)

	Space group	Applied dc field/Oe	Relaxation processes		Raman/C/ s $^{-1}$K $^{-n}$ and n	Direct	QTM/s	Ref
			Orbach					
			U_{eff}/K (cm $^{-1}$)	τ_0/s				
[Co$_2^{III}$Dy$_2$(OMe)(OH) (^{n}Budea)$_2$(o-CF$_3$-PhCO$_2$)$_4$ (NO$_3$)$_2$] **85**	P-1	0	126.8 (88.1)	1.4×10^{-8}	+	+	~ 1.5	[43]
[Co$_2^{III}$Dy$_2$(OH)$_2$(mdea)$_2$(o-Me-PhCO$_2$)$_4$(NO$_3$)$_2$] **86**	P-1	0	116.9 (81.2)	9.8×10^{-9}	C = 1.3×10^{-4} n = 7	–	0.34	[79]
[Co$_2^{III}$Tb$_2$(OH)$_2$(mdea)$_2$(o-Me-PhCO$_2$)$_4$(NO$_3$)$_2$] **87**	P-1	5000	49.2 (34.2)	6.6×10^{-11}	–	–	–	[79]
[Co$_2^{III}$Ho$_2$(OH)$_2$(mdea)$_2$(o-Me-PhCO$_2$)$_4$(NO$_3$)$_2$] **88**	P-1	2000	–	–	–	–	–	[79]
[^{i}Pr$_2$NH$_2$]$_2$[Mg$_2^{II}$Dy$_2$(OH)$_2$(Piv)$_{10}$] **89**	P2$_1$/c	0	44 (30.6)	7.8×10^{-7}	+	+	+	[50]
[^{i}Pr$_2$NH$_2$]$_2$[Mg$_2^{II}$Er$_2$(OH)$_2$(Piv)$_{10}$] **90**	P2$_1$/c	1000	23 (16.0)	6.6×10^{-7}	+	+	+	[50]
[Al$_2^{III}$Dy$_2$(OH)$_2$(pdea)$_2$(p-Me-PhCO$_2$)$_6$] **91**	P-1	0	38.7 (26.9)	1.06×10^{-6}	+	+	+	[25]
		1000	41.5 (28.8)	9.95×10^{-7}	+	+	+	
[Al$_2^{III}$Er$_2$(OH)$_2$(pdea)$_2$(p-Me-PhCO$_2$)$_6$] **92**	P-1	1000	4.54 (3.2) and 28.73 (20.0)	4.85×10^{-4} and 1.54×10^{-6}	+	+	+	[23]

Lattice solvent molecules are not listed. + means multiple relaxation processes were observed but not analyzed. – means multiple relaxation processes were not observed.
a,b and c mean three different setups for fitting.

tional magnetometer rather than a micro-SQUID set-up. The lack of a step in the hysteresis at zero field for compound **4** (Fig. 6) indicates ZF-QTM is suppressed significantly more than in compounds **1**–**3** and **5**.

Subsequently, a new series of {Cr$_2^{III}$Dy$_2$} heterometallic butterfly complexes of formulae [Cr$_2^{III}$Dy$_2$(OMe)$_2$(R-dea)$_2$(acac)$_4$(NO$_3$)$_2$] (acacH = acetylacetone, R = Me **6**, Et **7** or ^{n}Bu **8**) was investigated by the same group [36]. The compounds are isostructural, crystallize in the triclinic space group *P-1*, only differing from each other by variation of the amine based polyalcohol ligands. Each compound was found to be a heterometallic butterfly of **Type II** (Fig. 7), and the metal cores are also bridged by two μ$_3$-OMe ligands. Each complex is further stabilized around the periphery by two doubly deprotonated amine-polyalcohol ligands displaying μ$_3$-η^2: η^1:η^2 coordination mode (Scheme S2). Each of the four acac$^-$ ligands chelate to each of the four metal ions (Fig. 7). The two remaining coordination sites of each 8-coordinate Dy^{III} ion are occupied by a chelating nitrate giving a distorted square anti-prismatic geometry. The Cr^{III} ions have a distorted octahedral geometry with deviation values slightly larger than those found in complexes **1**–**5** (0.35–0.45) and in the range 0.55–0.67. For the Dy^{III} ions in compounds **6** and **7**, the deviation values are similar to those of compound **1**, and in compound **8** the deviation values are similar to compounds **3** and **4** (Table S3 for the estimated deviations for the idealized geometries).

The dc susceptibility measurements suggest that there are significant changes in the magnetic interactions between the Cr^{III} and Dy^{III} ions (Fig. 8) and *ab initio* calculations yielded Cr^{III}-Dy^{III} exchange parameters (11.24 and 8.33 cm^{-1} for **6**, 11.88 and 7.69 cm^{-1} for **7**, 10.48 and 7.14 cm^{-1} for **8**) which are all much smaller than for compound **1** (Table 2). All complexes show classic SMM behavior (Fig. 9). A fit to the data with an Arrhenius law yields energy barriers of 34.6 K (24 cm^{-1}), 41.6 K (29 cm^{-1}) and 37.5 K (26 cm^{-1}), with τ$_0$ = 1.2 × 10^{-7} s, 9.2 × 10^{-8} s and 3.1 × 10^{-7} s for **6**–**8**, respectively (Fig. 10). Again, the plots of ln (τ) versus T^{-1} are linear at all temperatures indicating that a single process is operative for all three compounds and Cole-Cole plots indicate a single relaxation process with small α parameters for all three complexes, which is similar to what was found for **1**–**5**. M(H) hysteresis loops at temperatures up to 1.8 K for **6**, and 2.2 K for **7** and **8** (Fig. 10) were observed using a sweep rate of

0.004 T s^{-1}. The coercive field for **7** and **8** is found to be ~1000 Oe at 1.8 K, which decreases with increasing temperature, typical of a SMM. The relaxation times are found to be faster for compound **6**, which displays a very narrow coercive field at 1.8 K, in line with the dynamic behavior of compound **1**. The results associated with *ab initio* calculations indicate that the anisotropy barrier is related to the J_{Cr-Dy} magnetic exchange interaction. When J_{Cr-Dy} increases, U_{eff} increases, highlighting a clear route towards the enhancement of slow magnetic relaxation of {Cr$_2^{III}$Dy$_2$} coupled systems.

More recently, a series of {Cr$_2^{III}$Ln$_2$} systems of formula {Cr$_2^{III}$Ln$_2$ (OMe)$_2$(O$_2$CPh)$_4$(R-dea)$_2$(NO$_3$)$_2$}, (R = CH$_2$CH$_2$OH, Ln = Nd **9**, R = Me, Ln = Tb **10**, Ho **11** and Er **12**) was reported [37]. The results show the effect that the *4f* ions can have on the magnetic properties within these {Cr$_2^{III}$Ln$_2$} butterfly systems (Fig. 11).

The dc susceptibility measurements indicate the four compounds show significantly different static magnetic behavior compared to complex **1** {Cr$_2^{III}$Dy$_2$}. There is slow magnetic relaxation but without maxima observed for compounds **9** {Cr$_2^{III}$Nd$_2$} and **12** {Cr$_2^{III}$Er$_2$} even under small applied dc field. It should be noted that in the literature only one other compound containing Nd^{III} shows slow magnetic relaxation [38]. Contrary to the cases of **9** {Cr$_2^{III}$Nd$_2$} and **12** {Cr$_2^{III}$Er$_2$}, typical SMM behavior was observed for **10** {Cr$_2^{III}$Tb$_2$}and **11** {Cr$_2^{III}$Ho$_2$} (Fig. 12) with U_{eff} = (64 ± 1) K (~44 cm^{-1}), τ$_0$ = 1.7 × 10^{-9} s and U_{eff} = (52 ± 0.7) K (~36 cm^{-1}) , τ$_0$ = 1.1 × 10^{-9} s (Fig. 13) under zero dc field, respectively. A fit to Cole-Cole plots for **10** {Cr$_2^{III}$Tb$_2$} and **11** {Cr$_2$Ho$_2$} (Fig. 13 inset) gave small α parameters, indicating a narrow distribution of relaxation times. M/H hysteresis loops open for complex **10** {Cr$_2^{III}$Tb$_2$} up to 2.5 K (Fig. 14a). Moreover, the plot shows a butterfly shape [39,40] with a large loss of magnetization at zero-field as is commonly observed for Tb^{III} based complexes due to QTM. For compound **11** {Cr$_2$Ho$_2$}, a very narrow open hysteresis loop is observed (Fig. 14b) at 1.8 K, which is rare for Ho^{III} based complexes. No magnetic hysteresis was observed for compounds **9** {Cr$_2^{III}$Nd$_2$} and **12** {Cr$_2^{III}$Er$_2$}, which is consistent with the ac experiments.

As the relaxation barriers in the {Cr$_2^{III}$Ln$_2$} species are mainly dependent on the exchange interaction between Cr^{III} and Dy^{III} ions, it is interesting to see if modifying the bridging benzoate ligands can affect the exchange interaction between Cr^{III} and Dy^{III} ions and thus further influence the magnetic properties in the {Cr$_2^{III}$Ln$_2$} butterfly systems. With this in mind, the Murray group utilized two types of substituted benzoate ligands (electron withdrawing

Table 9

The J values between paramagnetic centers obtained from *ab initio* calculations for {$Zn_2^{II}Ln_2$}, {$Co_2^{III}Ln_2$} {$Mg_2^{II}Ln_2$} and {$Al_2^{III}Ln_2$} systems.

	[$Zn_2^{II}Dy_2(L2)_4(NO_3)_2$ (MeOH)$_2$] **60** Fitted^m	[$Zn_2^{II}Dy_2(L3)_4(NO_3)_2$ (MeOH)$_2$] **61** Fitted^m	[$Zn_2^{II}Dy_2(L3)_4(OAc)_2$ (EtOH)$_2$] **62** Fitted^m	[$Zn_2^{II}Dy_2(L3)_4(OAc)_2$ (EtOH)$_2$] **63** Fitted^m	[$Zn_2^{II}Dy_2(L3)_4(OAc)_2$ (MeOH)$_2$] **64** Fitted^m
J^{tot}_{Dy-Dy}	2.8	0.41	0.37	0.35	0.48
J^{ex}_{Dy-Dy}	–	0.25	0.25	0.25	0.25
J^{dip}_{Dy-Dy}	–	0.66	0.62	0.60	0.43
zJ	0	0	0	0.01	0

[$Co_2^{III}Dy_2(OMe)_2(teaH)_2(O_2CPh)_4(MeOH)_4](NO_3)_2 \cdot MeOH \cdot H_2O$ (1) plus [$Co_2^{III}Dy_2(OMe)_2(teaH)_2(O_2CPh)_4(MeOH)_2(NO_3)_2] \cdot MeOH \cdot H_2O$ (2) **66*****

	Molecule 1^n				Molecule 2^n			
	A_α	A_β	B_α	B_β	A_α	A_β	B_α	B_β
J^{tot}_{Dy-Dy}	2.92128	2.93519	2.92106	2.93689	2.93338	2.95717	2.93735	2.95893
J^{ex}_{Dy-Dy}	0.61950	0.53625	0.62100	0.53795	0.51850	0.53900	0.52052	0.53925
J^{dip}_{Dy-Dy}	2.30178	2.39894	2.30006	2.39714	2.41488	2.41817	2.41685	2.41968

	[$Co_2^{III}Ln_2(OMe)_2(teaH)_2(Piv)_6$] **72** Fitted^l	[$Co_2^{III}Dy_2(OMe)_2(dea)_2(O_2CPh)_4(MeOH)_4](NO_3)_2$ **77*****		[$Co_2^{III}Dy_2(OMe)_2(mdea)_2(O_2CPh)_4(NO_3)_2$] **78*****	
		B_α^n	B_β^n	B_α^n	B_β^n
J^{tot}_{Dy-Dy}		2.77075	2.77425	2.62625	2.62050
J^{ex}_{Dy-Dy}	0.046	0.03950	0.04275	0.18425	0.19025
J^{dip}_{Dy-Dy}		2.61184	2.61073	2.69086	2.69157

[$Co_2^{III}Dy_2(OMe)_2(^nBudea)_2(O_2CPh)_4(MeOH)_4](NO_3)_2$ (1) plus [$Co_2^{III}Dy_2(OMe)_2(^nBudea)_2(O_2CPh)_4(MeOH)_2(NO_3)_2$] (2) **79*****

	Molecule 1^n		Molecule 2^n	
	B_α	B_β	B_α	B_β
J^{tot}_{Dy-Dy}	2.54075	2.52975	2.567565	2.55575
J^{ex}_{Dy-Dy}	0.04225	0.05300	0.07150	0.05300
J^{dip}_{Dy-Dy}	2.46831	2.46478	2.50851	2.50971

	[$Co_2^{III}Dy_2(OMe)_2(p\text{-}^tBu\text{-}PhCO_2)_4(^nBudea)_2(NO_3)(MeOH)_3](NO_3)$ **84*****		[$Co_2^{III}Dy_2(OH)_2(o\text{-}Me\text{-}PhCO_2)_4(mdea)_2(NO_3)_2$] **86**		[$Co_2^{III}Tb_2(OH)_2(o\text{-}Me\text{-}PhCO_2)_4(mdea)_2(NO_3)_2$] **87**		[$Co_2^{III}Ho_2(OH)_2(o\text{-}MePhCO_2)_4(mdea)_2(NO_3)_2$] **88**	
	A Fitted^n	B Fitted^n	DFT	Fitted^l	DFT	Fitted^l	DFT	Fitted^l
J^{tot}_{Ln-Ln}	2.71116	2.73228	–	–	–	–	–	–
J^{ex}_{Ln-Ln}	0.17296	0.22667	0.029	0.05	0.034	0.042	0.023	0.012
J^{dip}_{Ln-Ln}	2.53820	2.50561	–	–	–	–	–	–

	[$Al_2^{III}Dy_2(OH)_2(pdea)_2(p\text{-}Me\text{-}PhCO_2)_6$] **91** Fitted^m
J^{tot}_{Dy-Dy}	0.049
J^{ex}_{Dy-Dy}	0.025
J^{dip}_{Dy-Dy}	0.024

Two structural models for the mononuclear Dy^{III} fragments have been employed: fragment A (small) and B (large). The employed structures were both computed within two basis set approximations: α-small (DZP-quality) and β-large (TZP-quality). ***means $J^{tot} = J^{ising} + J^{dip}$, the J^{dip} is from Ising term.

^{l} $H = J^{ex}_{Dy\,Dy}\hat{s}_{Dy1}\hat{s}_{Dy2}$ (eqn 16).
$\hat{s}_{Dy} = 1/2$.
^{m} $H = J^{tot}_{Dy\,Dy}\hat{s}_{Dy1}\hat{s}_{Dy2}$ (eqn 17).
$\hat{s}_{Dy} = 1/2$, $J^{tot} = J^{ex} + J^{dip}$.
^{n} $H = J^{tot}_{Dy\,Dy}\hat{s}_{Dy1}\hat{s}_{Dy2}$ (eqn 18).
$\hat{s}_{Dy} = 1/2$, $J^{tot} = J^{ising} + J^{dip}$.
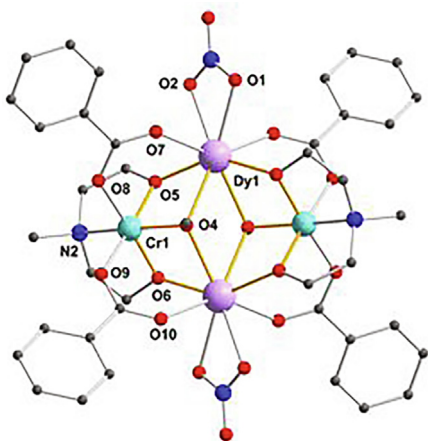
Fig. 2. Molecular structure of **1** [$Cr_2^{III}Dy_2(OMe)_2(O_2CPh)_4(mdea)_2(NO_3)_2$].

halogen and electron donating *tert*-butyl) isolating four new complexes with formulae of [$Cr_2^{III}Ln_2(OMe)_{2-x}(OH)_x(o$-Cl-*p*,*m*-F-PhCO_2)_4(mdea)_2(NO_3)_2$]·nMeOH (Ln = Tb **13**, Dy **14** and Ho **15**) and [$Cr_2^{III}Dy_2(OMe)(OH)(p$-^{t}Bu-PhCO_2)_4(^{t}Budea)_2(NO_3)_2$]·MeOH·2Et_2O **16** (^{t}BudeaH_2 = *N*-*tert*-butyldiethanolamine) (Fig. 15) [41]. Compounds **13–16** crystallize in the triclinic space group *P-1*. They display the same core topology and bridging structure as the parent benzoate compounds **1**, **10** and **11**.

Direct current (dc) magnetic susceptibility measurements show that the {$Cr_2^{III}Ln_2$} complexes (Ln = Tb **13**, Dy (**14** and **16**) and Ho **15**) have similar behavior to the benzoate analogues (PhCO_2^- for **1**, **10** and **11**, *o*-Cl-*p*,*m*-F-PhCO_2^- for **13–15** and *p*-^{t}Bu-PhCO_2^- for **16**) with subtle differences in the χT vs T plots. They are all SMMs under zero dc field with U_{eff} = 63.4 K (44 cm^{-1}) and τ_0 = 7.7 × 10^{-9} s for **13**, U_{eff} = 87.8 K (61 cm^{-1}) and τ_0 = 2.1 × 10^{-7} s for **14**, U_{eff} = 51.8 K (36 cm^{-1}) and τ_0 = 6.8 × 10^{-9} s for **15** and U_{eff} = 64.8 K (45 cm^{-1}) and τ_0 = 6.8 × 10^{-8} s for **16** (Fig. 16). Magnetic hysteresis loops of all samples are temperature dependent, with open loops observed up to 3.5 K with coercive fields of 1.4 T at 4.7 K, 4.4 T at 2.6 K, 1.2 T at 3.1 K and 2.2 T at 1.8 K for **13–16**, respectively, all at an average sweep rate of 0.003 T/s (Fig. 17). The experimental data suggest that the substituent atoms present on the bridging carboxylate co-ligand for **13–16** have a substantial influence on the magnetization dynamics. The benzoate substituents probably influence the strength of the magnetic exchange interaction, which was also shown to directly influence the anisotropy barrier and thus the relaxation time [42].

Based on the [$Cr_2^{III}Dy_2(OMe)_2(acac)_4(mdea)_2(NO_3)_2$] complex, the acac$^-$ and nitrate ligands could be replaced by hfacac$^-$ ligands, to give molecules such as [$Cr_2^{III}Dy_2(OMe)_2(mdea)_2(hfacac)_6$] **17** (Fig. 18) [43]. The Cr^{III} ions adopt octahedral coordination geometry with a deviation value of 0.72 and for Dy^{III} ions square anti-prismatic coordination geometry with a deviation value of 0.74 (see Table S3 for the estimated deviations for the idealized geometries).
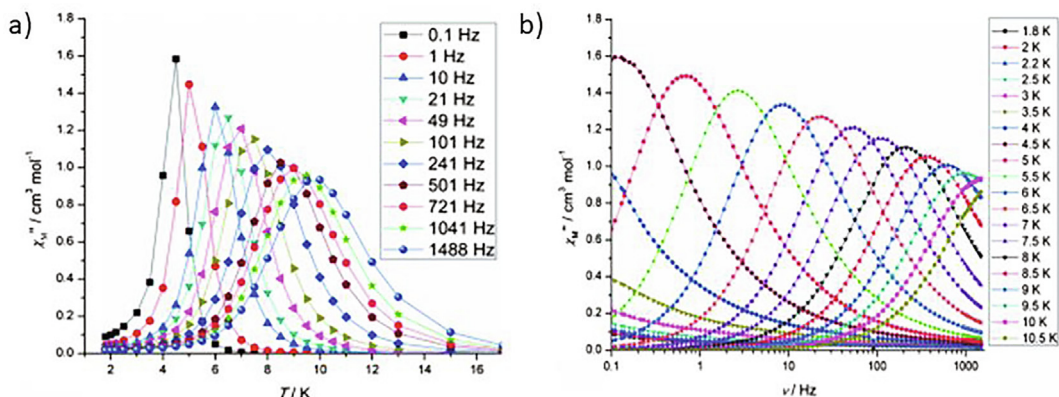
Fig. 3. Plots of χ'' vs T (a) and ν (b) for **1** [$Cr_2^{III}Dy_2(OMe)_2(O_2CPh)_4(mdea)_2(NO_3)_2$] under zero applied dc field. Reprinted with permission from [32]. Copyright (2013) Wiley-VCH Verlag GmbH& Co. KGaA.
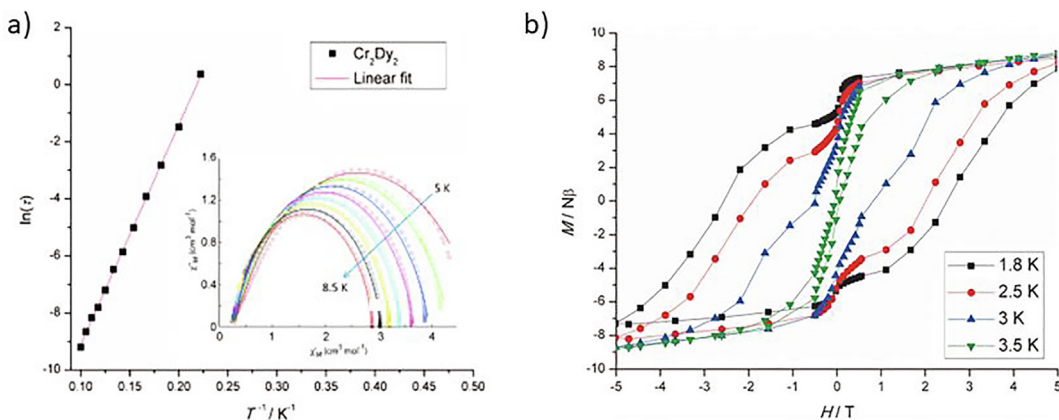
Fig. 4. Plot of ln(τ) vs T^{-1} for compound **1** [$Cr_2^{III}Dy_2(OMe)_2(O_2CPh)_4(mdea)_2(NO_3)_2$]. The solid red line represents a fit to the Arrhenius law in the thermally activated regime. Inset of (a): Cole-Cole plots of **1**. The solid lines are best fits (a). Plots of M vs H for **1** with an average sweep rate of 0.003 T/s (b). Reprinted with permission from [32]. Copyright (2013) Wiley-VCH Verlag GmbH& Co. KGaA.
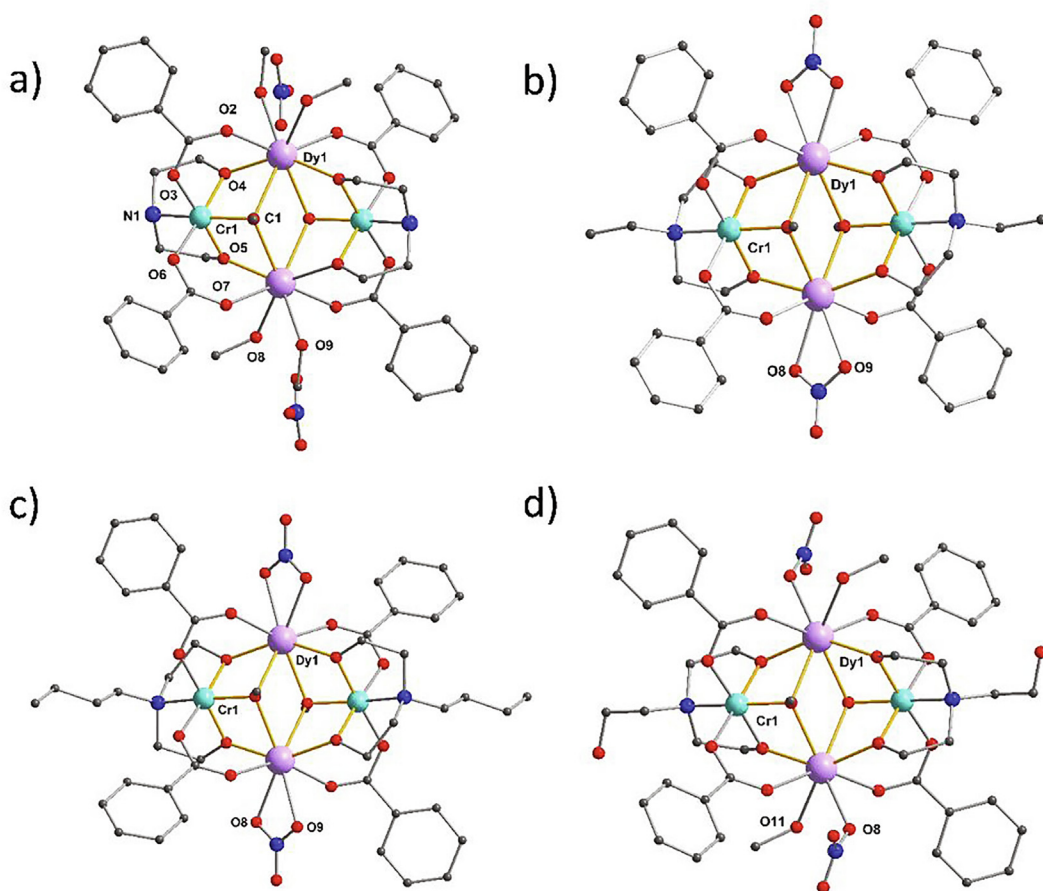
Fig. 5. The molecular structures of **2** [Cr$_2^{III}$Dy$_2$(OMe)$_2$(O$_2$CPh)$_4$(dea)$_2$(MeOH)$_4$](NO$_3$)$_2$ (a), **3** [Cr$_2^{III}$Dy$_2$(OH) (OMe)(O$_2$CPh)$_4$(edea)$_2$(NO$_3$)$_2$]·MeOH·Et$_2$O (b), **4** [Cr$_2^{III}$Dy$_2$(OMe)$_2$(O$_2$-CPh)$_4$(^{n}Budea)$_2$(NO$_3$)$_2$] (c) and **5** [Cr$_2^{III}$Dy$_2$(OMe)$_2$(O$_2$CPh)$_4$(teaH)$_2$(NO$_3$)$_2$(MeOH)$_2$] (d).

From the dc susceptibility measurements, it can be seen that **17** shows similar magnetic behavior to the analogous {Cr$_2^{III}$Dy$_2$} complexes. Ac susceptibility measurements show clear evidence of SMM behavior for **17** with χ'' versus frequency plots displaying out-of-phase susceptibility maxima at zero dc field (Fig. 19a) with U_{eff} = 41.1 K (28.6 cm^{-1}) and τ_0 = 1.6 × 10^{-7} s^{-1}. Magnetic hysteresis loops are open up to 2.2 K with a coercive field H$_{dc}$ = 0.25 T (Fig. 19b). The results indicate that the electron-withdrawing groups provide a potential route towards improving the exchange strength, and hence the energy barrier in exchange type relaxation processes involving anisotropic Ln^{III} ions.

Summary: For the **Type II** butterfly {Cr$_2^{III}$Ln$_2$} system, all the Dy^{III} analogues show typical SMM behavior with open hysteresis loops on randomly ordered samples up to surprisingly high temperatures for 3d-containing systems. This seems to result from the relatively strong antiferromagnetic interactions between the Cr^{III} and Dy^{III} ions as identified from ab initio calculations (Table 2). This helps to slow down the usually very fast relaxation of the Dy^{III} single ions, as judged by the global relaxation parameters for the cooperative butterfly system and the relaxation behavior can be analyzed exclusively with an Orbach process. Although not so impressively, some of the Tb^{III} and Ho^{III} analogues show nice SMM behavior with open hysteresis loops even if the Tb^{III} compounds suffer from zero-field quantum tunneling effects as judged by the ac signals and the hysteresis measurements. The relaxation rates for the compounds with these ions are notably faster than the Dy analogues. In one family, even the Nd^{III} and Er^{III} analogues show slow relaxation but without maxima in the out-of-phase ac signals. Such behavior for these lanthanides is rarely observed in 3d-4f SMM complexes.

From further studies, it also appears that the co-ligands have more influence on the magnetic properties than the main ligands. This is clear from the results with electron withdrawing groups on the co-ligands which reduce the ZF-QTM.

Given the good SMM performance of these systems and the potential to tune other parameters, it is a pity that examples with other paramagnetic 3d M^{III} ions such as Mn^{III} and Fe^{III} are not so far available. There are few **Type II** {Cr$_2^{III}$Ln$_2$} compounds making magneto-structural correlations in terms of the influence of the 3d ion and its influence via superexchange difficult. However, it is clear that this **Type II** {Cr$_2^{III}$Ln$_2$} butterfly is an interesting benchmark compound towards the understanding of the important parameters in 3d-4f SMMs. The fact that only four compounds were subjected to ab initio calculations means that at present no meaningful magneto-structural correlation can be proposed. It would be most instructive to have such calculations on the other compounds described here.

3.1.2. {Mn$_2^{II}$Ln$_2$} and {Mn$_2^{III}$Ln$_2$} systems

3.1.2.1. {Mn$_2^{II}$Ln$_2$} systems. Chen's group reported the first [Mn$_2^{II}$Ln$_2$] butterfly family showing slow relaxation of the magnetization with formulae [Mn$_2^{II}$Ln$_2$(hmp)$_6$(NO$_3$)$_4$(MeOH)$_2$] and [Mn$_2^{II}$Ln$_2$(hmp)$_6$ (NO$_3$)$_4$(H$_2$O)$_2$] (Ln = Tb **18** or Dy **19**) formed through solvothermal reaction of Mn(NO$_3$)$_2$ with hmpH ((2-hydroxymethyl)pyridine), Et$_3$N and Ln(NO$_3$)$_3$·6H$_2$O in MeOH [44]. Compounds **18** and **19** are isostructural, crystallizing in the triclinic space group P-1. The asymmetric unit contains two similar butterfly units with [Mn$_2^{II}$Ln$_2$] cores of **Type I** but with differences in the coordinated solvent ligands (Fig. 20). For both, the [Mn$_2^{II}$Ln$_2$] core is chelated and bridged by
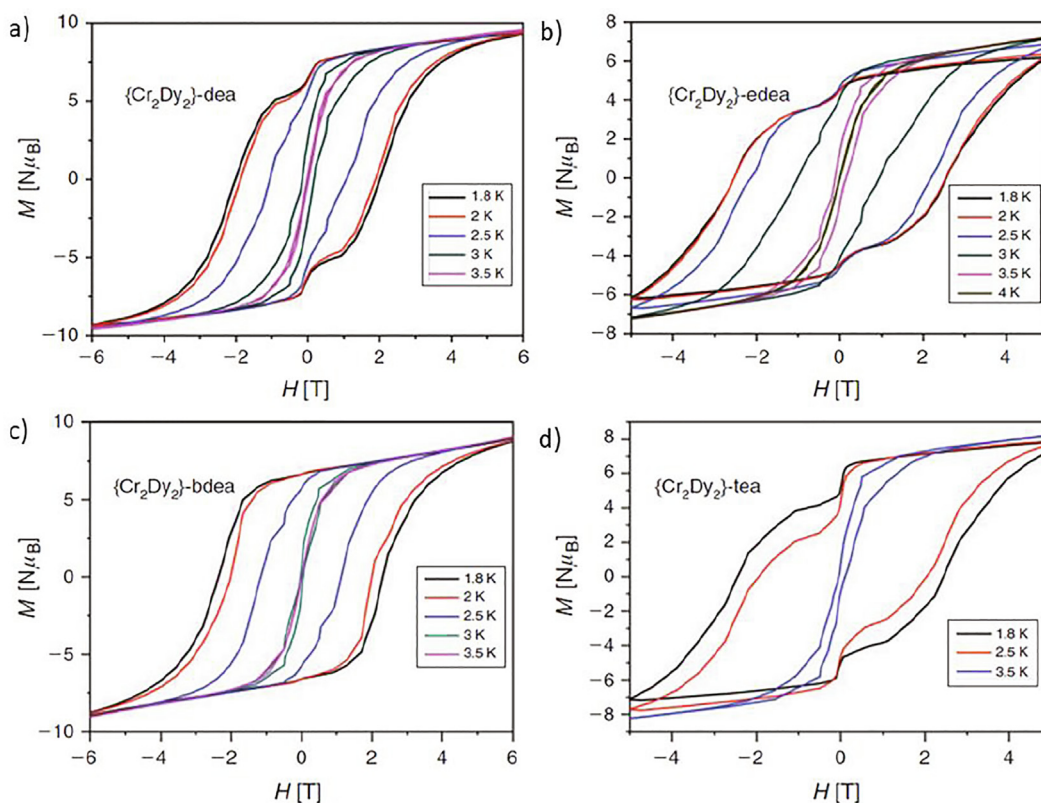
Fig. 6. Plots of M vs H for **2** $[Cr_2^{III}Dy_2(OMe)_2(O_2CPh)_4(dea)_2(MeOH)_4](NO_3)_2$ (a), **3** $[Cr_2^{III}Dy_2(OMe)_2(O_2CPh)_4(edea)_2(NO_3)_2]\cdot MeOH\cdot Et_2O$ (b), **4** $[Cr_2^{III}Dy_2(OMe)_2(O_2CPh)_4(^nBudea)_2 (NO_3)_2]$, (c) and **5** $[Cr_2^{III}Dy_2(OMe)_2(O_2CPh)_4(teaH)_2(NO_3)_2(MeOH)_2]$ (d) with an average (sweep rate of 0.002 T/s. Reprinted with permission from [33]. Copyright (2014) CSIRO Publishing.
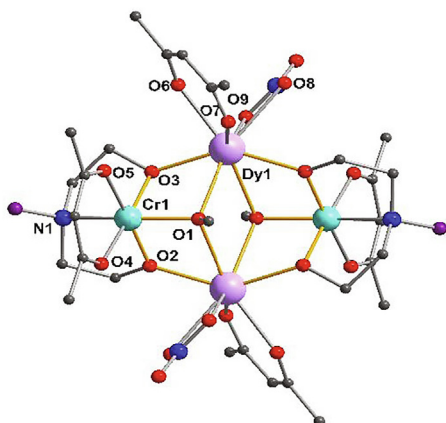
Fig. 7. Molecular structures of $[Cr_2^{III}Dy_2(OMe)_2(R-dea)_2(acac)_4(NO_3)_2]$ (acacH = acetylacetone, purple = R = Me **6**, Et **7** or n-Bu **8**).

Fig. 8. Plots of χT vs T for **6–8** under 1000 Oe dc field. Reprinted with permission from [36]. Copyright (2014) The Royal Society of Chemistry.

two $\eta^3:\eta^1:\mu_3$ hmp$^-$ groups and four $\eta^2:\eta^1:\mu_2$ hmp$^-$ groups. The peripheral ligation is completed by two chelating NO_3^- ligands and two MeOH (for **18** Tb) or two H_2O (for **19** Dy) terminal ligands. All four Mn^{II} atoms are six coordinate displaying octahedral coordination geometry and the Ln ions are nine-coordinate and can be described as having a capped square antiprism geometry (Table S4 for the estimated deviations for the idealized geometries).

Ac susceptibility measurements reveal that compounds **18** and **19** show slow magnetic relaxation but without maxima even under small applied dc fields (Fig. 21a and 21b). Therefore, U_{eff} and τ_0 could not be determined in the usual way. However, the values of U_{eff} and τ_0 can be extracted using the relation $\ln(\chi''/\chi') = \ln(\omega$

$\tau_0) + U_{eff}/K_BT$, giving U_{eff} = 3.84 K (2.67 cm^{-1}) and τ_0 = 6.43 × 10^{-7} s for **18** (Fig. 23c), 3.86 K (2.68 cm^{-1}) and τ_0 = 1.24 × 10^{-6} s for **19** (Fig. 21d).

Subsequently Song's group reported a $[Mn_2^{II}Dy_2(L2)_4(NO_3)_2 (DMF)_2]$ **20** compound formed by recrystallizing the red powder they obtained from reaction of $Dy(NO_3)_3\cdot 6H_2O$, $Mn(NO_3)_2\cdot 6H_2O$, H_2L (((E)-2-(2-hydroxy-3-ethoxybenzylideneamino)phenol) and Et_3N in DMF and MeOH (Fig. 22) [45]. The compound crystallizes in the triclinic space group *P-1*. Two symmetry related Mn^{II} and two Dy^{III} ions are linked via two μ_3-OR phenol bridges from two separate (L2)$^{2-}$
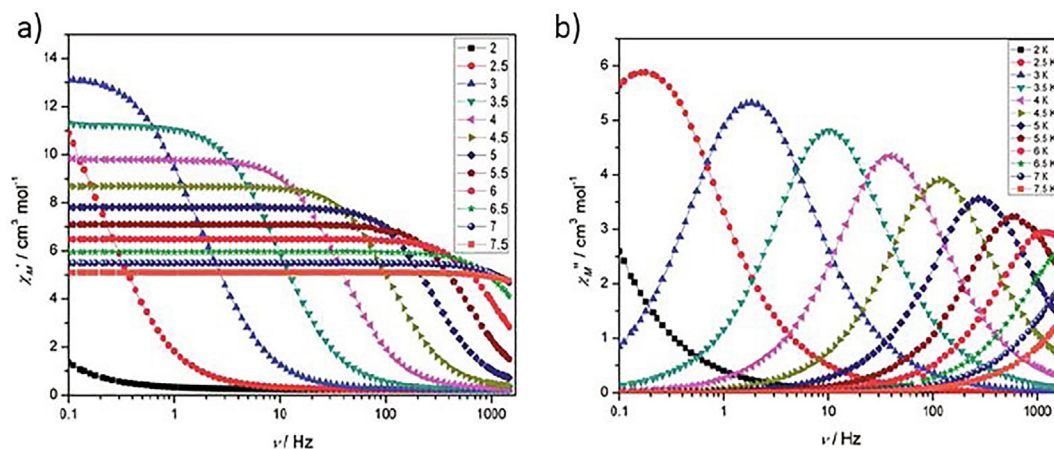
Fig. 9. Plots of χ' (a) and χ'' (b) vs ν for **8** [$Cr_2^{III}Dy_2(OMe)_2(^nBudea)_2(acac)_4(NO_3)_2$] under zero dc field. Reprinted with permission from [36]. Copyright (2014) The Royal Society of Chemistry.
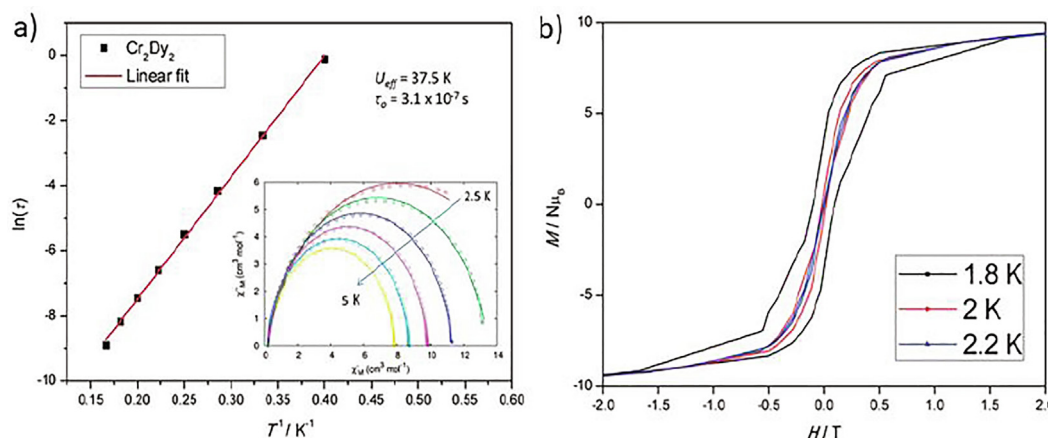
Fig. 10. Plot of $\ln(\tau)$ versus T^{-1} for compound **8** [$Cr_2^{III}Dy_2(OMe)_2(^nBudea)_2(acac)_4(NO_3)_2$]. The solid red line represents a fit to the Arrhenius law in the thermally activated regime. (inset) Cole-Cole plots of **8** at temperatures range 2.5–5 K. The solid lines are best fit (upper). Plots of M vs H for **8** with sweep rate of 0.004 T/s (lower). Reprinted with permission from [36]. Copyright (2014) The Royal Society of Chemistry.
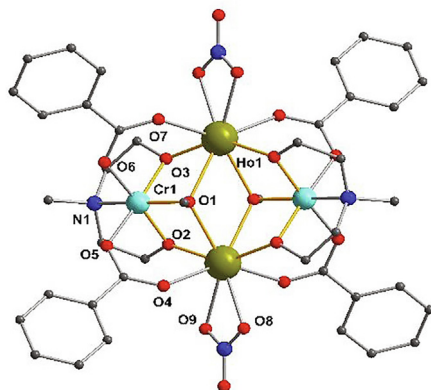
Fig. 11. Molecular structure of **11**, {$Cr_2^{III}Ho_2(OMe)_2(O_2CPh)_4(mdea)_2(NO_3)_2$}.

ligands to construct the {$Mn_2^{II}Dy_2O_2$} butterfly core of **Type I**. On the periphery, two doubly deprotonated ligands displaying a μ_3-η^1:η^2:η^1:η^2 coordination mode and two doubly deprotonated ligands displaying the μ_3- η^0:η^1:η^1:η^3 bridging and chelating mode connect the four metal ions (Scheme S2). Two chelating NO_3^- ligands are coordinated to two Dy^{III} ions and two oxygens from DMF coordinate to two Mn^{II} ions to give the eight coordinate Dy^{III} ions displaying an

ambiguous coordination geometry of either TDD-8, with a deviation value of 2.73, or BTPR-8, with a deviation value of 2.68, coordination geometry. The six coordinate Mn^{II} ions display distorted octahedral geometry with a deviation value of 3.08 (Table S4 for the estimated deviations for the idealized geometries).

Ac susceptibility measurements show magnetic relaxation but without maxima even under a small applied dc field. A fit to the ac data using the $\ln(\chi''/\chi') = \ln(\omega\tau_0) + U_{eff}/K_BT$ equation, gives $U_{eff} = 11$ K (7.6 cm^{-1}) and $\tau_0 = 1.0 \times 10^{-8}$ s, which are similar values to those found for compounds **18** and **19**. The *ab initio* calculations indicate the interactions are $J_{Dy-Dy}^{tot} = 5.5$ cm^{-1}, $J_{Mn-Dy}^{tot} = 4.8$ cm^{-1} and $J_{Mn-Mn}^{tot} = 0.2$ cm^{-1} (Table 4). It is surprising that the calculated wingtip J_{Dy-Dy}^{tot} interaction is over 25 times larger than the body J_{Mn-Mn}^{tot} interaction. This does not make physical sense.

Summary: The {$Mn_2^{II}Ln_2$} butterfly systems cannot be described as typical SMMs. These compounds show slow relaxation, but without maxima even under applied dc field. Probably combining the highly isotropic Mn^{II} ions in an octahedral coordination environment with Ln^{III} ions is not a promising strategy for 3d/4f SMMs. There are few examples for such systems. It should be instructive to compare the relative contributions of h.s. Mn^{II} d^5 and Fe^{III} d^5 ions in terms of the SMM properties in 3d-4f butterfly systems. The fact that there are many more examples of Fe^{III}-4f SMM systems suggests that Mn^{II}-based compounds either have not been investigated much or
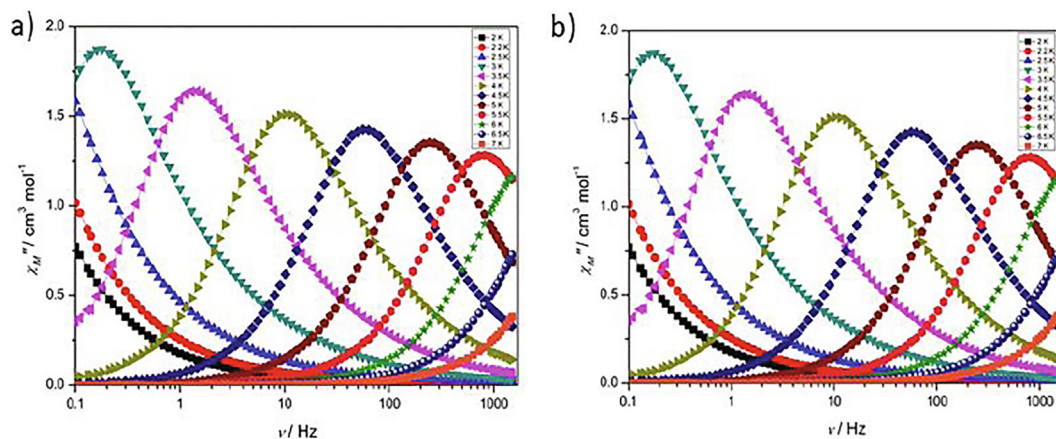
Fig. 12. Plots of χ'' vs ν for **10** $\{Cr_2^{III}Tb_2\}$ (a) and **11** $\{Cr_2^{III}Ho_2\}$ (b) under zero dc field. Reprinted with permission from [37]. Copyright (2015) American Chemical Society.
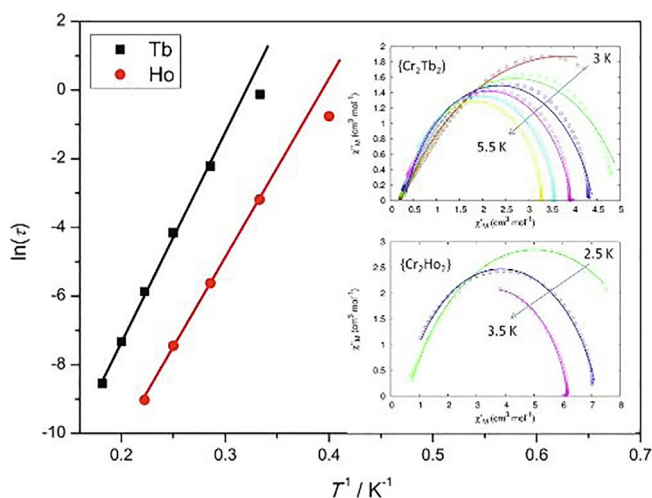
Fig. 13. Plots of $\ln(\tau)$ vs T^{-1} for compounds **10** $\{Cr_2^{III}Tb_2\}$ and **11** $\{Cr_2^{III}Ho_2\}$. The solid lines represent fits to the Arrhenius law in the thermally activated regime. (Inset) Cole-Cole plots of **10** $\{Cr_2^{III}Tb_2\}$ and **11** $\{Cr_2^{III}Ho_2\}$. The solid lines are the best fit. Reprinted with permission from [37]. Copyright (2015) American Chemical Society.

else never make it into the literature because of a lack of SMM behavior.

3.1.2.2. {Mn$_2^{III}$Ln$_2$} systems. The Brechin group reported the first Mn^{III}-4f butterfly SMM cluster, $[NMe_4]_2[Mn_2^{III}Dy_2(thme)_2 (O_2CCMe_3)_4(NO_3)_4]$ **21** obtained through the reaction of

$[Mn_3O(piv)_6(py)_3]$ with thmeH$_3$ (2-ethyl-2-(hydroxymethyl)propane-1,3-diol), Dy(NO$_3$)$_3$·xH$_2$O, and NMe$_4$OH in MeCN [46]. The compound crystallizes in the monoclinic space group $P2_1/c$. The central metallic core has a butterfly topology of **Type I** (Fig. 23) with the metal ions linked together via two thme^{3-} ligands displaying the μ_4-η^2: η^2:η^3 coordination mode. The two ligands are situated above and below the plane of these metal ions. Around the periphery, four pivalates bridge the Mn^{III} and Dy^{III} ions in their usual *syn, syn, μ*-fashion. Thus, the Mn^{III} ions are in distorted octahedral geometries (deviation value of 0.36) with the J-T axes defined by O12-Mn1-O31. The coordination spheres of the nine-coordinate Dy ions are completed by two chelating NO$_3^-$ ions, to give a capped square antiprismatic coordination geometry (CSAP-9) with a deviation value of 1.43 (Table S4 for the estimated deviations for the idealized geometries).

Dc magnetic susceptibility measurements indicate dominant antiferromagnetic interactions between the metal centers. Ac susceptibility measurements (Fig. 24 a) reveal compound **21** shows SMM behavior with U_{eff} = 15 K (10.4 cm^{-1}) and τ_0 = 3.31 × 10^{-7} s (Table 3). Furthermore, hysteresis data collected on a micro-SQUID indicate the observed hysteresis is due only to intramolecular slow relaxation of the magnetization at very low temperature measured with a scan rate of 0.07 T/s (Fig. 24b). The butterfly shape of the loops indicates significant ZF-QTM.

In 2009, the Powell group reported the compounds $[Mn_2^{III}Ln_2 (^nBudea)_2(^nBudeaH)_2(piv)_6]\cdot2MeCN$ (Ln = Ce **22** and Nd **23**) obtained from the reaction of $^nBudeaH_2$ (N-^{n}butyldiethanolamine), Ln(NO$_3$)$_3$·6H$_2$O, Mn(OAc)$_2$·4H$_2$O and pivalic acid in MeCN [47]. The complexes crystallize in the triclinic space group *P-1* and contain $\{Mn_2^{III}Ln_2\}$
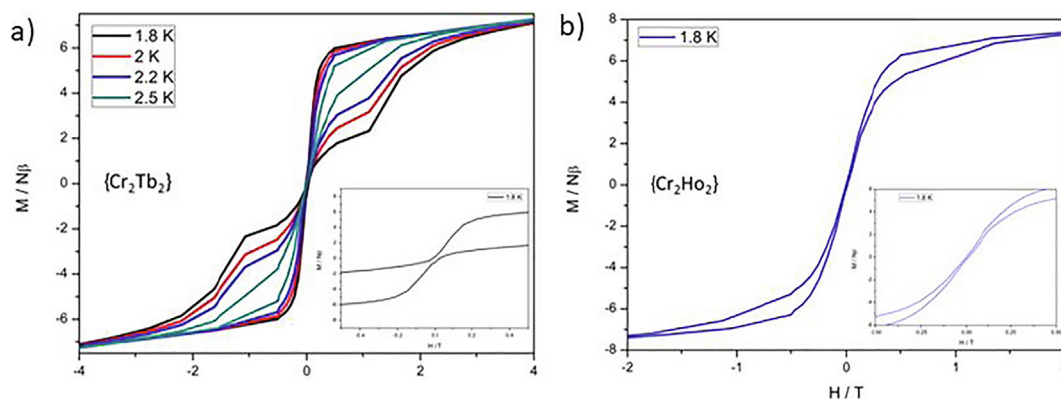
Fig. 14. Plots of M vs H for compounds **10**, Cr$_2^{III}$Tb$_2$ (a) and **11**, Cr$_2^{III}$Ho$_2$ (b) with an average sweep rate of 0.003 T/s. Reprinted with permission from [37]. Copyright (2015) American Chemical Society.
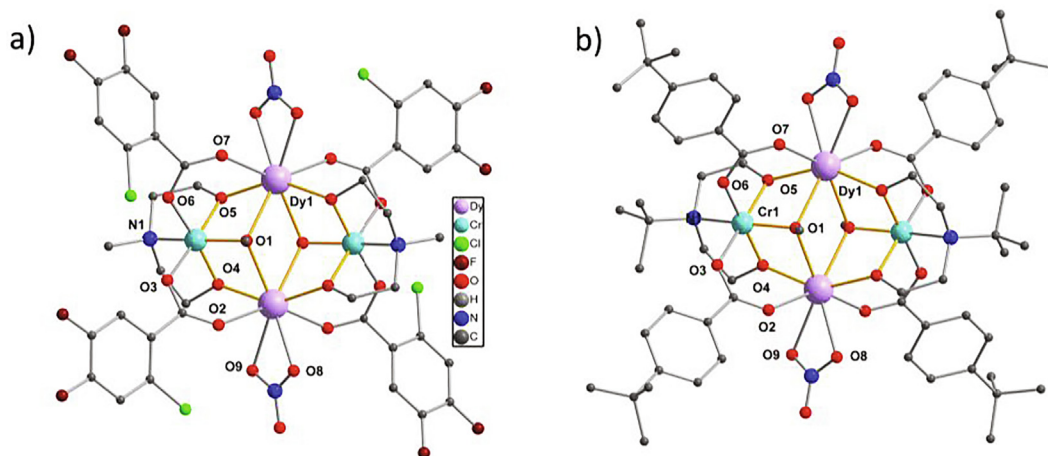
Fig. 15. Molecular structure of **14** [Cr$_2^{III}$Dy$_2$(OMe)$_{2-x}$(OH)$_x$(o-Cl-p,m-F-PhCO$_2$)$_4$(mdea)$_2$(NO$_3$)$_2$]·nMeOH (a) and **16** [Cr$_2^{III}$Dy$_2$(OMe)(OH)(p-^{t}Bu-PhCO$_2$)$_4$(^{t}Budea)$_2$(NO$_3$)$_2$]·MeOH· 2Et$_2$O (b).
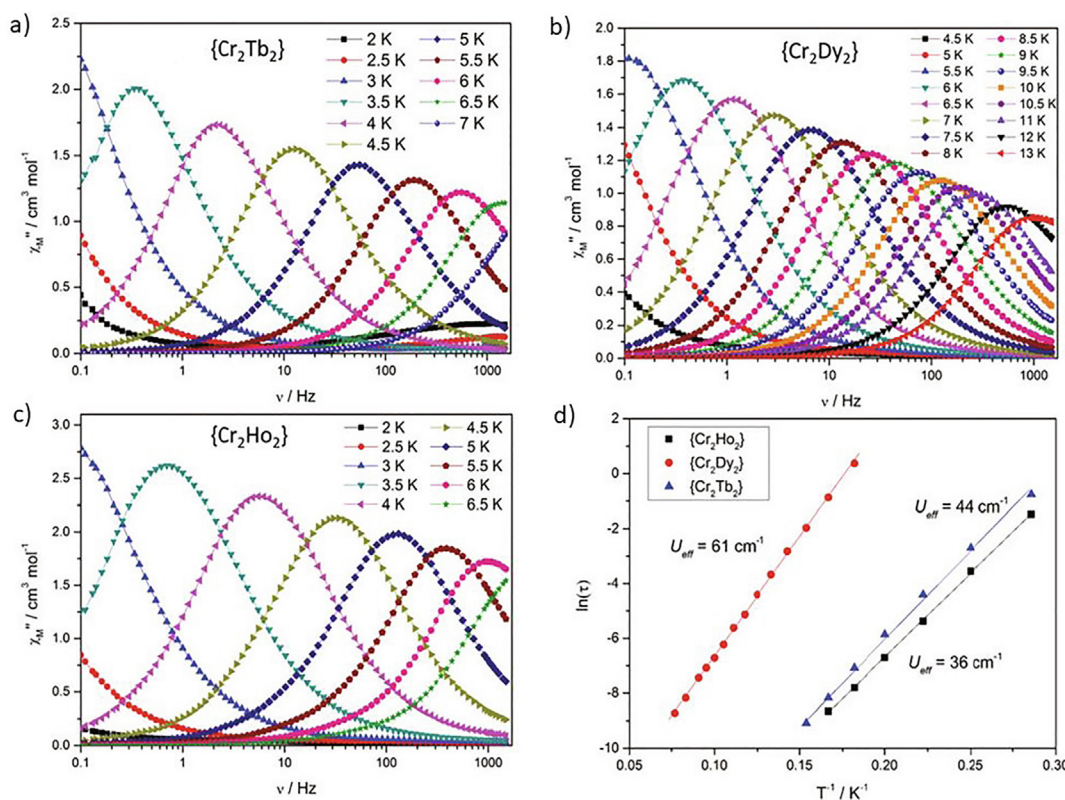
Fig. 16. Plots of χ″ vs ν for **13** (a), **14** (b) and **15** (c) under zero dc field. (lower right) Plots of ln(τ) vs T^{-1} for compounds **13–15** (d). Reprinted with permission from [41]. Copyright (2016) The Royal Society of Chemistry.

butterfly cores of **Type I** (Fig. 25). Each of two doubly-deprotonated (^{n}Budea)$^{2-}$ ligands displays the μ$_4$-η^3:η^1:η^2 coordination mode (Scheme S2). The central nitrogen is coordinated to one Mn^{III} and the two deprotonated alcohol arms bridge to the other three metal ions. Each of two singly-deprotonated (^{n}BudeaH)$^-$ ligands displays the μ$_2$-η^2:η^1:η^1 coordination mode and chelate to one Ln^{III} and bridge to a central Mn^{III}ion. Each of the two *syn, syn: μ* pivalates bridge between Mn^{III} and Ln^{III}. The unique Mn^{III} ion is six coordinate in a J-T distorted octahedral coordination geometry with the J-T axis along O1-Mn-N1′. Three oxygen atoms from one chelating pivalate and one coordinated pivalate complete the coordination spheres of the nine-coordinate Ln^{III} ion giving a capped square antiprismatic

coordination geometry (Table S4 for the estimated deviations for the idealized geometries).

Compounds **22** and **23** show overall ferromagnetic coupling. Ferromagnetic coupling between the central *3d* metal ions in **Type I** butterflies appears to be a useful strategy for enhancing the SMM parameters as has also been seen in mixed valence {Mn$_2^{II}$Mn$_2^{III}$} butterflies when the Mn^{III} ions are in the body positions with their J-T axes aligned [51] and more recently shown to be key to enhancing SMM properties in mixed *3d-4f* butterflies with body *3d* ions and their analogues [24].

Complex **22** {Mn$_2^{III}$Ce$_2$} shows slow relaxation of magnetization but without maxima (Fig. 26a), while complex **23** {Mn$_2^{III}$Nd$_2$} shows
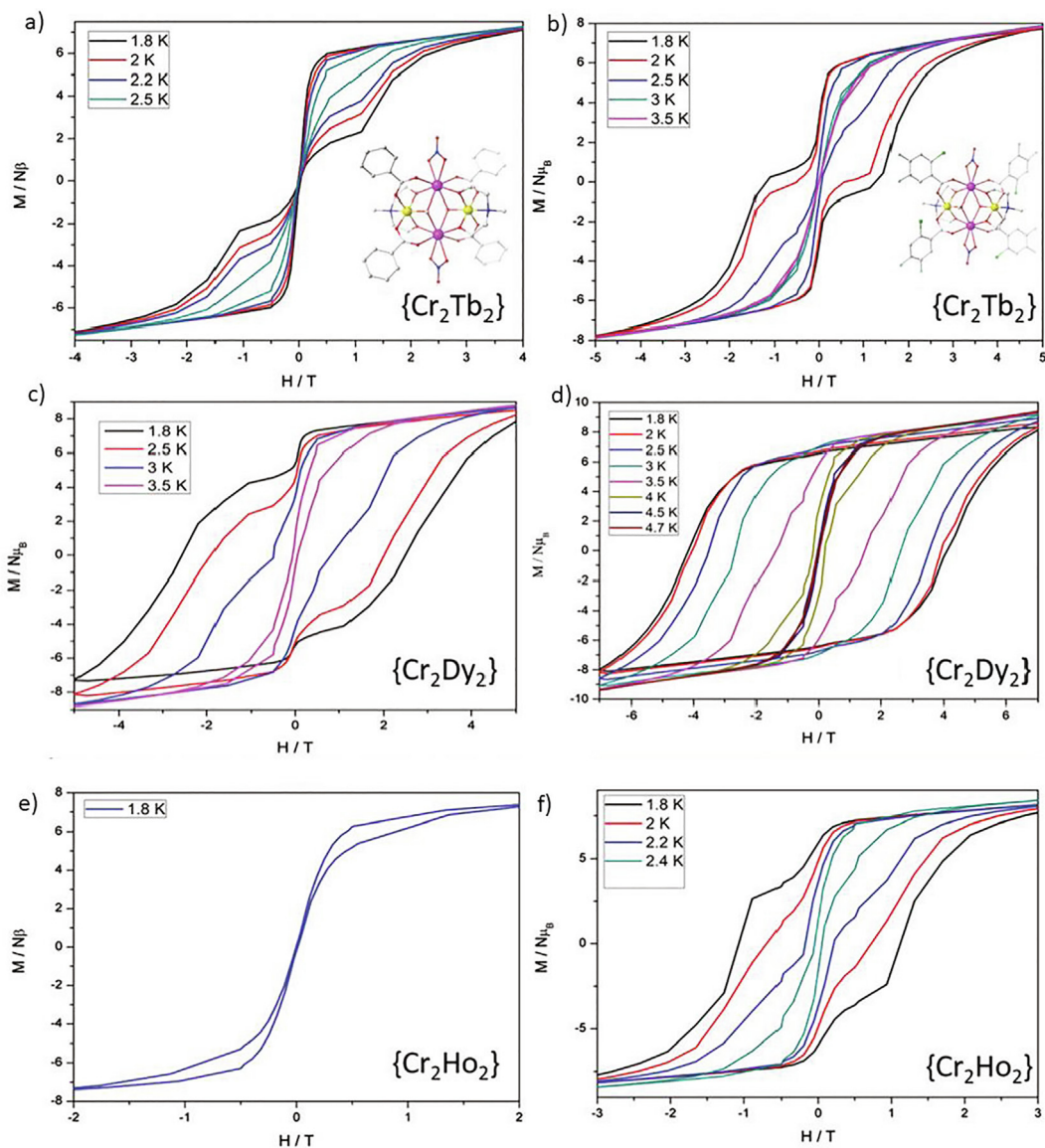
Fig. 17. Comparison of the plots of M vs H for (**10** a and **13**b), (**1**c and **14** d) and (**11** e and **15**f), with average sweep rate of 0.003 T/s. Reprinted with permission from [41]. Copyright (2016) The Royal Society of Chemistry.
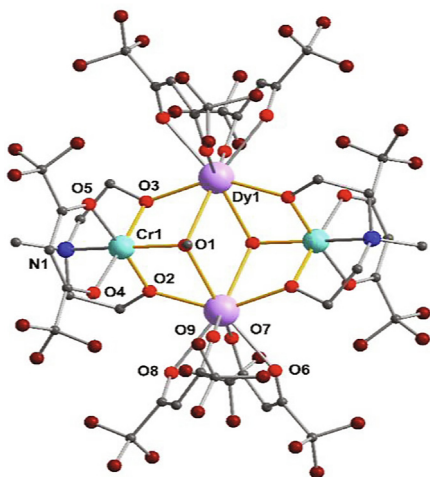
Fig. 18. Molecular structure of **17** [$Cr_2^{III}Dy_2(OMe)_2(mdea)_2(hfacac)_6$].

out-of-phase signals with clear maxima (Fig. 26b) and could be analyzed in terms of an energy barrier of 10.0 K (6.95 cm^{-1}) with τ_0 = 1. 4 × 10^{-6} s.

These results pose important questions regarding lighter versus heavier lanthanides and their anisotropies as well as possible spin contributions to the overall system under study. A simple "switchback plot" is a useful aide memoire to relating and correlating potential single ion spin, or maybe better put, number of unpaired electrons, and anisotropy characteristics (Scheme 1). From this it can be seen that Ce^{III} equates to Yb^{III} in terms of a single unpaired electron and oblate versus prolate anisotropy, whereas Nd^{III} with three unpaired electrons and an oblate anisotropy can be compared with the electronic situation of Er^{III} with a prolate anisotropy.

If the incorporation of lighter lanthanides can also lead to SMM behavior, although most of the published research on SMMs concerning 3d-4f, describes systems based on the heavier and smaller lanthanides such as Dy^{III}, Tb^{III} and Er^{III}, then Nd^{III} is a promising candidate worthy of further exploration. We note that it offers an
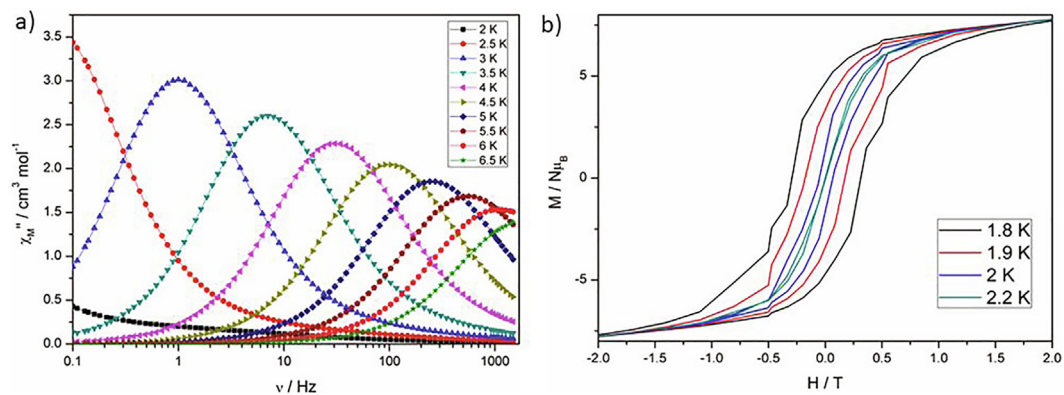
Fig. 19. Plots of χ'' vs ν (a) and Plot of M vs H for **17** [Cr$_2^{III}$Dy$_2$(OMe)$_2$(mdea)$_2$(hfacac)$_6$] (b) an average sweep rate of 0.004 T/s. Reprinted with permission from [43]. Copyright (2015) American Chemical Society.
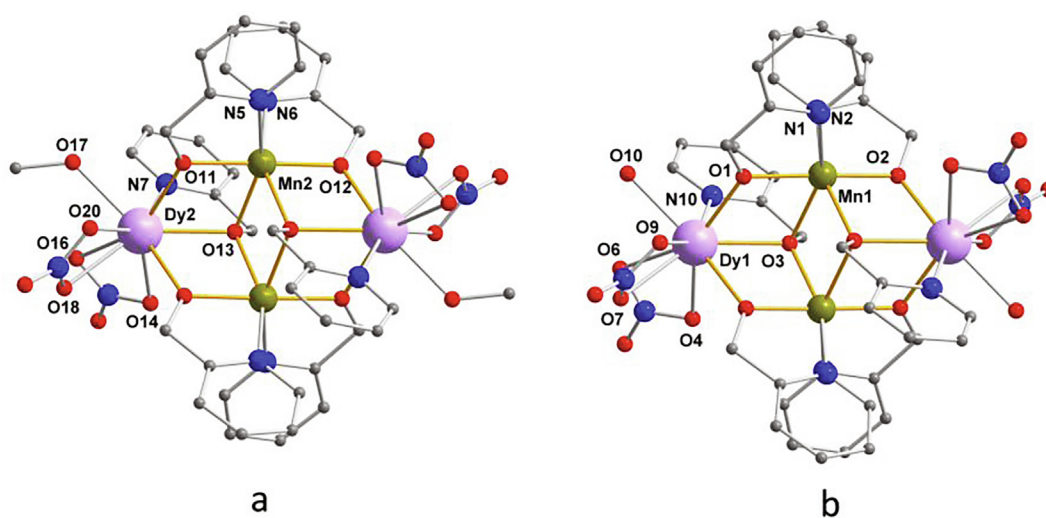
Fig. 20. Molecular structure of [Mn$_2^{II}$Ln$_2$(hmp)$_6$(NO$_3$)$_4$(MeOH)$_2$] (a) and [Mn$_2^{II}$Ln$_2$(hmp)$_6$(NO$_3$)$_4$(H$_2$O)$_2$] (b) (Ln = Tb **18**, Dy **19**).
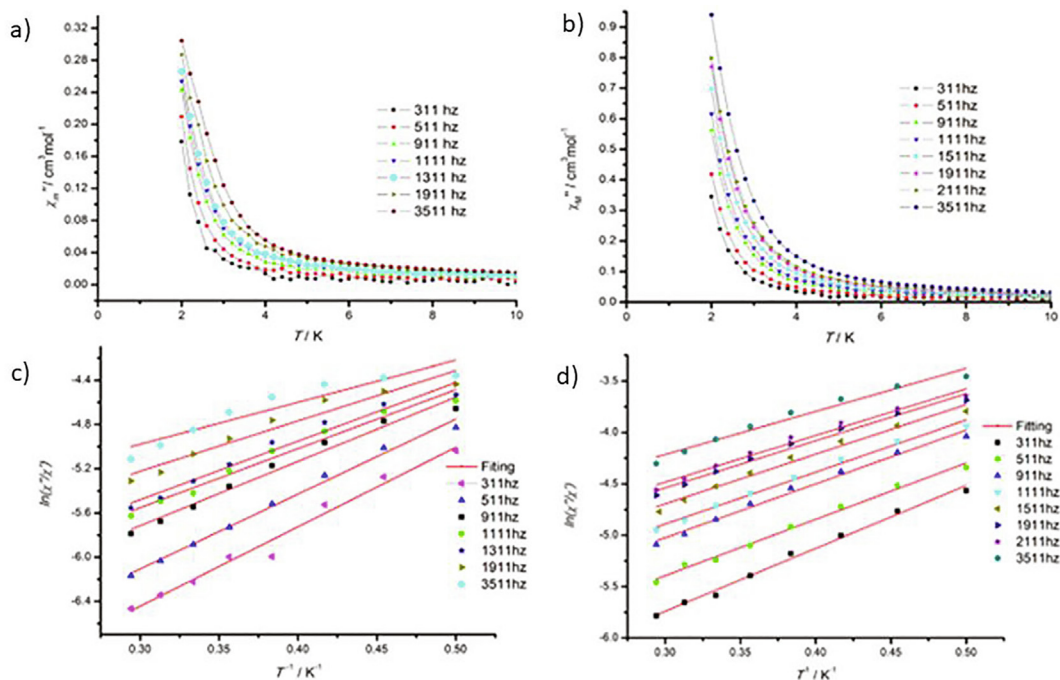
Fig. 21. Plots of χ_M'' vs T under zero field for compounds [Mn$_2^{II}$Ln$_2$(hmp)$_6$(NO$_3$)$_4$(MeOH)$_2$] plus [Mn$_2^{II}$Ln$_2$(hmp)$_6$(NO$_3$)$_4$(H$_2$O)$_2$] Ln = Dy **18** (a) and Ln = Tb **19** (b). Plots of ln(χ''/χ') vs T^{-1} for compounds **18** (c) and **19** (d), the solid lines represent the fitting in the range 2.0–3.4 K. Reprinted with permission from [44]. Copyright (2016) Elsevier.

Fig. 22. Molecular structure of **20** [Mn$_2^{II}$Dy$_2$(L2)$_4$(NO$_3$)$_2$(DMF)$_2$].

Fig. 23. The structure of the anion of complex **21** [NMe$_4$]$_2$[Mn$_2^{III}$Dy$_2$(thme)$_2$(piv)$_4$(NO$_3$)$_4$]. The green lines represent the J-T axes.

Fig. 25. Molecular structure of **22** [Mn$_2^{III}$Ce$_2$(^{n}Budea)$_2$(^{n}BudeaH)$_2$(piv)$_6$]·2MeCN. The green lines represent the J-T axes.

coordinate with distorted octahedral geometry including the expected J-T distortion of an axial elongation along O3-Mn1′-N2, but with a significant deviation from a linear 180° central angle. The coordination sphere of the nine coordinate Dy^{III} ions is completed by two chelating nitrates and two H$_2$O molecules giving a distorted muffin coordination geometry (Table S4 for the estimated deviations for the idealized geometries).

Dc susceptibility measurements reveal that the coupling is predominantly antiferromagnetic in both compounds **24** and **25**. Ac susceptibility measurements show slow relaxation of the magnetization in zero dc field, but without maxima for both **24** and **25** (Fig. 28). Thus, no energy barriers were extracted.

Vaz et al reported another {Mn$_2^{III}$Ln$_2$} butterfly system formed by reaction of MnCl$_2$, Ln(NO$_3$)$_3$, Hdpm (2,2,6,6-tetramethyl-3,5-heptanodione) and 30% MeONa solution in MeOH with formula of [Mn$_2^{III}$-Dy$_2$(dpm)$_6$(MeO)$_6$] **26** and [Mn$_2^{III}$Tb$_2$(dpm)$_6$(MeO)$_6$(MeOH)$_2$] **27** [49]. These two compounds are similar and crystallize in the triclinic space group *P-1*. The molecular structures of these two clusters consist of a butterfly {Mn$_2^{III}$Ln$_2$} core bridged by two μ$_3$-OH$^-$ and four μ$_2$-OH$^-$ in **Type I** (Fig. 29). Each six coordinate Mn^{III} ion is further coordinated by one β-diketonate leading to a distorted octahedral environment with J-T distortion. The lanthanide ions are further coordinated by two β-diketonate anions and in **26** are seven coordinate with pentagonal bipyramidal geometry and, as the result of an additional coordinating MeOH ligand, eight coordinate in **27** with square anti-prismatic geometry (Table S4 for the estimated deviations for the idealized geometries).

Ac susceptibility measurements on both compounds show slow relaxation without maxima even under applied dc field (Fig. 30).

alternative oblate anisotropy ellipsoid for a configuration with 3 unpaired electrons compared with the prolate ellipsoid of Er^{III}.

The Christou group reported [Mn$_2^{III}$Ln$_2$(OH)$_2$(NO$_3$)$_4$(hmp)$_4$(H$_2$-O)$_4$](NO$_3$)$_2$, (Ln = Dy **24** and Tb **25**) [48] formed by reaction of Mn (ClO$_4$)$_2$·6H$_2$O with hmpH ((2-hydroxymethyl)pyridine), NEt$_3$, and Ln(NO$_3$)$_3$·6H$_2$O in MeCN. Compounds **24** and **25** are isostructural, crystallizing in the monoclinic space group *C2/c* with an inversion center in the middle of the cation. It possesses a [Mn$_2^{III}$Ln$_2$(μ$_3$-OH)$_2$]$^{10+}$ core consisting of a {Mn$_2^{III}$Ln$_2$} planar **Type I** butterfly (Fig. 27). The core is additionally chelated and bridged by four μ$_2$-η^1:η^2 hmp$^-$ groups (Scheme S2). Thus the Mn^{III} atoms are six-

Fig. 24. Plots of χ″ vs T under zero dc field (a) and plots of M vs H with a scan rate of 0.07 T/s for **21** (b). Reprinted with permission from [46]. Copyright (2005) The Royal Society of Chemistry.
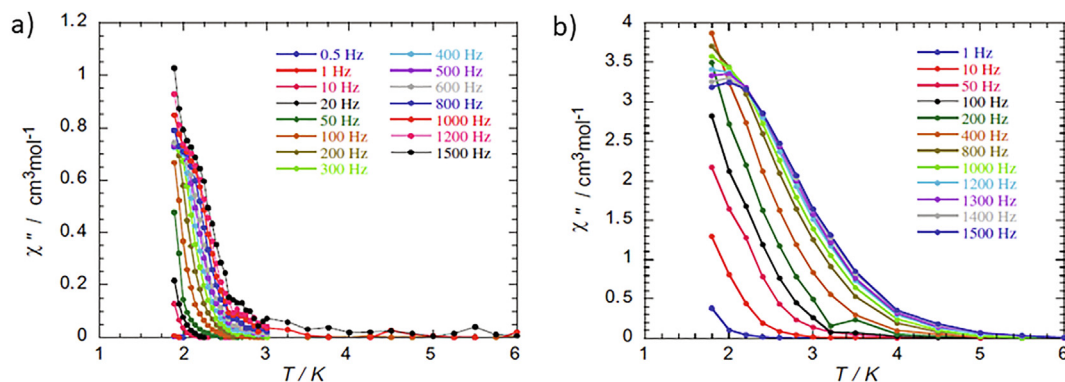
Fig. 26. Plots of χ″ vs T under zero dc field for compound **22** {Mn$_2^{III}$Ce$_2$} (a) and **23** {Mn$_2^{III}$Nd$_2$} (b). Reprinted with permission from [47]. Copyright (2009) Elsevier.

Scheme 1. The relationship amongst the Ln^{III} ions. O = Oblate and P = Prolate anisotropy. The central row of numbers gives the number of unpaired electrons in the ground state of the free ion.
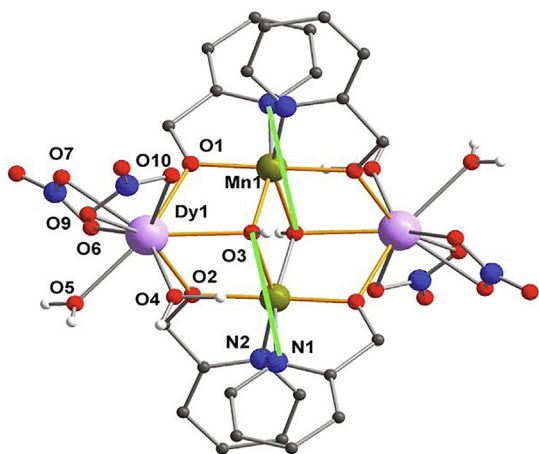
Fig. 27. Molecular structure of **24** [Mn$_2^{III}$Dy$_2$(OH)$_2$(NO$_3$)$_4$(hmp)$_4$(H$_2$O)$_4$](NO$_3$). The green lines represent the J-T axes.

For both compounds, there is a signature of QTM under zero dc field evidenced by the in-phase and out-of-phase ac signals moving to higher temperatures under a small applied dc field.

In 2015, Winpenny's group reported the {Mn$_2^{III}$Ln$_2$} butterfly, [Et$_3$NH]$_2$[Mn$_2^{III}$Ln$_2$(O)$_2$(Piv)$_{10}$] **28** formed through reaction of [Mn$_2^{II}$(Piv)$_4$EtOH]$_n$, [Dy$_2$(Piv)$_6$(HPiv)$_6$], and Et$_3$N in MeCN [50]. The anionic cluster is composed of a {Mn$_2^{III}$Dy$_2$} **Type I** butterfly core bridged by two μ$_3$-O^{2-} (Fig. 31). The metal core is further bridged and chelated by ten piv$^-$ ligands displaying three different coordination modes: η^0:η^1;μ^2:η^2:η^1 and *syn syn*: η^1:η^2. The resulting dinegative charge is balanced by two [Et$_3$NH]$^+$ cations. The six coordinate Mn^{III} ion shows elongated octahedral geometry due to a J-T

elongation along the O4-M-O10′ axis. The Ln^{III} ion is eight coordinate adopting a distorted square antiprismatic coordination geometry (SAP-8) (Table S4 for the estimated deviations for the idealized geometries).

Ac susceptibility measurements indicate compound **28** is a typical SMM with clear maxima in the out of phase ac susceptibilities (Fig. 32a and b). Fits for the data extracted from the χ″ vs ν data to an Arrhenius law gave U_{eff} = 29 K (20.2 cm^{-1}) and τ$_0$ = 4.6 × 10^{-6} s (Fig. 32d). As can be seen from the ln(τ) vs T^{-1} data, there are clearly further relaxation processes to be taken into account, but at the time of publication it was not common practice to use the multiple relaxation processes equation to fit the data. Fitting the Cole-Cole plots gave α parameters in the range 0.2–0.3, suggesting a wide distribution of relaxation times (Fig. 32c).

More recently, the Powell group reported another [Mn$_2^{III}$Dy$_2$(OH)$_2$(*p*-Me-PhCO$_2$)$_6$(pdea)$_2$] ·2MeCN·2MeOH **29** butterfly complex of **Type I** with the pdeaH$_2$ ligand (Fig. 33) [24]. The high spin distorted octahedral Mn^{III} ions in {Mn$_2^{III}$Dy$_2$} show an axial J-T elongation along O4–Mn–O1′. The ferromagnetically coupled coordination cluster shows typical SMM behavior with no significant efficient ZF-QTM (Fig. 34). The Arrhenius law is a straight line over the whole temperature range 1.8–2.4 K with U_{eff} = 19.32 K (13.4 cm^{-1}) and τ$_0$ = 5.64 × 10^{-8} s (Table 3). Fitting the relatively symmetrical semicircles Cole-Cole plots gave small α values in the range 0.067–0.093 (Fig. 35), indicating a narrow distribution of relaxation times within this single relaxation process. *Ab* initio calculations suggest that the ferromagnetic coupling between the Mn^{III} and Dy^{III} ions plays a key role in directing the nature of the SMM properties observed (Table 4).

Summary: The {Mn$_2^{III}$Ln$_2$} systems containing J-T distorted Mn^{III} ions show better SMM performance compared to the {Mn$_2^{II}$Ln$_2$} systems but with only two examples for {Mn$_2^{III}$Dy$_2$} butterflies showing slow relaxation which can be analyzed in terms of an effective energy barrier. However, it is hard to correlate the J-T effect of the Mn^{III} ions to the behavior of the whole molecule. The orientation of the J-T axes within the butterfly motif is probably one important factor. It is perhaps noteworthy that for **28** {Mn$_2^{III}$Dy$_2$} the J-T axes are in an almost perpendicular orientation to those in **29** {Mn$_2^{III}$Dy$_2$}. It is also not clear what the effect of an elongation versus a compression along the J-T axis might make. The nature of the ligand and coligand and lastly the nature of the Ln^{III} e.g. as shown for **26** and **27** (**26** [Mn$_2^{III}$Dy$_2$(dpm)$_6$(MeO)$_6$] and **27** [Mn$_2^{III}$Tb$_2$(dpm)$_6$(MeO)$_6$ (MeOH)$_2$]) can all have further influences on the SMM properties.

3.1.3. {Fe$_2^{III}$Ln$_2$} systems

As mentioned before, the {Fe$_2^{III}$Ln$_2$} butterfly clusters have been reviewed elsewhere [26] and here we list the parameters of the compounds showing SMM properties for comparison with the other
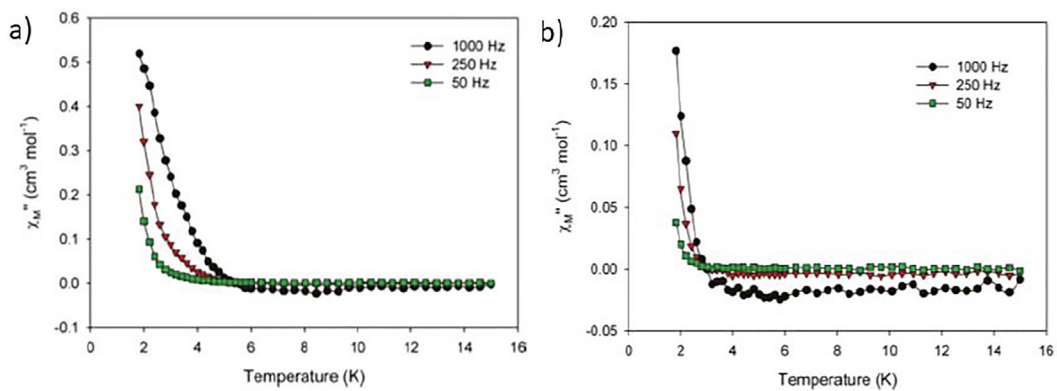
Fig. 28. Plots of χ'' vs T under zero dc field for **24** (a) and **25** (b). Reprinted with permission from [48]. Copyright (2011) American Chemical Society.
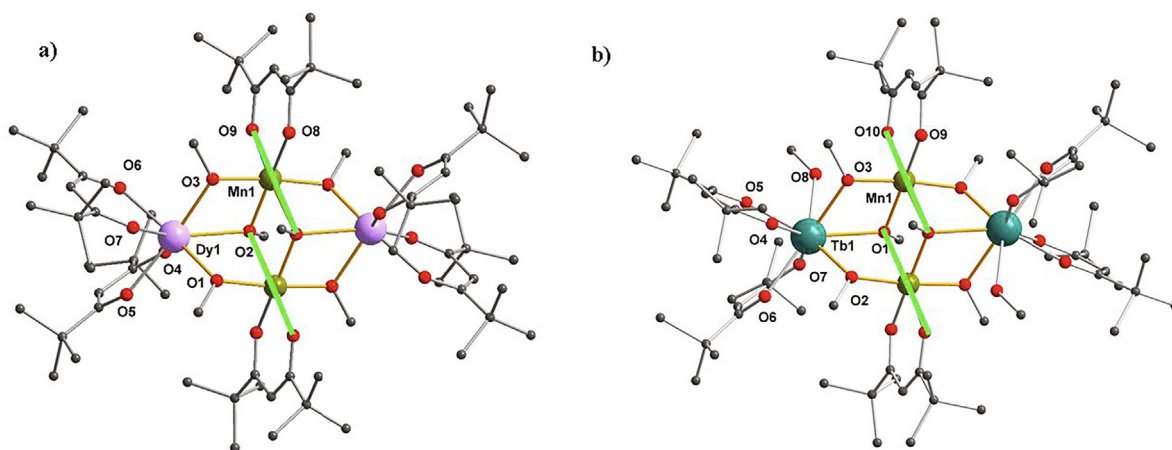
Fig. 29. Molecular structures of **26** [Mn$_2^{III}$Dy$_2$(dpm)$_6$(MeO)$_6$] (a) and **27** [Mn$_2^{III}$Tb$_2$(dpm)$_6$(MeO)$_6$(MeOH)$_2$] (b). The green lines represent the J-T axes.
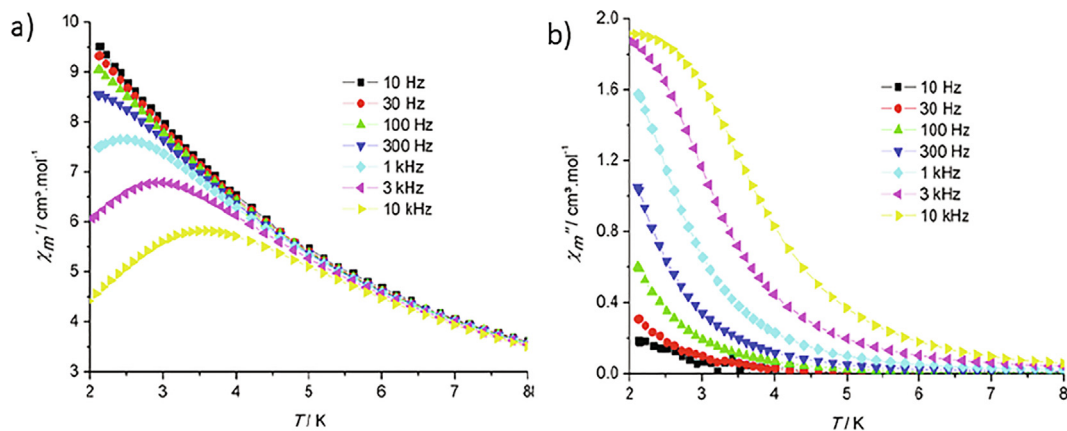
Fig. 30. Plots of χ' (a) and χ'' (b) vs T under zero field for compound **26**, [Mn$_2^{III}$Dy$_2$(dpm)$_6$(MeO)$_6$]. Reprinted with permission from [49]. Copyright (2013) American Chemical Society.

compounds discussed in the present review (Tables 4, 5 and S5 for the estimated deviations for the idealized geometries). It is instructive to compare the available *ab initio* calculations on these with the other butterflies in this review. Furthermore, it is interesting that there are very many more h.s. Fe^{III} than Mn^{II} SMM butterflies so far discovered. In this system, SMM behavior is often only observed under application of small external dc fields, which

indicates that many compounds are not particularly impressive SMMs. Nevertheless, this fact actually allows for an easier identification of the parameters which enhance SMM performance and we can see that the **Type I** [Fe$_2^{III}$Ln$_2$(OR$_1$)$_2$(R$_2$-dea)$_2$(R$_3$-PhCO$_2$)$_6$] system provides a robust, highly tunable and sensitive compound making it an ideal "test bed" for exploring magneto-structural correlations.
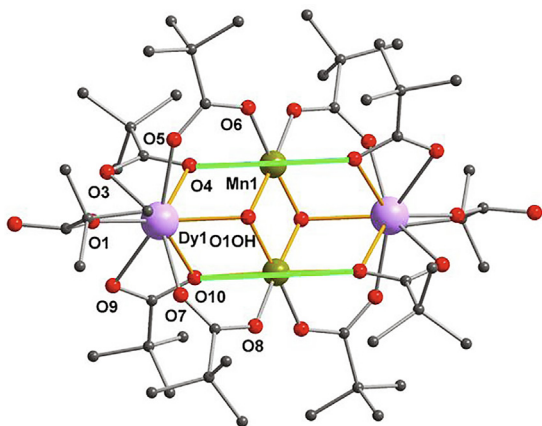
Fig. 31. Molecular structure of **28** [Et$_3$NH]$_2$[Mn$_2^{III}$Dy$_2$(O)$_2$(Piv)$_{10}$]. The green lines represent the J-T axes.
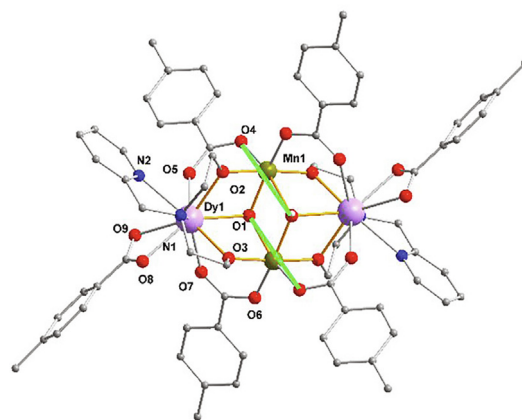
Fig. 33. Molecular structural of **29** {Mn$_2^{III}$Dy$_2$}. The green lines represent the J-T axes.

3.1.4. {Co$_2^{II}$Ln$_2$} systems

Costes's group reported the first Co^{II}-4f butterfly compound showing slow relaxation of the magnetization [58] in 2011, namely [Co$_2^{II}$Gd$_2$(OH)$_2$(ovan)$_4$(NO$_3$)$_4$]·(acetone) **41** (Hovan = *o*-vanillin) through the reaction of the cobalt complex [(ovan)$_2$Co^{II}(H$_2$O)$_2$] with Gd^{III} ions. It crystallizes in the triclinic space group *P-1* with a {Co$_2$-Gd$_2$} **Type I** butterfly core motif (Fig. 36) bridged by two μ$_3$-OH$^-$ ligands. The periphery of the core is further bridged and chelated by four deprotonated ovan ligands adopting a η^1:η^2:η2:μ$_2$ coordination mode. Thus the Co^{II} ions are six coordinate in distorted octahedral geometry and each of two Gd^{III} ions is further chelated by two NO$_3^-$ to achieve nine coordinate in distorted MFF-9 (muffin) geometry with a deviation value of 2.24 (Table S6 for the estimated deviations for the idealized geometries).

The dc susceptibility measurements indicate an overall ferromagnetic interaction in **41** and slow relaxation of the magnetization was detected from the open hysteresis loops at low temperatures measured using a micro-SQUID (Fig. 37). The molecular nature of the relaxation was confirmed from the temperature and sweep-rate data, but zero-field fast quantum tunneling meant that no U_{eff} values could be extracted.

One year later the Powell group reported the first Co^{II}-4f butterfly system showing classic SMM properties, i.e. no ZF-QTM as seen from maxima in the ac-susceptibility signals measured under zero field, [Co$_2^{II}$Dy$_2$(L1)$_4$(NO$_3$)$_2$(THF)$_2$] **42**. This was formed by recrystallizing the red powder obtained from reaction in MeOH of Dy(NO$_3$)$_3$·6H$_2$O, Co(NO$_3$)$_2$·6H$_2$O, H$_2$L and Et$_3$N from THF [59]. Compound **42** crystallizes in the triclinic space group *P-1*. The molecular structure
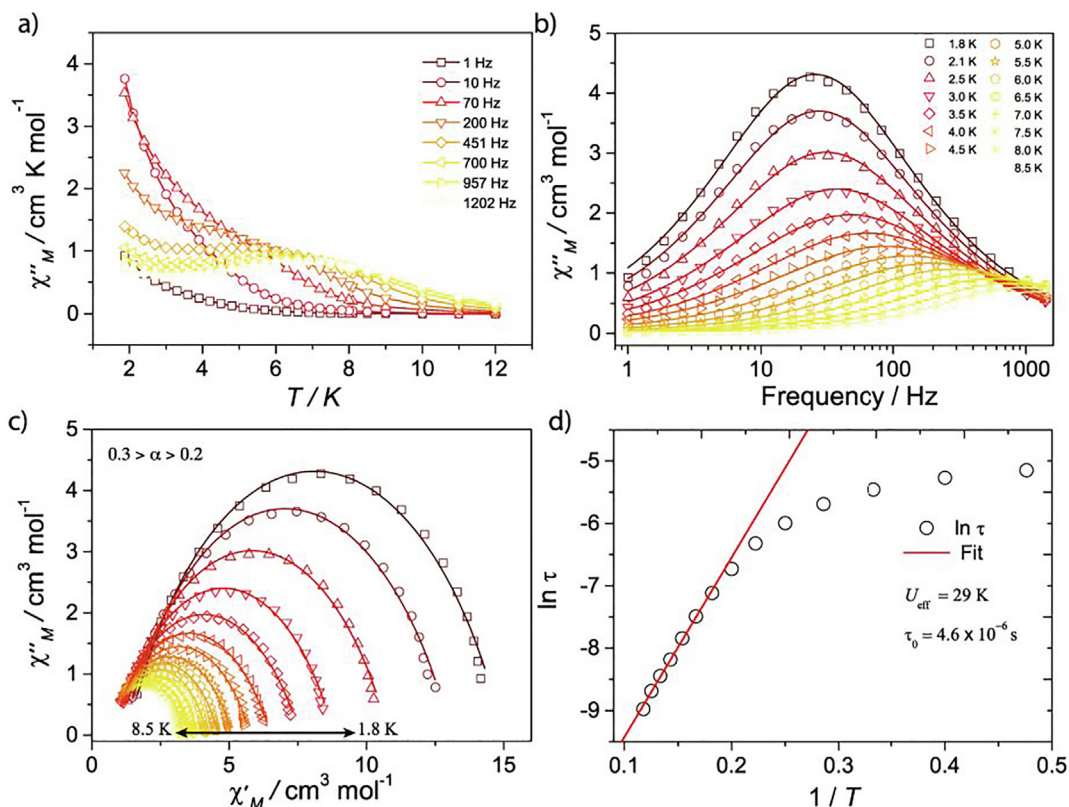
Fig. 32. (a) Plots of χ″ vs T, (b) plts of χ″ vs ν, (c) Cole-Cole plots, and (d) plot of ln(τ) vs T^{-1} for **28** [Et$_3$NH]$_2$[Mn$_2^{III}$Dy$_2$(O)$_2$(Piv)$_{10}$] under zero dc field. Reprinted with permission from [50]. Copyright (2015) American Chemical Society.
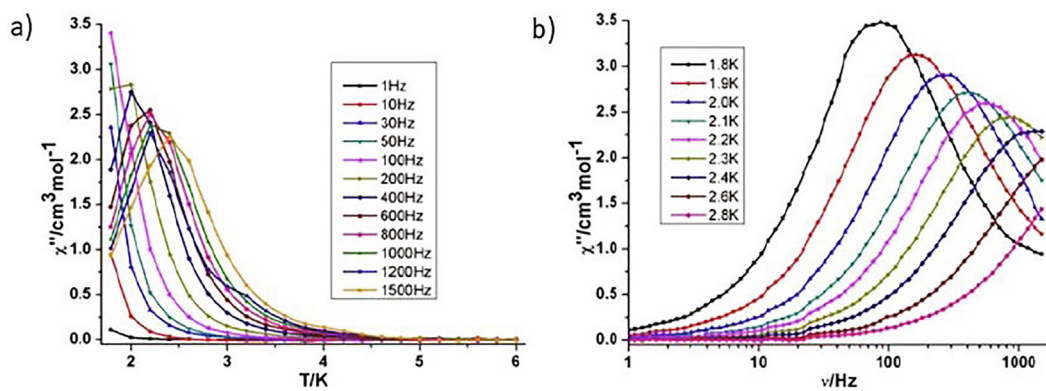
Fig. 34. Plots of χ'' vs T (a) and ν (b) under zero dc field for compound **29** {Mn$_2^{III}$Dy$_2$}.Reprinted with permission from [24]. Copyright (2019) The Royal Society of Chemistry.
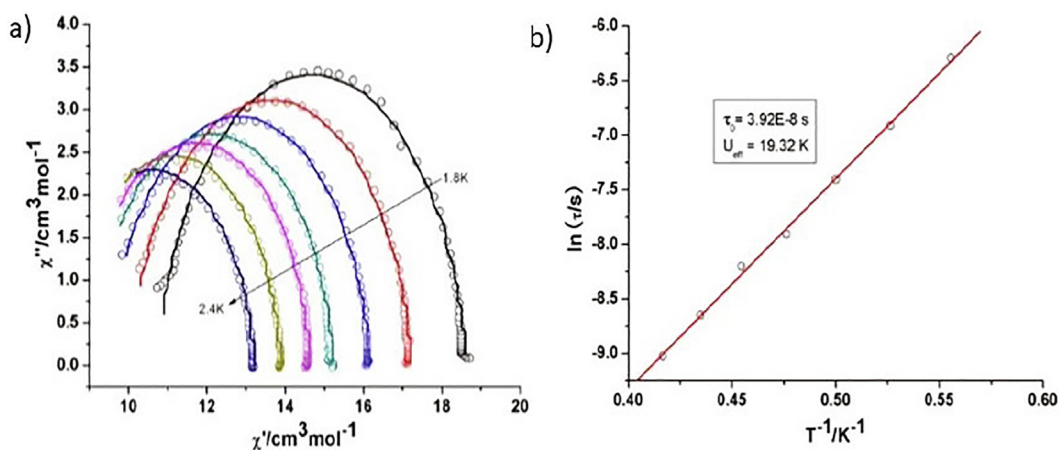
Fig. 35. Cole-Cole plots (a) and plot of ln(τ) vs T^{-1} under zero dc field (b) for **29** {Mn$_2^{III}$Dy$_2$}. Reprinted with permission from [24]. Copyright (2019) The Royal Society of Chemistry.
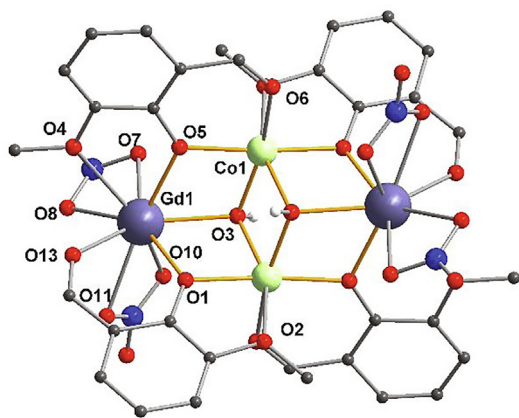
Fig. 36. The molecular structure of compound **41** [Co$_2^{II}$Gd$_2$(OH)$_2$(ovan)$_4$(NO$_3$)$_4$].

is similar to that of the {Mn$_2^{II}$Dy$_2$} compound, **20** with small differences in the details of the ligands (Fig. 38).

Complex **42** shows overall ferromagnetic interactions between the metal centers and characteristic SMM behavior (Fig. 39a). A fit to the ln(τ)vs T^{-1} plots gave two thermally activated regimes with $U_{eff}1$ = 16.0 K (11.1 cm^{-1}) and $\tau_0 1$ = 7.7 × 10^{-4} s in the temperature range 1.6–8 K and $U_{eff}2$ = 118.3 K (82.2 cm^{-1}) and $\tau_0 2$ = 6.2 × 10^{-7} s (18–22 K) (Fig. 40a). The compound also shows open hysteresis curves measured on bulk powder samples and

the data from these measurements in addition to data from ac-susceptibility measurements were fitted according to two Orbach processes obeying Arrhenius laws. These findings could be substantiated from *ab initio* calculations with the conclusion that the two relaxation processes could be attributed to the single-ion anisotropy of the Dy^{III} ions at higher temperature with a crossover to molecular exchanged-based anisotropy in the low temperature regime.

Through fine-tuning of the reaction conditions, two analogues, [Co$_2^{II}$Dy$_2$(L1)$_4$(NO$_3$)$_2$(MeOH)$_2$]·2CH$_2$Cl$_2$ **43** and [Co$_2^{II}$Dy$_2$(L1)$_4$(NO$_3$)$_2$ (DMF)$_2$]·2C$_2$H$_6$CO **44**, of compound **42** were formed [60]. These crystallize isomorphically in the monoclinic space group *P2$_1$/c*. The significant differences for these compounds compared with **42** are the nature of the coordinated solvents and lattice solvent molecules (Fig. 38). The structures all have very similar bond lengths and angles but display slightly different static magnetic behavior. The ac susceptibilities measurements show that **43** and **44** are typical SMMs under zero dc field (Fig. 39). Both compounds show two thermally activated regimes, $U_{eff}1$ = 17.9 K (12.4 cm^{-1}) and $\tau_0 1$ = 2.3 × 10^{-4} s in the temperature range 2.0–8.0 K and $U_{eff}2$ = 104.8 K (72.8 cm^{-1}) and $\tau_0 2$ = 9.2 × 10^{-7} s between 18 and 22 K for complex **43** and $U_{eff}1$ = 17.5 K (12.2 cm^{-1}) and $\tau_0 1$ = 1.5 × 10^{-4} s in the temperature range 2.0–8.0 K and $U_{eff}2$ = 94.5 K (65.7 cm^{-1}) and $\tau_0 2$ = 1. 2 × 10^{-6} s (Table 6) between 17 and 21 K for complex **44** (Fig. 40).

It seems that, the coordinating solvent on the Co^{II} has an influence on the strength of the exchange interaction between Co^{II} and Dy^{III} ions, which further affects the relaxation of the Dy^{III} ions as seen from the relative values of $U_{eff}1$, and $U_{eff}2$. For **41** the Y^{III} ana-
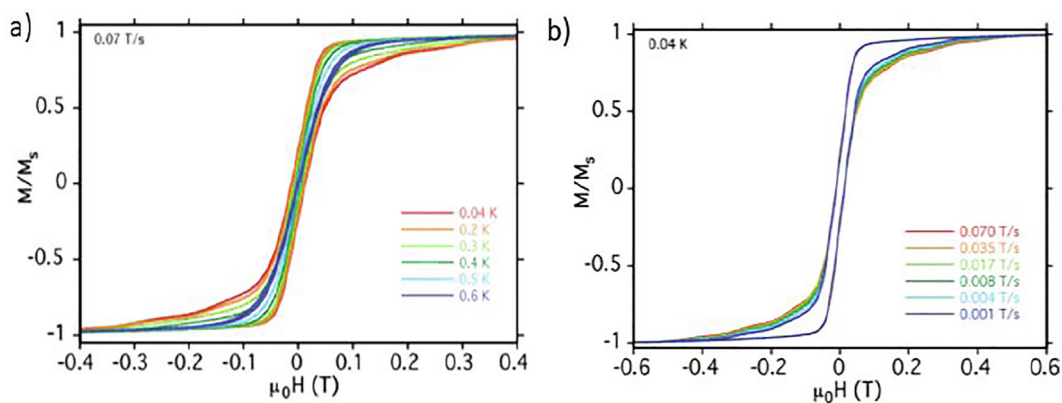
Fig. 37. Single-crystal plots of M vs H for complex **41** at several temperatures with a scan rate of 0.07 T/s (a), and at 0.04 K for several field sweep rates (b). M is normalized to its saturation value at 1.4 T. Reprinted with permission from [58]. Copyright (2011) The Royal Society of Chemistry.
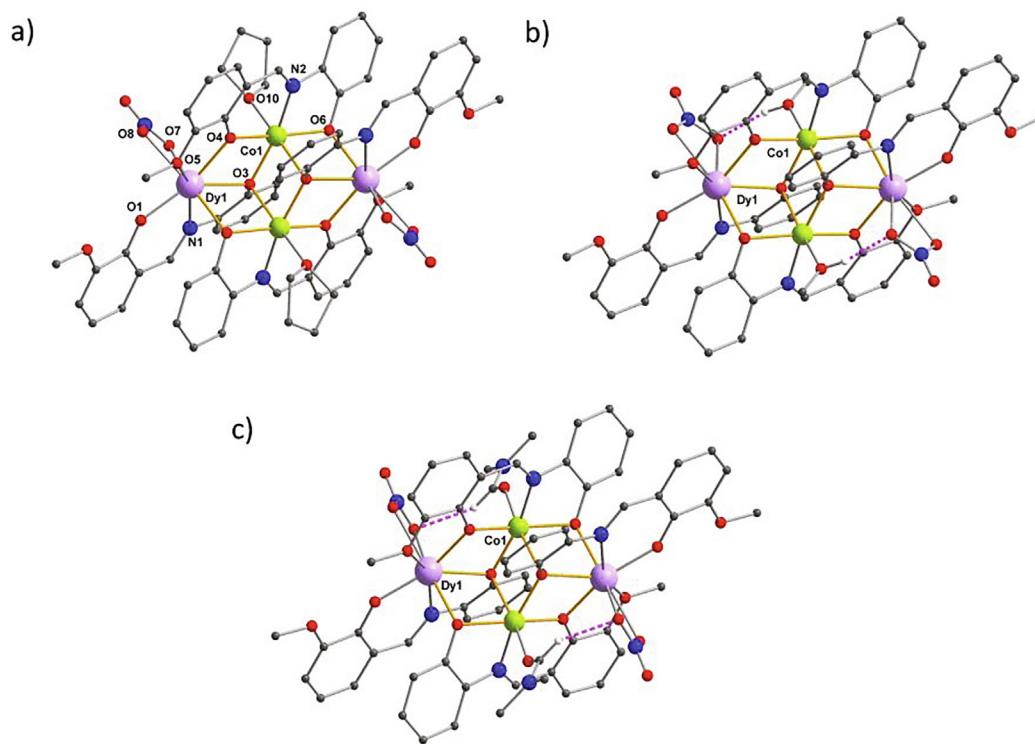
Fig. 38. Molecular structures of **42** [Co$_2^{II}$Dy$_2$(L1)$_4$(NO$_3$)$_2$(THF)$_2$] (a), **43** [Co$_2^{II}$Dy$_2$(L1)$_4$(NO$_3$)$_2$(MeOH)$_2$]·2CH$_2$Cl$_2$ (b), and **44** [Co$_2^{II}$Dy$_2$(L1)$_4$(NO$_3$)$_2$(DMF)$_2$]·2C$_2$H$_6$CO (c), emphasizing the interaction between the terminal ligand on Co(1) (THF in **42**, MeOH in **43**, DMF in **44**). The atom numbering is the same in compounds **42**–**44** and given only for compound **42**. O-H···O and C-HO hydrogen bonding shown as dashed pink lines.
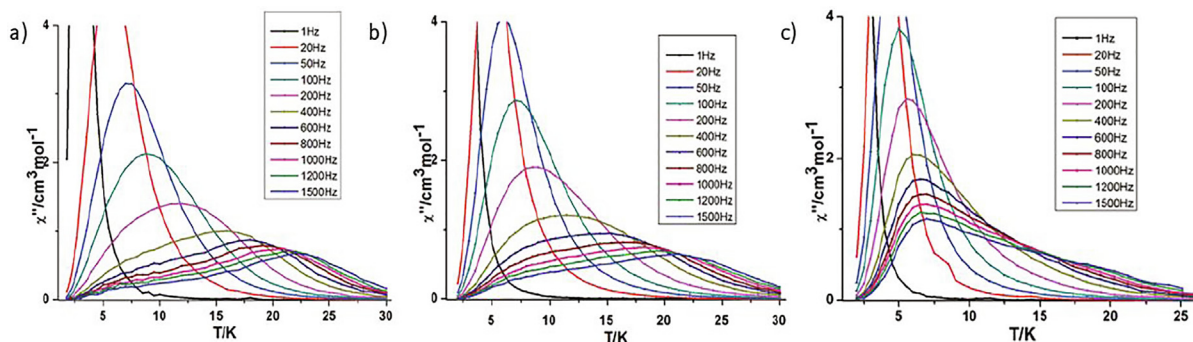
Fig. 39. Plots χ″ vs T for **42** [Co$_2^{II}$Dy$_2$(L1)$_4$(NO$_3$)$_2$(THF)$_2$] (a), **43** [Co$_2^{II}$Dy$_2$(L)$_4$(NO$_3$)$_2$(MeOH)$_2$]·2CH$_2$Cl$_2$ (b), and **44** [Co$_2^{II}$Dy$_2$(L)$_4$(NO$_3$)$_2$(DMF)$_2$]·2C$_2$H$_6$CO (c), under zero dc field. Reprinted with permission from [59,60]. Copyright (2012) Wiley-VCH Verlag GmbH& Co. KGaA and Copyright (2017) The Royal Society of Chemistry.
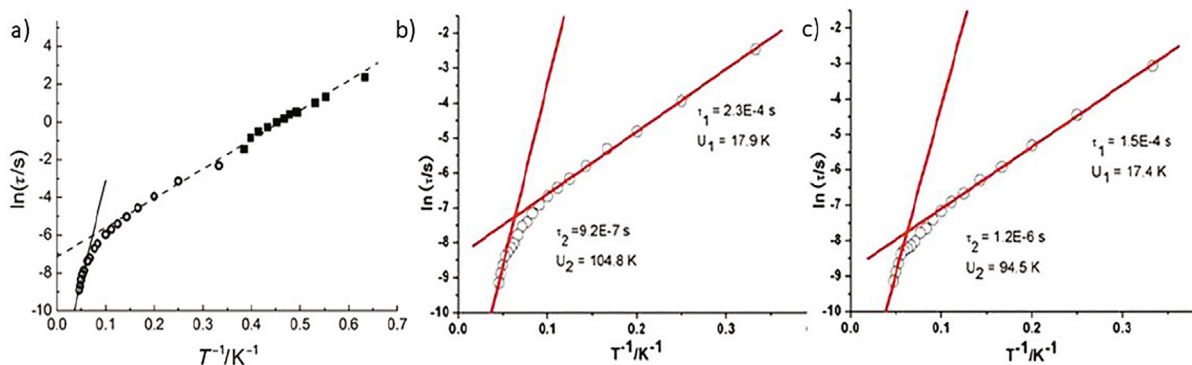
Fig. 40. Arrhenius analysis of **42** [Co$_2^{II}$Dy$_2$(L1)$_4$(NO$_3$)$_2$(THF)$_2$] (a), **43** [Co$_2^{II}$Dy$_2$(L1)$_4$(NO$_3$)$_2$(MeOH)$_2$]·2CH$_2$Cl$_2$ (b), and **44** [Co$_2^{II}$Dy$_2$(L1)$_4$(NO$_3$)$_2$(DMF)$_2$]·2C$_2$H$_6$CO (c). Reprinted with permission from [59,60]. Copyright (2012) Wiley-VCH Verlag GmbH& Co. KGaA and Copyright (2017) The Royal Society of Chemistry.
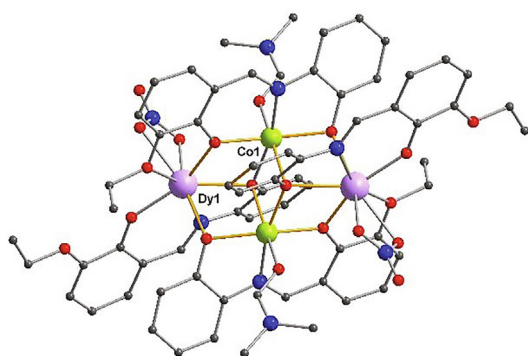
Fig. 41. Molecular structures of **45** [Co$_2^{II}$Dy$_2$(L1)$_4$(NO$_3$)$_2$(DMF)$_2$].

logue shows no ac signals at zero field. For the Zn^{II} analogue of **42** (see Section 3.2.1) deletion of the 3d contribution leads to an enhanced barrier of U_{eff} = 140.4 K at zero field with similar relaxation time but now the data must be fit taking Raman and QTM processes into account. The Arrhenius plots clearly show that the energy barriers of exchange-coupled regime at low temperature are very similar for compounds **42**–**44**, whereas the energy barriers of the single ion Dy^{III} high temperature process are different. This was the first time where it was observed that the effects of the anisotropy of a single Dy^{III} can be steered through changes to the nature of one coordinated solvent site on the Co^{II} ions within these [Co$_2^{II}$Dy$_2$(L1)$_4$(NO$_3$)$_2$(solv)$_2$] butterfly systems.

Song's group reported another analogue, [Co$_2^{II}$Dy$_2$(L2)$_4$(NO$_3$)$_2$(DMF)$_2$]·2DMF (**45**) [45]. The molecular structure of **45** is similar to **44**, except that the coordinating ligands are H$_2$L2 (((E)-2-(2-hydroxy-3-ethoxybenzyli-deneamino)phenol) instead of H$_2$L1 (((E)-2-(2-hydroxy-3-methoxybenzylideneamino)phenol), and the two additional acetone molecules found in the lattice for **44** are replaced by two DMF molecules (Fig. 41). The bond lengths and angles of the fragment surrounding the Dy^{III} ions in the two complexes are basically consistent, making the comparison for these system high informative (Table S6 for the estimated deviations for the idealized geometries).

Direct current (dc) magnetic susceptibility measurements indicate that there are overall ferromagnetic couplings within the molecule, which is very similar to what was found in compound **43**. Ac susceptibility measurements show that **45** is a typical SMM under zero dc field as evidenced by the observation of maxima of ac signals (Fig. 42a). A fit to the Arrhenius law gave U_{eff} = 88.8 K (61.6 cm^{-1}) and τ_0 = 2.29 × 10^{-6} s in the range 16–20 K. A fit employing multi-relaxation processes (Fig. 42b) gave τ_{QTM}^{-1} = 0.001 s^{-1}, C = 0.301 s^{-1} K$^{-3.16}$, n = 3.16, τ_0 = 2.67 × 10^{-6} s, and U_{eff} = 125.1 K (86.8 cm^{-1}) (Table 6). For complex **45**, no hysteresis loops were observed even at 1.8 K. Surprisingly, compound **42** with THF coordinating to the Co^{II} ions, shows large hysteresis loops below 4 K. The *ab initio* calculations for these two complexes reveal that it is the difference in the local environment of the Co^{II} ions which directly affects the uniaxial magnetic anisotropy of Co^{II} as well as the magnitude of the ferromagnetic interactions between the central Co^{II} ions as judged from J_{Co-Co} where
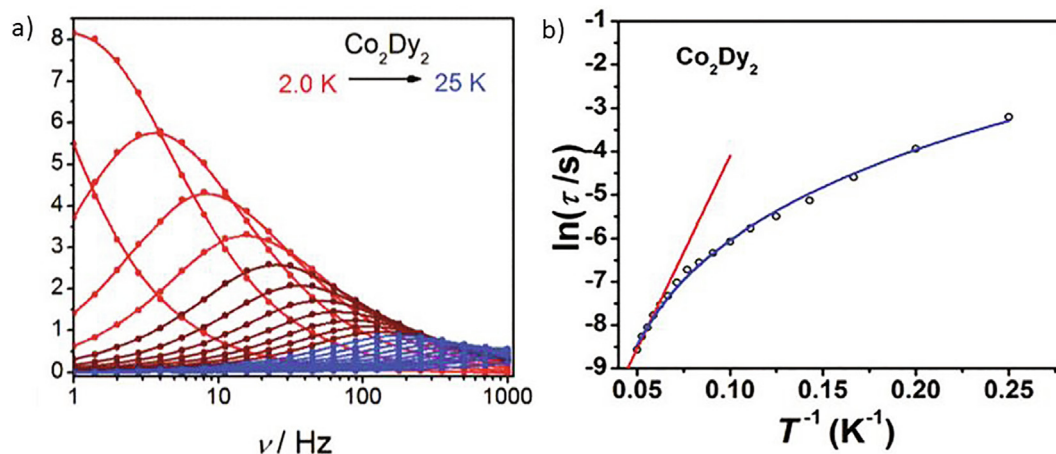
Fig. 42. Plots of χ'' vs ν (a) and plots of ln(τ) vs T^{-1} (b) for **45** [Co$_2^{II}$Dy$_2$(L2)$_4$(NO$_3$)$_2$(DMF)$_2$]·2DMF under zero dc field. Reprinted with permission from [45]. Copyright (2017) The Royal Society of Chemistry.

J_{Co-Co} = 6.8 cm^{-1} for **45** and J_{Co-Co} = 2.0 cm^{-1} for **42**, as well as the interaction between the Dy^{III} and Co^{II} ions J_{Dy-Co} where $_{Dy-Co}$ = 11.7 cm^{-1} for **45** and J_{Dy-Co} = 1.6 cm^{-1} for **42**. Both interactions are stronger for **45** and it thus seems that these stronger interactions effectively destroy the relaxation properties of the single ion Dy^{III}. In order to clarify the effects of the *3d-3d* and *3d-4f* magnetic interactions in these systems more examples are needed to allow for a systematic survey. These results further confirm that subtle changes in the ligand sphere can have a huge effect on the dynamic behavior, in line with the observations for compounds **41–43**. It is, however, difficult to compare the results of the *ab initio* calculation for **42** and **45** since for **42** the spin Hamiltonian was calculated using S = 3/2 for Co^{II} and S = 5/2 for Dy^{III}, whereas for **45** a pseudospin of S = 1/2 was used for the Co^{II} and Dy^{III} ions. As in the case for the {Mn$_2^{II}$Dy$_2$} **20** and {Zn$_2^{II}$Dy$_2$} **60** analogues the Dy^{III}-Dy^{III} interactions seem relatively large (Tables 4, 9). Within the SMM community *3d-3d* interactions are expected to be larger than *3d-4f* interactions which in turn are expected to be larger than *4f-4f* interactions.

Winpenny reported another butterfly, [^{i}Pr$_2$NH$_2$]$_2$[Co$_2^{II}$Dy$_2$(OH)$_2$ (Piv)$_{10}$] **46** (Fig. 43) [50]. It crystallizes in the triclinic space group *P-1* and is essentially isostructural to **28** [Et$_3$NH]$_2$ [Mn$_2^{III}$Dy$_2$(O)$_2$ (Piv)$_{10}$] with the small differences that in **46** the two μ$_3$-O^{2-} are two μ$_3$-OH$^-$ in **28** and the two Et$_3$NH$^+$ counterions are now two ^{i}Pr$_2$NH$_2^+$. The compounds show slow relaxation of magnetization but without maxima in χ″$_M$ vs T above 2 K. Thus no energy barrier could be obtained from the data (Fig. 44).
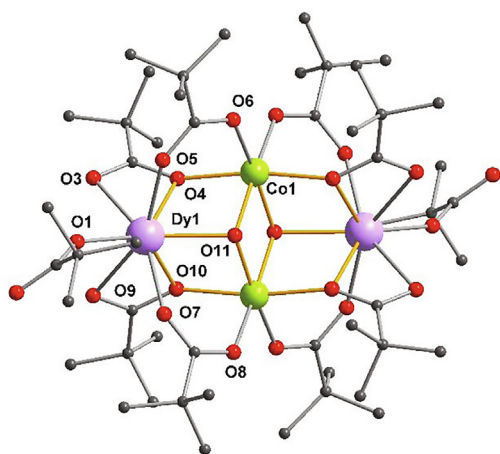
Fig. 43. Molecular structure of **46** [^{i}Pr$_2$NH$_2$]$_2$[Co$_2^{II}$Dy$_2$(OH)$_2$(Piv)$_{10}$].
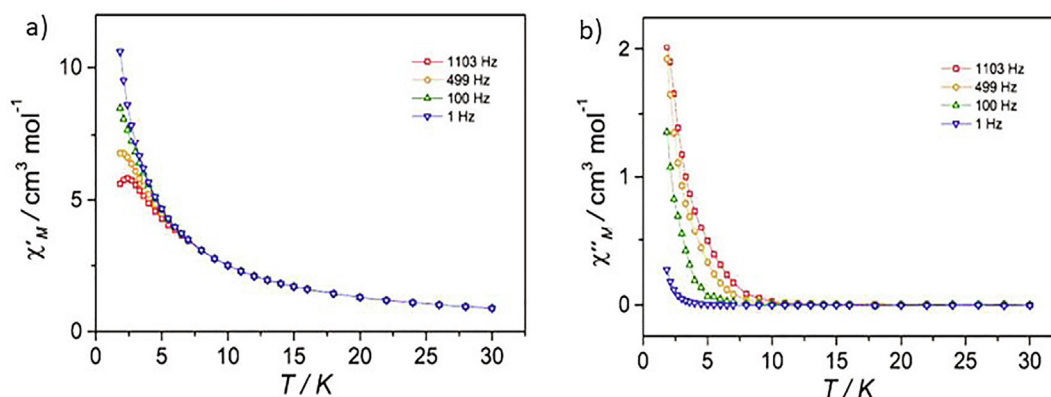
Summary: The *o*-vanillin based Schiff-base compounds incorporating Dy^{III} ions reveal two clear linear relaxation processes in the Arrhenius plots. In these systems, the effect of varying the coordinated solvent ligands proves to be a fine-tuning parameter for slow relaxation as discussed in more detail above.

3.1.5. {Ni$_2^{II}$Ln$_2$} systems

In 2011, Powell's group reported the first {Ni$_2^{II}$Ln$_2$} butterfly SMM systems, [Ni$_2^{II}$Dy$_2$(L1)$_4$(NO$_3$)$_2$(DMF)$_2$] **47** and [Ni$_2^{II}$Ln$_2$(L1)$_4$ (NO$_3$)$_2$(MeOH)$_2$]·3MeOH (Ln = Dy **48**, Tb **49**) H$_2$L1 = ((E)-2-(2-hydr oxy-3-methoxybenzyli-deneamino)phenol [61]. The only significant difference in the molecular structures involves the replacement of the ((E)-2-(2-hydroxy-3-methoxybenzyli-deneamino)phenol DMF ligand on each Ni^{II} ion in **47** by MeOH ligands in **48** and **49** (Fig. 45). The core of compound **47–48** can be described in terms of the well-known **Type I** butterfly topology and the compounds are isostructural to complexes **42–45**.

The dc susceptibilities indicate intramolecular ferromagnetic interactions between the paramagnetic centers within the {Ni$_2^{II}$Ln$_2$} units. Ac susceptibility measurements show typical SMM behavior for both Dy-containing complexes **47** and **48** under zero dc fields with U_{eff} = 18.5 K (12.9 cm^{-1}) and τ_0 = 5.4 × 10^{-7} s for **47**, U_{eff} = 21.3-K (14.8 cm^{-1}) and τ_0 = 1.5 × 10^{-6} s for **48** (Fig. 46) without QTM, since the ln(τ) vs T^{-1} are linear over the whole temperature region. Complex **49** {Ni$_2^{II}$Tb$_2$} shows field-induced SMM behavior with U_{eff} = 28.5 K (19.8 cm^{-1}) and τ_0 = 2.8 × 10^{-6} s (Table 7) under 4000 Oe dc field. Fits to Cole-Cole plots gave α values in the range 0.10 to 0.14 for **47** suggesting single relaxation processes. For **48**, a good fit could only be obtained above 3.4 K giving α values in range 0.09–0.16.

These results indicate that the ligand substitution on Ni^{II} has a significant effect on the magnetic properties, which is in line with the results on the {Co$_2^{II}$Dy$_2$} analogues discussed in Section 3.1.4. Furthermore, on replacing the Co^{II} with Ni^{II}, large changes in the magnetic signature are observed, suggesting the nature of the *3d* metal ions within a given motif is an important influence on the resulting magnetic properties. One factor to consider here is the significant differences between these two *3d* ions in octahedral coordination geometries. Co^{II} is expected to be a very anisotropic Kramers single ion, whereas Ni^{II} has much less anisotropy and is a non-Kramers single ion. Quite how these factors can influence the magnetic properties in such *3d-4f* butterflies is something requiring further examples and *ab initio* calculations (Table 4).

The results also reveal that the ligand substituents on the *3d* metal ions could change the coordination geometries of the lanthanides, which clearly has an effect on the orientation and pre-

Fig. 44. Plots of χ′ (a) and χ″ (b) vs T for **46** [^{i}Pr$_2$NH$_2$]$_2$[Co$_2^{II}$Dy$_2$(OH)$_2$(Piv)$_{10}$] under zero dc field. Reprinted with permission from [50]. Copyright (2015) American Chemical Society.
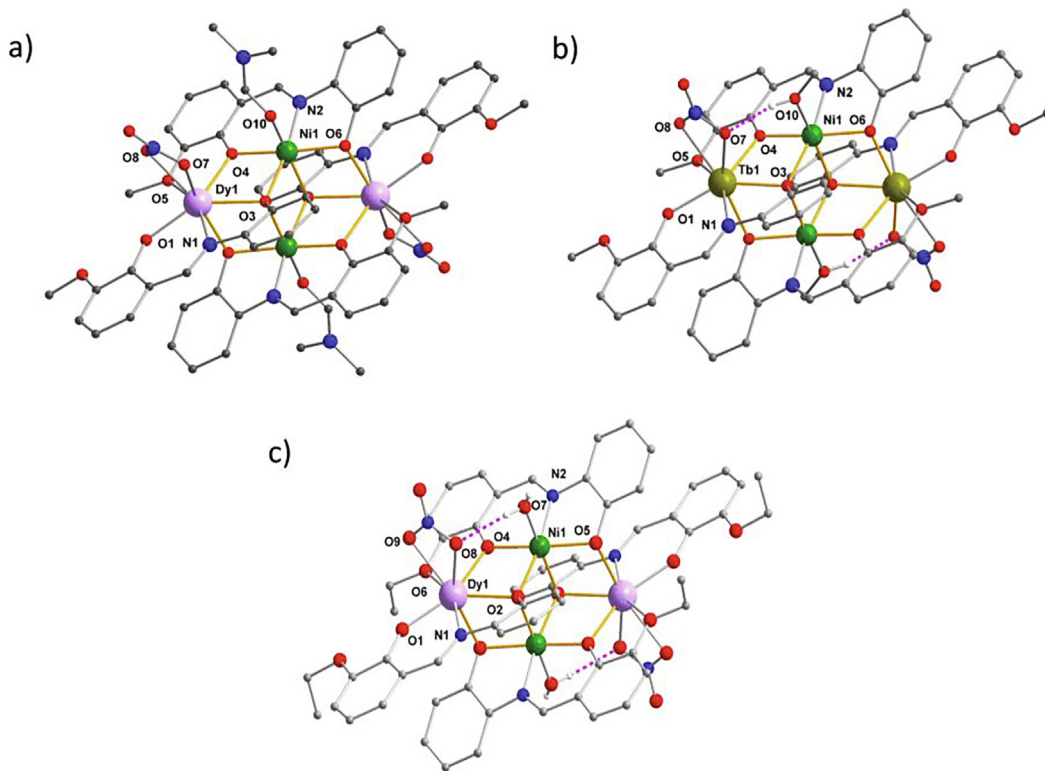
Fig. 45. Molecular structures of the coordination clusters in compounds **47** [Ni$_2^{II}$Dy$_2$(L1)$_4$(NO$_3$)$_2$(DMF)$_2$] (a) and **48** [Ni$_2^{II}$Dy$_2$(L1)$_4$(NO$_3$)$_2$(MeOH)$_2$]·3MeOH (b) **49** [Ni$_2^{II}$Tb$_2$(L2)$_2$(NO$_3$)$_2$(H$_2$O)$_2$] (c).
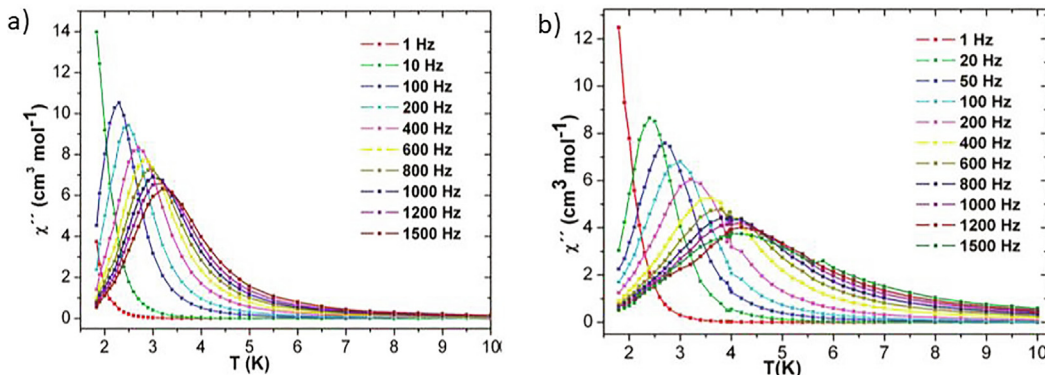
Fig. 46. Plots of χ″ vs T for **47** (a) and **48** (b) under zero dc field. Reprinted with permission from [61]. Copyright (2011) American Chemical Society.

sumably the magnitude of the lanthanide single-ion anisotropy tensors.

Changing the H$_2$L1 (((E)-2-(2-hydroxy-3-methoxybenzyli-dene amino)phenol) to H$_2$L2 (((E)-2-(2-hydroxy-3-ethoxybenzyli-denea mino)phenol), Christou and Mohanta could produce isostructural [Ni$_2^{II}$Ln$_2$(L2)$_2$(NO$_3$)$_2$(MeOH)$_2$] [62]. However, these molecules lose their two MeOH molecules which are replaced by two water molecules to give [Ni$_2^{II}$Ln$_2$(L2)$_2$(NO$_3$)$_2$(H$_2$O)$_2$] **50**. This molecule also shows ferromagnetic coupling within the metal centers for the Dy^{III} compound. Typical SMM behavior was observed with U_{eff} = 36.0 K (25 cm^{-1}) and τ_0 = 8 × 10^{-8} s (Fig. 47). This result further confirms that small differences in the structural parameters can induce significant differences in the magnetic properties of butterfly systems with similar core compositions (in terms of the metal ions) and topologies.

In 2015, three butterfly Ni^{II}-4f clusters of **Type I** were reported by Liang's group with formulae of [Ni$_2^{II}$Dy$_2$(H$_2$L4)$_2$(OMe)$_2$(CH$_3$CN)$_2$

(NO$_3$)$_4$]·4H$_2$O **51**, [Ni$_2^{II}$Ln$_2$ (HL5)$_2$(OMe)$_2$(CH$_3$CN)$_2$(NO$_3$)$_4$]·4H$_2$O (Ln = Tb **52**, Dy **53**) [63], using the o-vanillin based Schiff-base ligands 2-(((2-hydroxy-3-methoxyphenyl)methylene)amino)-2-(hydroxyme thyl)-1,3-propanediol (H$_4$L4) (Scheme S1) and 2-(2,3-dihydroxypropyli minomethyl)-6-methoxyphenol (H$_3$L5). Compound **51** crystallizes in the space group P-1 whereas complexes **52** and **53** are isostructural crystallizing in the space group P2$_1$/n (Fig. 48). Both systems lie on crystallographic inversion centers to give a **Type I** [Ni$_2^{II}$Dy$_2$] butterfly core bridged by two μ$_3$-OMe. The butterfly cores of **51** and **53** are bridged and chelated by two doubly deprotonated HL4 with η^1:η^2: η^1:η^2:η^1:η^0: μ$_3$ coordination mode for **51** or two doubly deproto-nated HL5 with η^1:η^2:η^1:η^2:η^1: μ$_3$ coordination mode for **53**. Two MeCN molecules coordinate to two Ni^{II} ions to complete six-coordinated distorted octahedral coordination geometry (Table S7 for the estimated deviations for the idealized geometries). Each Dy^{III} ion further coordinated by two chelating NO$_3^-$ to complete the nine-coordinate distorted capped square antiprismatic geometry.
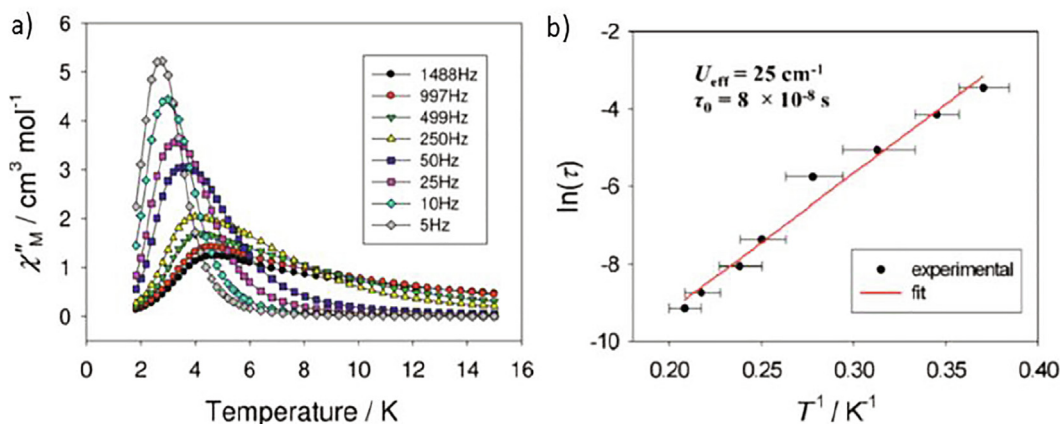
Fig. 47. Plots of χ'' vs T (a) and plot of $\ln(\tau)$ vs T^{-1} (b) for **50** [Ni$_2^{II}$Dy$_2$L$_4$(NO$_3$)$_2$(H$_2$O)$_2$]·2H$_2$O under zero dc field. Reprinted with permission from [62]. Copyright (2018) Wiley-VCH Verlag GmbH& Co. KGaA.
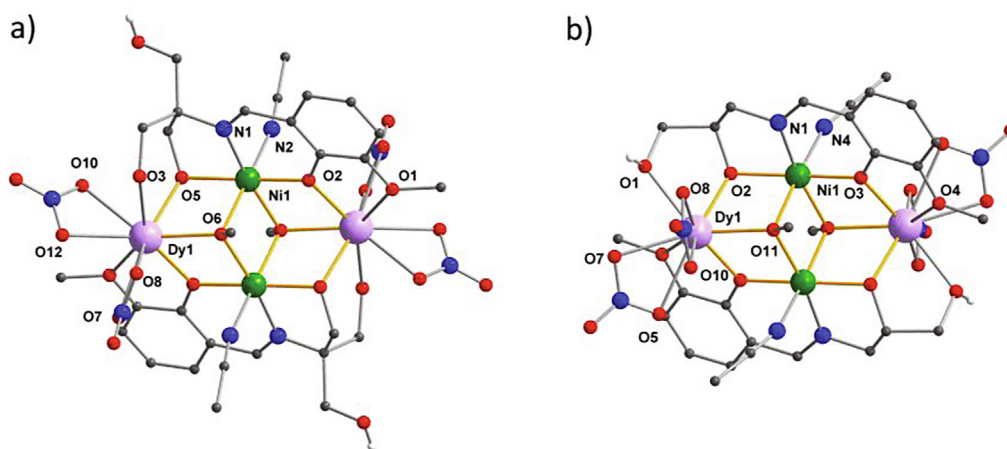
Fig. 48. Molecular structures of compounds **51** [Ni$_2^{II}$Dy$_2$(H$_2$L4)$_2$(OMe)$_2$(CH$_3$CN)$_2$(NO$_3$)$_4$]·4H$_2$O (a) and **53** [Ni$_2$Dy$_2$ (HL5)$_2$(OMe)$_2$(CH$_3$CN)$_2$(NO$_3$)$_4$]·4H$_2$O (b).
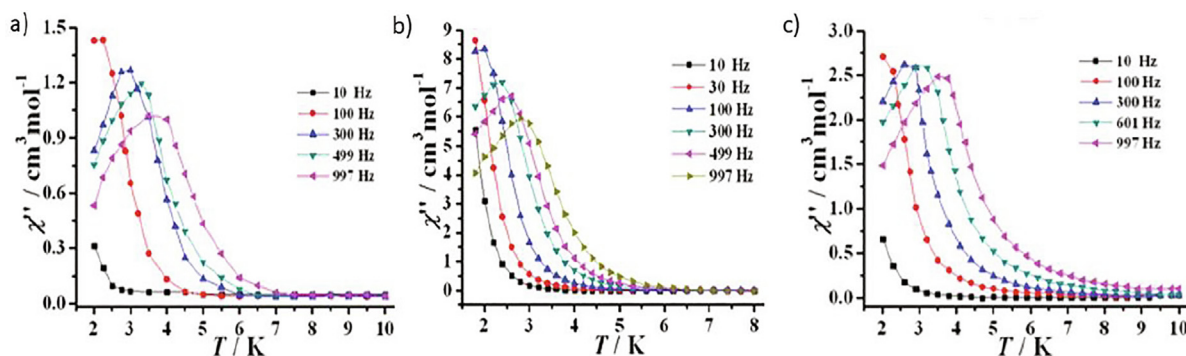
Fig. 49. Plots of χ'' vs T for **51** [Ni$_2^{II}$Dy$_2$(H$_2$L4)$_2$(OMe)$_2$(CH$_3$CN)$_2$(NO$_3$)$_4$]·4H$_2$O (a), [Ni$_2^{II}$Ln$_2$ (HL5)$_2$(OMe)$_2$(CH$_3$CN)$_2$(NO$_3$)$_4$]·4H$_2$O Ln = Tb **52** (b), and Ln = Dy **53** (c) under zero dc field. Reprinted with permission from [63].Copyright (2015) The Royal Society of Chemistry.

Magnetic measurements show similar behavior in χT with decreasing temperature for compounds **51–53**, consistent with overall antiferromagnetic interactions between metal ions. Ac susceptibility measurements indicate compounds **51–53** are all SMMs under zero dc field (Fig. 49) with energy barriers of 48.46 K (33.7 cm^{-1}), 86.71 K (60.3 cm^{-1}) and 56.94 K (39.6 cm^{-1}) and relaxation times τ_0 = 3.6 × 10^{-8}, 2.3 × 10^{-7} and 3.3 × 10^{-8} s, respectively, indicating that complexes **51–53** display relatively high anisotropy barriers. In particular, **52** {Ni$_2$Tb$_2$} not only has the best SMM parameters among these three compounds, but also

exhibits the highest anisotropy barrier among the Ni^{II}-Tb^{III} based SMMs reported so far. *Ab initio* calculations suggest there are stronger *3d-4f* exchange couplings within these compounds, which again highlights the importance of the exchange coupling in *3d-4f* SMMs. The *ab initio* calculations on these {Ni$_2^{II}$Ln$_2$} were performed by the same group who analyzed the compounds {Mn$_2^{II}$Dy$_2$} **20**, {Co$_2^{II}$Dy$_2$} **45** and {Zn$_2^{II}$Dy$_2$} **60**. As mentioned previously, the relative values of the *3d-3d* and *3d-4f* coupling seem counter intuitive when the BS-DFT approach is used for compound **51** with J_{3d-3d} = 7.9 cm^{-1} and J_{3d-4f} = 17.2 cm^{-1} (Tables 4 and 9).
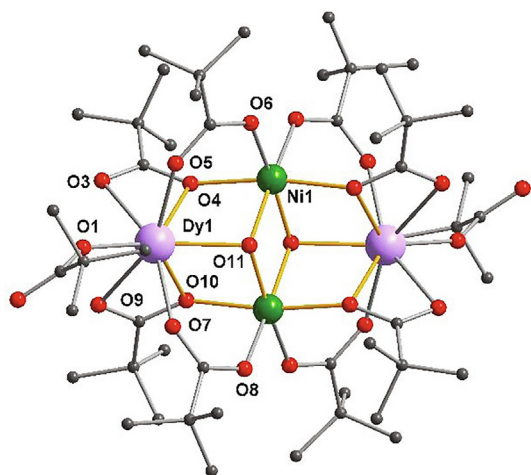
Fig. 50. Molecular structure of compound **54** [Et$_3$NH]$_2$[Ni$_2^{II}$Dy$_2$(OH)$_2$(Piv)$_{10}$]

In the same year, another family of {Ni$_2^{II}$Ln$_2$} butterfly coordination clusters, [Et$_3$NH]$_2$[Ni$_2^{II}$Ln$_2$(OH)$_2$(Piv)$_{10}$] (Ln = Dy **54** and Er **55**) [50], were reported by Winpenny's group. The structures are isostructural to the reported compound **46** [^{i}Pr$_2$NH$_2$]$_2$[Co$_2^{II}$Ln$_2$(OH)$_2$ (Piv)$_{10}$] (Fig. 50).

Ac susceptibility measurements indicate that the {Ni$_2^{II}$Dy$_2$} compound shows slow relaxation under zero field and clear maxima are observed in the temperature- and frequency-dependent measurements (Fig. 51) at low temperature. Analysis of χ (T, ν) gives U_{eff} = 20-K (13.9 cm^{-1}) and τ_0 = 6.0 × 10^{-7} s, with α varying from 0.01 to 0.1 from high to low temperature. {Ni$_2^{II}$Er$_2$} shows similar magnetic behavior to {Ni$_2^{II}$Dy$_2$} when measured under a 1000 Oe dc field. Arrhenius analysis gives U_{eff} = 12 K (8.3 cm^{-1}) with τ_0 = 5 × 10^{-6}

s and α = 0.1 at high temperature, increasing to 0.2 at lower temperatures, which indicates a narrow distribution of the relaxation (Fig. 52). As was the case for Mn^{III} analogue discussed before, the data of {Ni$_2^{II}$Dy$_2$} clearly show that other relaxation processes are in operation. From the shape of ln(τ) vs T^{-1} plots, it is probably only a Raman process which dominates for {Ni$_2$Er$_2$}.

Summary: All {Ni$_2^{II}$Dy$_2$} analogues in {Ni$_2^{II}$Ln$_2$} systems, show typical SMM properties under zero applied dc fields. Interestingly, in the [Ni$_2^{II}$Ln$_2$(HL5)$_2$(OMe)$_2$(CH$_3$CN)$_2$(NO$_3$)$_4$]·4H$_2$O system, the Tb^{III} analogue shows better SMM properties than the Dy^{III} analogue, which is unusual for *3d-4f* systems. We note that for the {Co$_2^{II}$Ln$_2$} analogues, the Dy^{III} analogues have better SMM parameters suggesting that mixing *3d* Kramer ions with *4f* Kramer ions is favorable as is, apparently, mixing *3d* non-Kramer ions with *4f* non-Kramer ions. This obviously requires further exploration in order to discover means to help target better performing 3d-4f SMMs.

3.1.6. {Cu$_2^{II}$Ln$_2$} systems

Winpenny's group reported the first {Cu$_2^{II}$Ln$_2$} (Ln = Dy **56** or Er **57**) butterfly SMMs [50], [^{i}Pr$_2$NH$_2$]$_2$[Cu$_2^{II}$Ln$_2$(OH)$_2$(Piv)$_{10}$]. The structures are isostructural to the reported [^{i}Pr$_2$NH$_2$]$_2$[Co$_2^{II}$Ln$_2$(OH)$_2$ (Piv)$_{10}$] **46** compound (Fig. 53).

Dc susceptibility measurements indicate both compounds show overall antiferromagnetic coupling between the metal centers. Ac susceptibility measurements reveal both compounds show slow relaxation without maxima even under applied dc field, making it impossible to derive an energy barrier (Fig. 54).

In 2017, the Powell group reported another {Cu$_2^{II}$Dy$_2$} **Type I** butterfly SMM [64], [Cu$_2^{II}$Dy$_2$(OMe)$_2$(HL6)$_2$(NO$_3$)$_4$]·2MeOH **58** (Fig. 55a) which is similar to the [Ni$_2^{II}$Dy$_2$(H$_2$L4)$_2$(OMe)$_2$(CH$_3$CN)$_2$(NO$_3$)$_4$]· 4H$_2$O **51** and [Ni$_2^{II}$Ln$_2$ (HL5)$_2$(OMe)$_2$(CH$_3$CN)$_2$(NO$_3$)$_4$]·4H$_2$O (Ln = Tb **52** or Dy **53**) compounds. The butterfly core is bridged and chelated by two doubly deprotonated H$_3$L5 with η^1:η^2:η^1:η^2:η^1:η^0: μ_3

Fig. 51. (a) Plots of χ'' vs T; (b) plots of χ'' vs ν; (c) Cole-Cole plots; (d) plots of ln(τ) vs T^{-1} for **54** {Ni$_2^{II}$Dy$_2$} under zero dc field. Reprinted with permission from [50]. Copyright (2015) American Chemical Society.
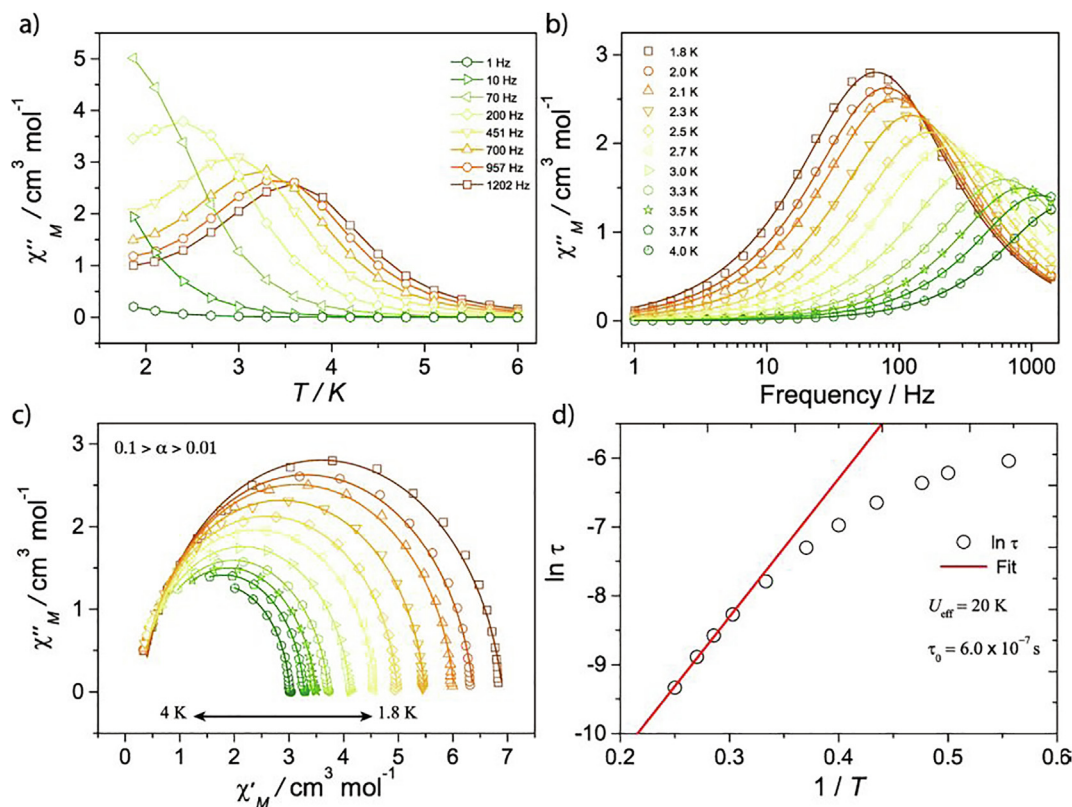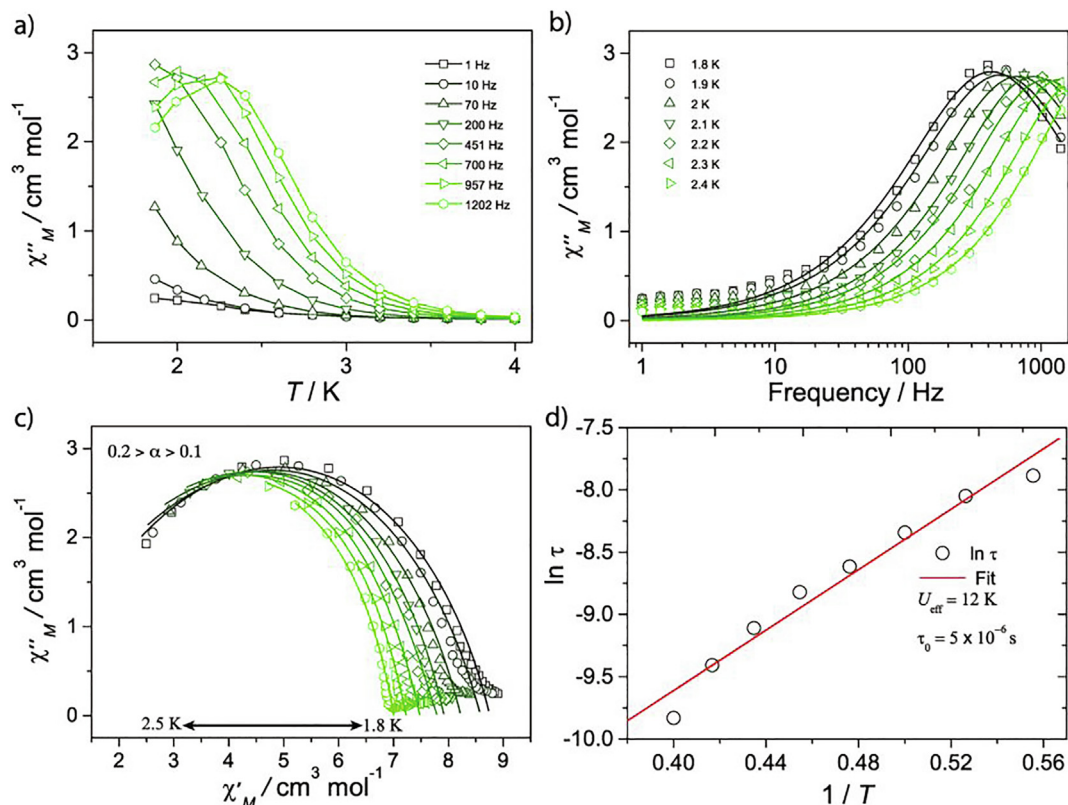
Fig. 52. (a) Plots of χ'' vs T; (b) plots of χ'' vs ν; (c) Cole-Cole plots; (d) plots of $\ln(\tau)$ vs T^{-1} for **55** {Ni$_2^{II}$Er$_2$} under zero dc field. Reprinted with permission from [50]. Copyright (2015) American Chemical Society.
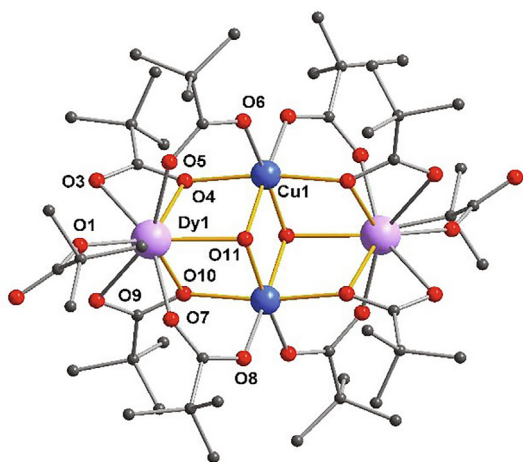
Fig. 53. Molecular structure of compound **56** [^{i}Pr$_2$NH$_2$]$_2$[Cu$_2^{II}$Ln$_2$(OH)$_2$(Piv)$_{10}$].

coordination mode. The two Cu^{II} ions have five-coordinate distorted square pyramid coordination geometry. Two pairs of NO$_3^-$ ions coordinate to two Dy^{III} ions to complete nine-coordinate distorted capped square anti-prismatic coordination geometries (Table S7 for the estimated deviations for the idealized geometries). The ac measurements reveal that the compound show maxima only under applied dc field of 1500 Oe with U_{eff} = 16.5 K (11.5 cm^{-1}) and τ_0 = 4.5 × 10^{-7} s (Fig. 55b and Table 8).

Summary: Generally speaking, it might appear that Cu^{II} with its single unpaired electron is not the best choice for *3d-4f* SMMs. The fact that all the butterfly examples require application of dc field to reveal slow relaxation supports this view.

3.2. 3d (diamagnetic)/4f systems

In several of the *3d-4f* butterfly SMMs coordination clusters, the *3d* metal ions are diamagnetic Zn^{II} and Co^{III} ions. Thus it is debatable whether these coordination clusters should be considered *3d-4f* SMMs or simply lanthanide SMMs. We have decided to consider these species here since usually when lanthanide SMMs are reviewed such compounds are not accounted for [65–68]. Furthermore, these can give insights into the effect of the diamagnetic ions on the dynamic behavior of the paramagnetic *4f* ions. Although the *3d* diamagnetic metal ions Zn^{II} and Co^{III} have been successfully used as "knock-out" ions for replacement of divalent *3d* ions such as Mn^{II}, Co^{II}, Ni^{II}, Cu^{II} and trivalent *3d* ions such as Cr^{III}, Mn^{III}, Fe^{III}, until now, little progress has been made in replacing M^{II} with Mg^{II} and M^{III} with Al^{III}, both being non-*3d* alternatives. There are only two such butterfly systems, {Mg$_2^{II}$Ln$_2$} and {Al$_2^{III}$Ln$_2$} in the literature and these will also be discussed here.

3.2.1. {Zn$_2^{II}$Ln$_2$} systems

{Zn$_2^{II}$Ln$_2$} complexes are normally isolated as analogues to help the study of other {M$_2^{II}$Ln$_2$} (M = Co, Mn, Ni and Cu) isostructural clusters. The groups of Powell, Song and Ke reported three similar {Zn$_2^{II}$Ln$_2$} butterfly SMMs compounds, [Zn$_2^{II}$Dy$_2$(L1)$_4$(NO$_3$)$_2$(MeOH)$_2$]·2CH$_2$Cl$_2$ **59** [Zn$_2^{II}$Dy$_2$(L2)$_4$(NO$_3$)$_2$(MeOH)$_2$] **60** and [Zn$_2^{II}$Dy$_2$(L3)$_4$(NO$_3$)$_2$(MeOH)$_2$]·2C$_3$H$_6$O **61** with *o*-vanillin based Schiff-base ligands [45,60,69]. The slight differences in the organic ligands and lattice solvents (Fig. 56) allow for comparison/assessment of the effect of the remote organic functional groups on the magnetic properties. Dc magnetic susceptibility measurements indicate there are weak ferromagnetic dipolar interactions between these two distant Dy^{III} ions within these three complexes. Ac measurements reveal they show typical SMM behavior under zero dc field (Fig. 57). The relax-
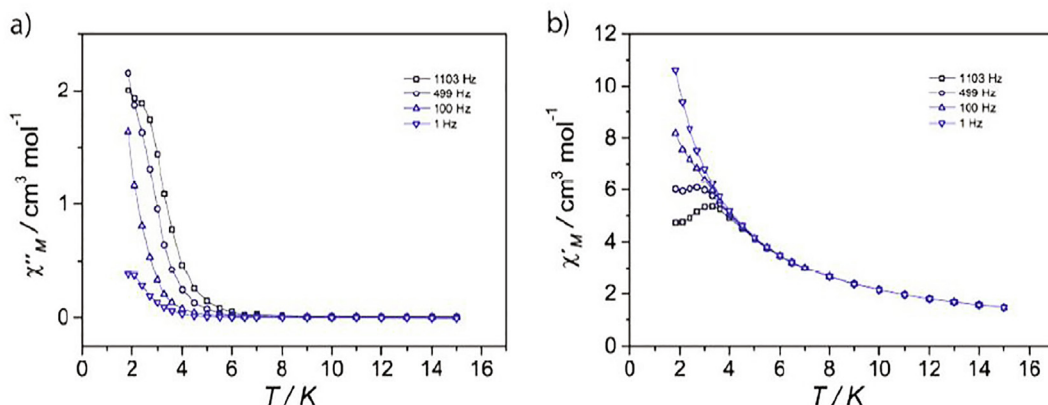
Fig. 54. plots of χ' (a) and χ'' (b) vs T for **56**, [^{i}Pr$_2$NH$_2$]$_2$[Cu$_2^{II}$Ln$_2$(OH)$_2$(Piv)$_{10}$] under zero dc field. Reprinted with permission from [50]. Copyright (2015) American Chemical Society.
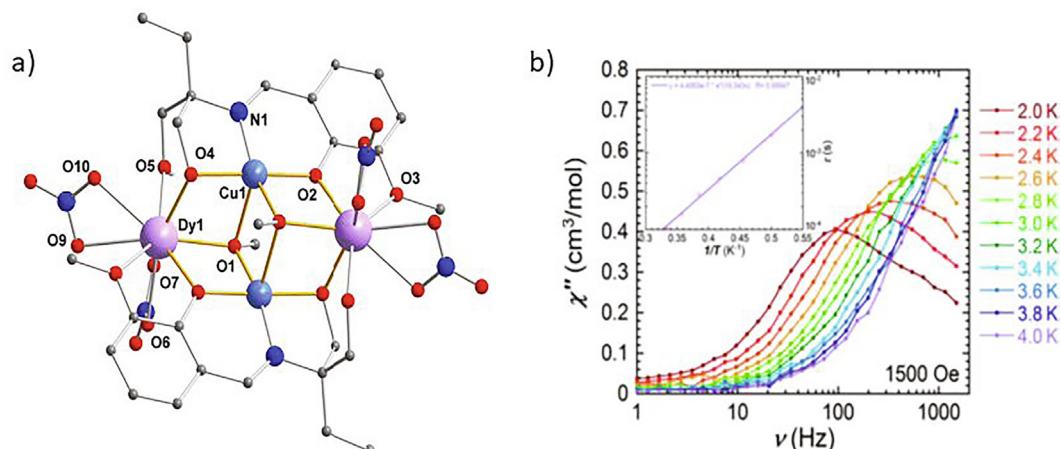
Fig. 55. Molecular structure (a) and plots of χ'' vs ν (b) for **58** [Cu$_2^{II}$Dy$_2$(OMe)$_2$(HL6)$_2$(NO$_3$)$_4$]·2MeOH. Arrhenius fit (right inset). Reprinted with permission from [64]. Copyright (2017) American Chemical Society.

ation data can be modelled allowing for QTM, Raman and Orbach relaxation processes for compounds **59** and **60** with parameters of U_{eff} = 140.4 K (97.6 cm^{-1}), τ_0 = 1.4 × 10^{-7} s, n = 4.1, C = 2.1 × 10^{-2} s^{-1} K$^{-4.1}$ and τ_{QTM} = 1.50 × 10^{-2} s for **59** and U_{eff} = 115 K (79.9 cm^{-1}), τ_0 = 2.35 × 10^{-6} s, n = 3.26 and C = 0.116 s^{-1} K$^{-3.26}$, τ_{QTM} = 9.2 × 10^{-3} s for **60**. The QTM process turns out to be a significant feature of many of these Type **I** butterfly compounds with diamagnetic 3d-contributions. This short-cut to overcoming the energy barrier places an important limit on what might be regarded as "well-performing" SMM properties. Put simply, a high energy barrier to spin reversal is no guarantee that the system is forced to overcome this barrier (as seen here). Indeed, as is widely acknowledged, in order to utilize the potential of the very high energy barriers to magnetization reversal which 4f ions can deliver, it is necessary to maintain a careful control over the local coordination geometry of the lanthanide ion in question. In addition, little attention has so far been paid to the role of spin-phonon relaxation modes operating in solid state systems. These effects are possibly easier to control by using the ameliorating effects of providing a nearby 3d partner, which, through even weak coupling to 4f ions seems to be an ideal way to push the system over what may well be a lower energy barrier, but in end effect avoid relaxation processes short-circuiting the "trip to the summit".

For **61**, the whole temperature range could be fitted using only a combination of Orbach and Raman processes with parameters

U_{eff} = 112.2 K (78 cm^{-1}), τ_0 = 8.2 × 10^{-5} s, n = 5.4 and C = 1.47 × 10^{-4} s^{-1} K$^{-5.4}$ (Table 8). These results show that remote functional groups on the organic ligands in {Zn$_2^{II}$Dy$_2$} complexes can modulate the dynamic behavior that the diamagnetic 3d body ions can help to suppress zero field QTM of the individual wingtip Dy^{III} ions.

Through careful control of the reaction conditions, [Zn$_2^{II}$Dy$_2$(L3)$_4$(OAc)$_2$(EtOH)$_2$]·4C$_3$H$_6$O **62**[69] [Zn$_2^{II}$Dy$_2$(L3)$_4$(OAc)$_2$(EtOH)$_2$]·2CH$_2$Cl$_2$·0.5H$_2$O **63** and [Zn$_2^{II}$Dy$_2$(L3)$_4$(OAc)$_2$(MeOH)$_2$]·4CH$_2$Cl$_2$·2MeOH·0.1H$_2$O **64** could be obtained (Fig. 58) [70]. Compounds **62** and **63** are isostructural with only slight differences in terms of the lattice solvent molecules. The relaxation dynamics can be fit with a combination of QTM and Orbach processes with parameters U_{eff} = 74.8 K (52 cm^{-1}), τ_0 = 2.78 × 10^{-6} s, and τ_{QTM} = 2.5 × 10^{-4} s for **62**, for **63** a Raman process was also identified giving parameters of U_{eff} = 166.0 K (115.4 cm^{-1}), τ_0 = 6.6 × 10^{-9} s, n = 2.02 and C = 16.75 s^{-1} K$^{-2.02}$ (Table 8). When the data are modeled using the multiple relaxation equation, it is interesting that the higher energy barrier for **63** is accompanied by a faster τ_0 parameter indicating that the relevance of the lattice phonon modes has been significantly altered. These two systems provide useful models for future in-depth studies on the role of lattice spin phonon relaxation process which could be evaluated using heat capacity plus ^{161}Dy NRVS (nuclear resonance vibrational spectroscopy). The results also show that the nature and probably connectivity of lattice solvent molecules can have a significant effect on the dynamic magnetic
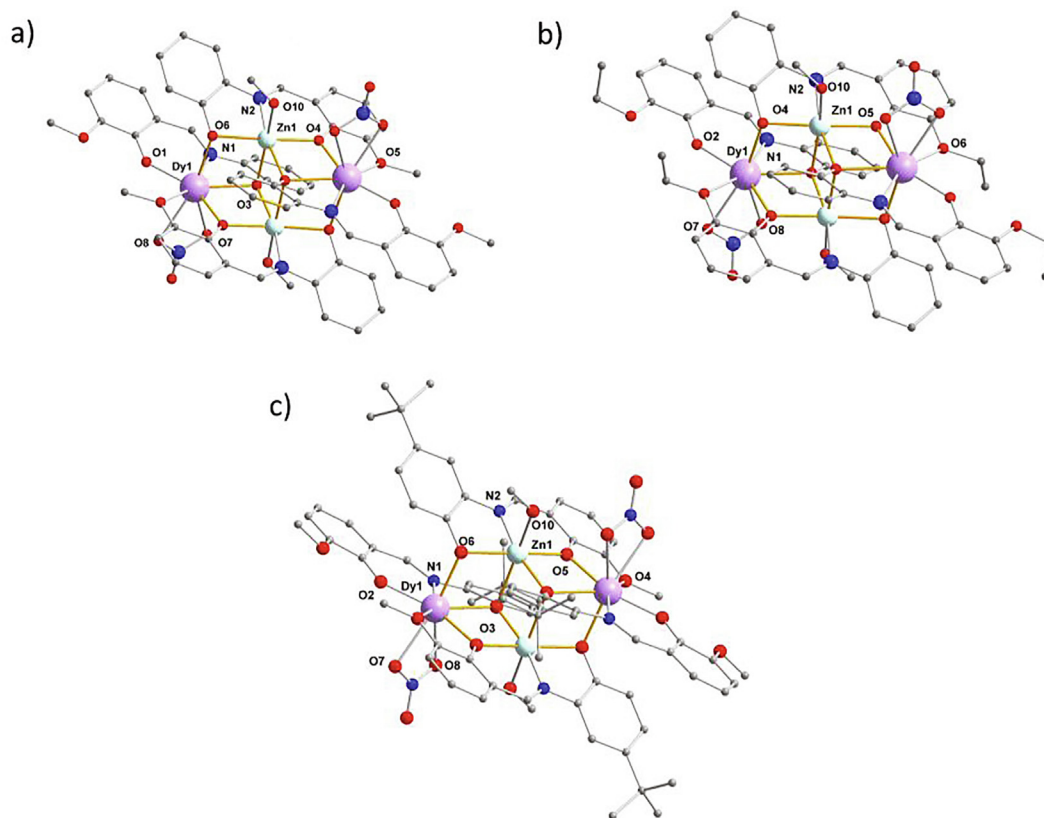
Fig. 56. Molecular structures of **59** [Zn$_2^{II}$Dy$_2$(L1)$_4$(NO$_3$)$_2$(MeOH)$_2$]·2CH$_2$Cl$_2$ (a), **60** [Zn$_2^{II}$Dy$_2$(L2)$_4$(NO$_3$)$_2$(MeOH)$_2$] (b) and **61** [Zn$_2$Dy$_2$(L3)$_4$(NO$_3$)$_2$(MeOH)$_2$]·2C$_3$H$_6$O (c).
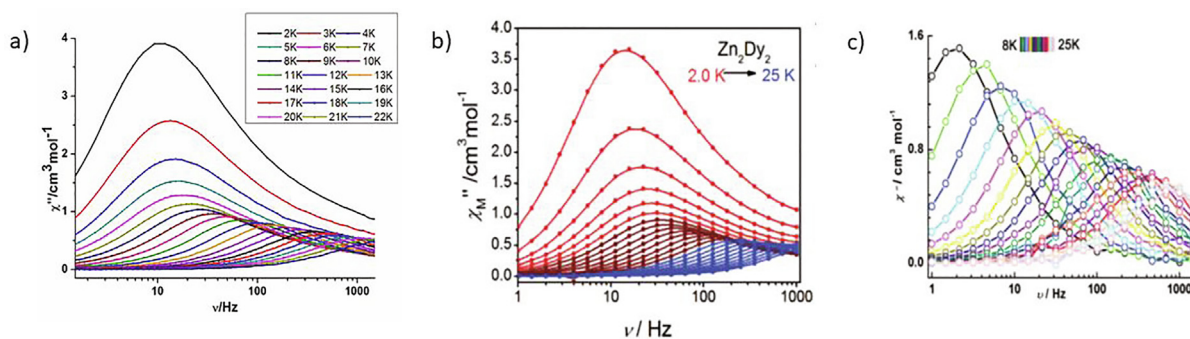
Fig. 57. Plots of χ″ vs ν for compounds **59** [Zn$_2^{II}$Dy$_2$(HL1)$_4$(NO$_3$)$_2$(MeOH)$_2$]·2CH$_2$Cl$_2$ (a), Reprinted with permission from [60] Copyright (2017) The Royal Society of Chemistry. **60** [Zn$_2^{II}$Dy$_2$(HL2)$_4$(NO$_3$)$_2$(MeOH)$_2$] (b) Reprinted with permission from [45]. Copyright (2017) The Royal Society of Chemistry. and **61** [Zn$_2$Dy$_2$(L3)$_4$(NO$_3$)$_2$(MeOH)$_2$]·2CH$_3$COCH$_3$ (c). Reprinted with permission from [69]. Copyright (2019) The Royal Society of Chemistry.

properties (Fig. 59) which is likely to be the result of the different nature of spin/lattice relaxation modes mediated by spin-phonon coupling.

Complex **64** is similar to complexes **62** and **63**, but with each of the two acetate ions now bridging the Zn^{II} and Dy^{III} ions instead of solely chelating the Dy^{III} ions. The two terminal solvent ligands on the Zn^{II} ions in **62** and **63** are transferred to the Dy^{III} ions in **64**, preserving the local coordination geometries of the Zn^{II} and Dy^{III} ions. With these differences, compound **64** shows ferromagnetic exchange coupling between two Dy^{III} ions at low temperature with J_{Dy-Dy}^{ex} = +0.25 cm^{-1}, which is opposite to the observation in complexes **62** and **63**. The relaxation dynamics can be fitted with a combination of QTM and Orbach processes with the parameters U_{eff} = 149.9 K (104.2 cm^{-1}), τ_0 = 1.26 × 10^{-7} s, n = 5.67, C = 3.26 × 10^{-4} s^{-1} K$^{-5.67}$ and τ_{QTM} = 2.02 s (Table 8).

Summary: For this system, the Dy^{III} ions are highly sensitive to the ligand field. Both main ligands and co-ligands have a significant effect on magnetic properties. Also, the lattice solvents influence the magnetic properties. For example, by changing the four lattice acetones per formula unit to two CH$_2$Cl$_2$ and 0.5 H$_2$O in [Zn$_2^{II}$Dy$_2$ (L3)$_4$(OAc)$_2$(EtOH)$_2$] the energy barrier changes from 74.8 K (**62**) to 166.0 K (**63**). Although it is impossible to draw any conclusion in this system, it is helpful to compare the magnetic properties with those of some paramagnetic 3d^{II} analogues {M$_2^{II}$Ln$_2$} (M = Co, Mn, Ni and Cu). The magnetic properties of [M$_2^{II}$Dy$_2$(L1)$_4$(NO$_3$)$_2$(MeOH)$_2$] M = Co **43** or Ni **48** or Zn **59**, [M$_2^{II}$Ln$_2$(L2)$_4$(NO$_3$)$_2$(DMF)$_2$] M = Co **45**, Zn **60** and [Ni$_2^{II}$Ln$_2$(L2)$_4$(NO$_3$)$_2$(H$_2$O)$_2$] **50** indicate that the paramagnetic 3d^{II} (Co and Ni) ions in these two systems help to suppress the ZF-QTM. However, changing the 3d^{II} ions to Mn^{II} ions, [Mn$_2^{II}$Dy$_2$ (L2)$_4$(NO$_3$)$_2$(DMF)$_2$] **20**, in this [M$_2^{II}$Dy$_2$(L2)$_4$(NO$_3$)$_2$(DMF)$_2$] (M = Co,
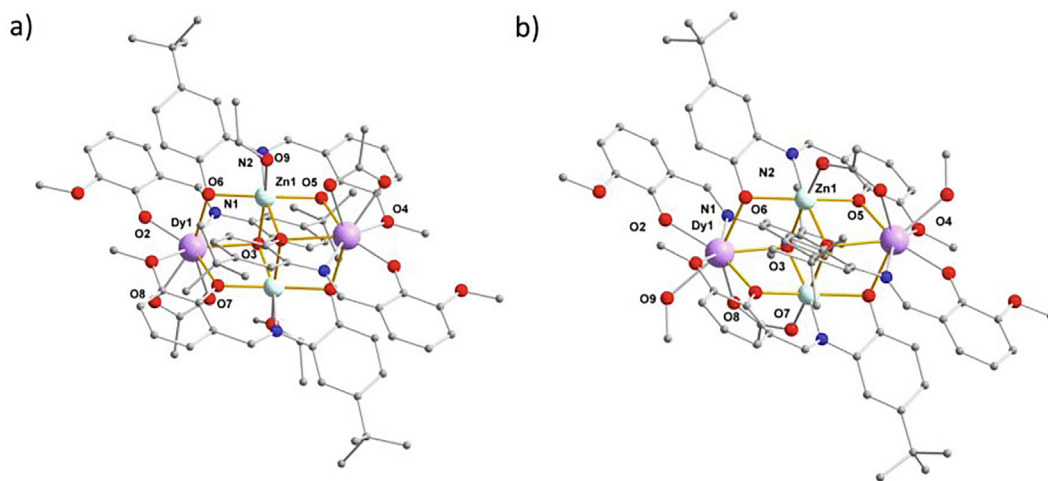
Fig. 58. Molecular structures of **62** [Zn$_2^{II}$Dy$_2$(L3)$_4$(OAc)$_2$(EtOH)$_2$]·4C$_3$H$_6$O (a), **63** [Zn$_2^{II}$Dy$_2$(L3)$_4$(OAc)$_2$(EtOH)$_2$]·2CH$_2$Cl$_2$·0.5H$_2$O (b) and **64** [Zn$_2^{II}$Dy$_2$(L3)$_4$(OAc)$_2$(MeOH)$_2$]·4CH$_2$Cl$_2$-·2MeOH·0.1H$_2$O (c).
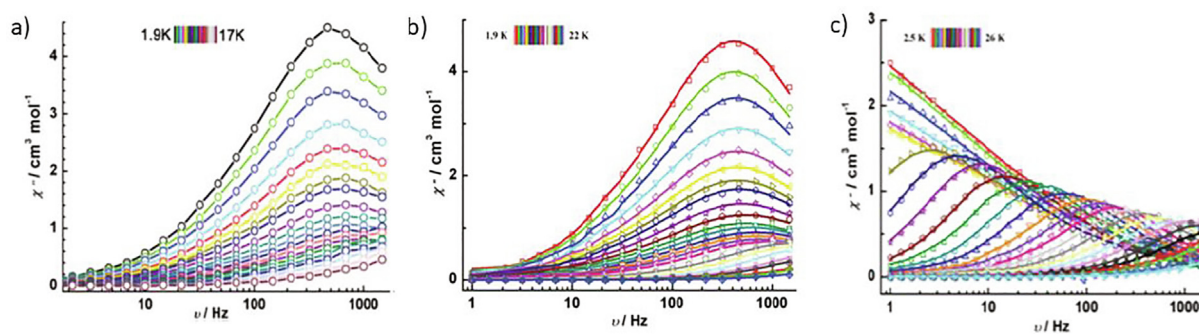
Fig. 59. Plots of χ'' vs ν for **62** [Zn$_2^{II}$Dy$_2$(L3)$_4$(OAc)$_2$(EtOH)$_2$]·4C$_3$H$_6$O (a), **63** [Zn$_2^{II}$Dy$_2$(L3)$_4$(OAc)$_2$(EtOH)$_2$]·2CH$_2$Cl$_2$·0.5H$_2$O (b) and **64** [Zn$_2^{II}$Dy$_2$(L3)$_4$(OAc)$_2$(MeOH)$_2$]·4CH$_2$Cl$_2$-·2MeOH·0.1H$_2$O (c) under zero dc field. Reprinted with permission from [69,70]. Copyright (2018, 2019) The Royal Society of Chemistry.
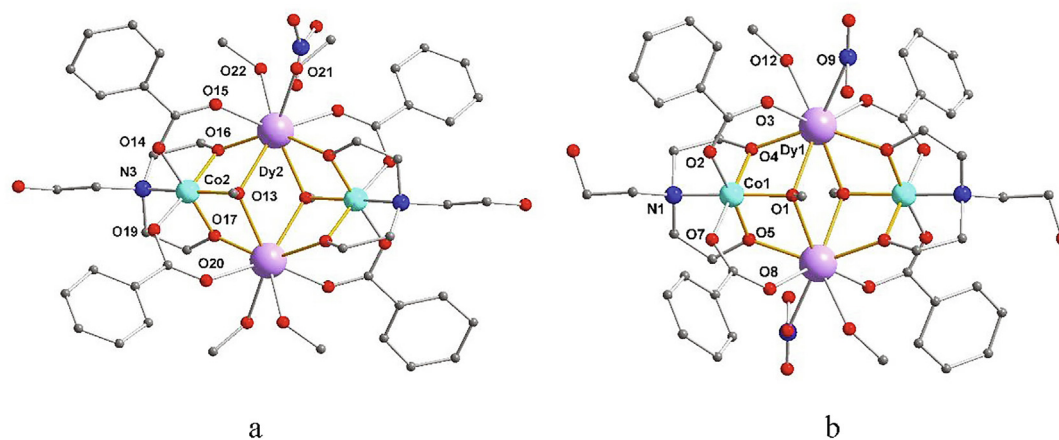
Fig. 60. Molecular structure of **66** [Co$_2^{III}$Ln$_2$(OMe)$_2$(teaH)$_2$(O$_2$CPh)$_4$(MeOH)$_4$](NO$_3$)$_2$·MeOH·H$_2$O a plus [Co$_2^{III}$Ln$_2$(OMe)$_2$(teaH)$_2$(O$_2$CPh)$_4$(MeOH)$_2$(NO$_3$)$_2$]·MeOH·H$_2$O b, where two **Type II** butterflies crystalized in one unit cell a and b for Ln = Dy and Tb.

Mn, Ni and Zn) family leads to disappearance of the SMM behavior, which indicates that we must combine the right *3d* ions with Dy^{III} ions to target SMMs within a given core motif. As seen in Table 9, *ab initio* calculations were performed for compounds **60–64**, the compound **60** has a J_{Dy-Dy}^{tot} = 2.8 cm^{-1}, whereas for compounds **61–64** these are in range 0.35–0.48 cm^{-1}. We do not expect the distant Dy^{III} ions to have such a big interaction. Furthermore, for compounds **61–64** all calculated by the same group, they introduced an inter-molecular interaction of 0.01 cm^{-1} (Table 9) for compound **63**, which is not consistent with the other three. Thus, it is impossible to relate the interactions to energy barriers, relaxation times and processes and thus derive magneto-structural correlations.

3.2.2. {Co$_2^{III}$Ln$_2$} systems

Murray's group was the first to report Co^{III}-4f butterfly SMMs in 2012 [71], namely [Co$_2^{III}$Ln$_2$(OMe)$_2$(teaH)$_2$(O$_2$CPh)$_4$(MeOH)$_4$](NO$_3$)$_2$·MeOH·H$_2$O (a) and [Co$_2^{III}$Ln$_2$(OMe)$_2$(teaH)$_2$(O$_2$CPh)$_4$(MeOH)$_2$(NO$_3$)$_2$]·MeOH·H$_2$O (b), ((Ln = Tb **65** or Dy **66**), which have the **Type II** core (Fig. 60). Here the Co^{III} ions are d^6 and diamagnetic. These com-

pounds are prepared from reaction of Co(NO$_3$)$_3$·6H$_2$O, Ln(NO$_3$)$_3$·nH$_2$O, teaH$_3$ (triethanolamine) and Et$_3$N in MeCN/MeOH. Compounds **65** and **66** are isostructural, crystallizing in the tetragonal space group *I4$_1$/a*. The asymmetric unit contains two half butterflies, designated as a and b for the complete butterflies. Butterflies a and b are structurally very similar. Butterfly a is found to be isostructural to **2**,
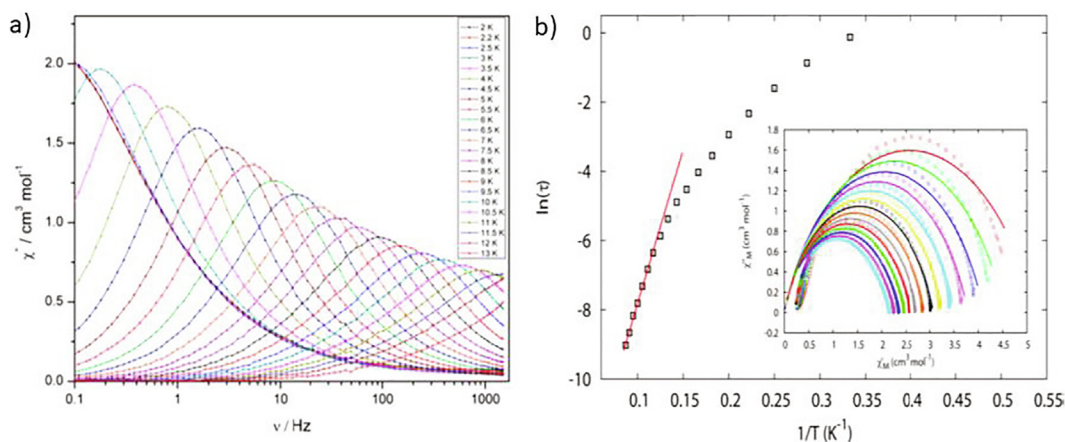
Fig. 61. Plots of χ″ vs ν (a) and plots of ln(τ) vs T^{-1} (b) for **66** under zero applied dc field. The solid red line is a fit to the Arrhenius law; inset Cole-Cole plots between 4 and 10.5 K, with the solid lines being best fits to the experimental data. Reprinted with permission from [71]. Copyright (2012) American Chemical Society.
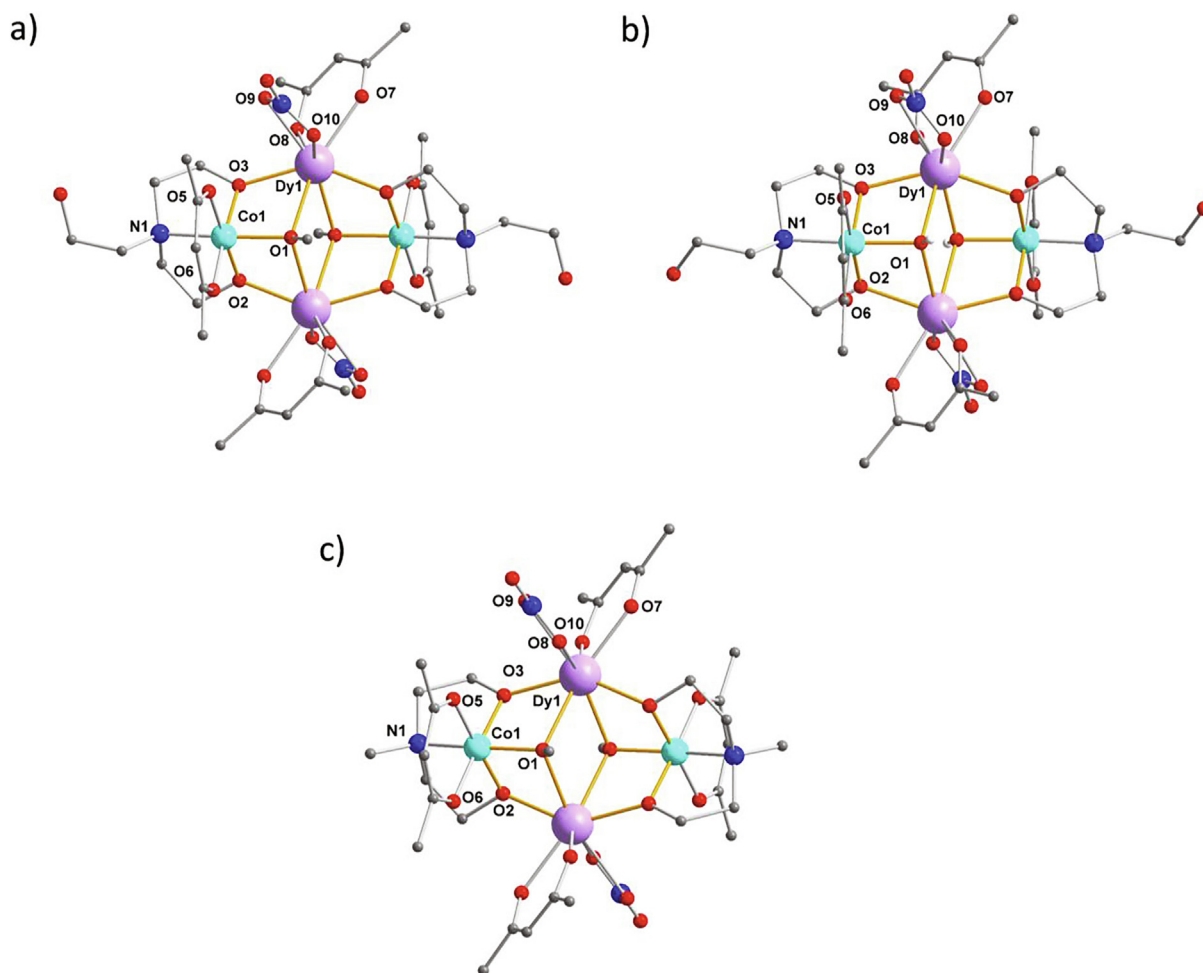
Fig. 62. The molecule structures of compounds **67** [Co$_2^{III}$Dy$_2$(OMe)$_2$(teaH)$_2$(acac)$_4$(NO$_3$)$_2$] (a), **68** [Co$_2^{III}$Dy$_2$(OH)$_2$(teaH)$_2$(acac)$_4$(NO$_3$)$_2$]·4H$_2$O (b), and **69** [Co$_2^{III}$Dy$_2$(OMe)$_2$(mdea)$_2$(acac)$_4$(NO$_3$)$_2$] (c).

[Cr$_2^{III}$Dy$_2$(OMe)$_2$(O$_2$CPh)$_4$(dea)$_2$(MeOH)$_4$](NO$_3$)$_2$ and b is isostructural to **5** [Cr$_2^{III}$Dy$_2$(OMe)$_2$(O$_2$CPh)$_4$(teaH)$_2$(NO$_3$)$_2$(MeOH)$_2$]. The l.s. Co^{III} ions are six-coordinate with distorted octahedral geometries and the Dy^{III} and Tb^{III} ions are eight coordinate with distorted square antiprismatic geometries (Table S8 for the estimated deviations for the idealized geometries).

Dc susceptibility measurements show similar decreases in χT with decreasing temperature for **65** Tb and **66** Dy, consistent with overall antiferromagnetic interactions between metal centers. For **66**, the {Co$_2^{III}$Dy$_2$} analogue, typical SMM behavior is observed with a barrier of 88.8 K (61.7 cm^{-1}) and τ_0 = 5.64 × 10^{-8} s (Fig. 61) under zero dc field. However, this fitting using an Arrhenius law is only valid for the high temperature part of the data and clearly fitting only part of the data with an Arrhenius law is not enough, since other relaxation processes are in operation. The {Co$_2^{III}$Tb$_2$} complex, **65**, showed field-induced SMM behavior. *Ab initio* calculations (Table 9) and experimental data reveal that QTM is greatly reduced in the {Co$_2^{III}$Dy$_2$} example compared to previously reported Dy^{III} SMMs and attributed as due to the weak antiferromagnetic dipolar coupling. Furthermore, dilution studies were performed and are in good agreement with the results of the *ab initio* calculations.

Through the replacement of the carboxylate ligands by acetylacetonate (acac), the same group isolated three related complexes, [Co$_2^{III}$Dy$_2$(OMe)$_2$(teaH)$_2$(acac)$_4$(NO$_3$)$_2$] **67**, [Co$_2^{III}$Dy$_2$(OH)$_2$(teaH)$_2$ (acac)$_4$(NO$_3$)$_2$]·4H$_2$O **68**, and [Co$_2^{III}$Dy$_2$(OMe)$_2$(mdea)$_2$(acac)$_4$(NO$_3$)$_2$] **69** [72]. Compounds **67** and **69** crystallize in the triclinic space group *P-1*, while compound **68** crystallizes in the monoclinic space group *P2$_1$/c*. Compounds **66**–**68** (Fig. 62) are heterometallic tetranuclear clusters consisting of {Co$_2^{III}$Dy$_2$} ions displaying a planar butterfly motif of **Type II** and are isostructural to [Cr$_2^{III}$Dy$_2$(OMe)$_2$(R-dea)$_2$(acac)$_4$(NO$_3$)$_2$] (R = Me (**6**), Et (**7**) or ^{n}Bu (**8**)) (Fig. 62). All the low spin Co^{III} ions are six-coordinate displaying an octahedral geometry. All the Dy^{III} ions are eight-coordinate displaying distorted square antiprismatic geometry (Table S8 for the estimated deviations for the idealized geometries).

Dc susceptibility measurements show similar trends in χT upon cooling for **66**–**69**, consistent with the overall antiferromagnetic interactions observed for compound **66**. Compounds **67**–**69** all show SMM behavior under zero dc magnetic field (Fig. 63) with energy barriers of 27 K (18.8 cm^{-1}), 28 K (19.5 cm^{-1}) and 38 K (26.4 cm^{-1}), respectively. It is notable that changing two μ_3-OMe$^-$ (**68**) to two μ_3-OH$^-$ (**67**) shows negligible effect on the magnetic behavior. Two relaxation processes are observed for **67** and **69** under a small dc field (Fig. 64) with similar overall profiles. However, both the barrier height and quantum regime are subtly different between **67** and **69** and also different from the previously reported {Co$_2^{III}$Dy$_2$} SMM complex **66**. For all these compounds the significant distortions of the local Dy^{III} ion geometry may be responsible for the observation of multiple relaxation pathways. Dilution studies on the Dy^{III} sample of **69** using Y^{III} revealed that the single-molecule magnet behavior is also single ion in origin as found for compound **66**.

The replacement of one coordinated acetylacetonate by nitrate around a Ln^{III} and of teaH$^-$ for ^{n}Budea$^-$ in **67** results in two
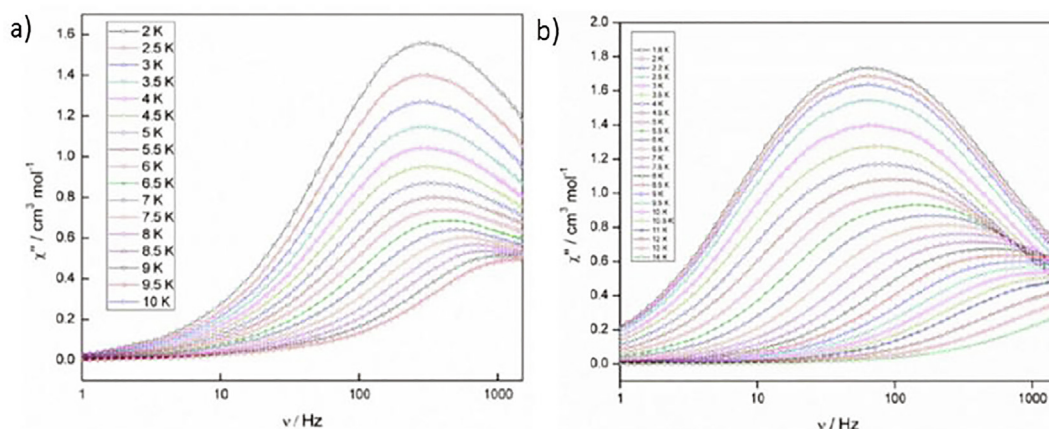
Fig. 63. Plots of χ'' vs ν for **67** (a) and **69** (b) under zero dc field. The solid lines are guides for the eyes. Reprinted with permission from [72]. Copyright (2013) American Chemical Society.
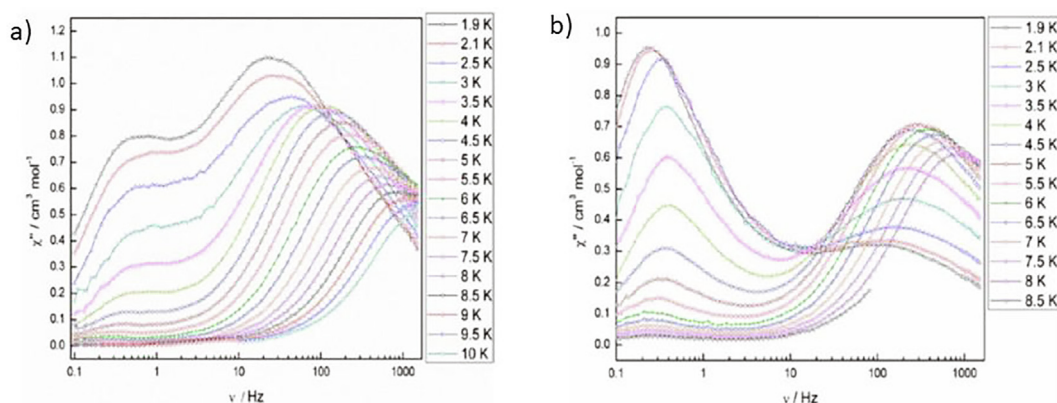
Fig. 64. Plots of χ'' vs ν under 3000 (a) and 6000 Oe (b) dc fields for **69**. The solid lines are guides for eyes. Reprinted with permission from [72]. Copyright (2013) American Chemical Society.
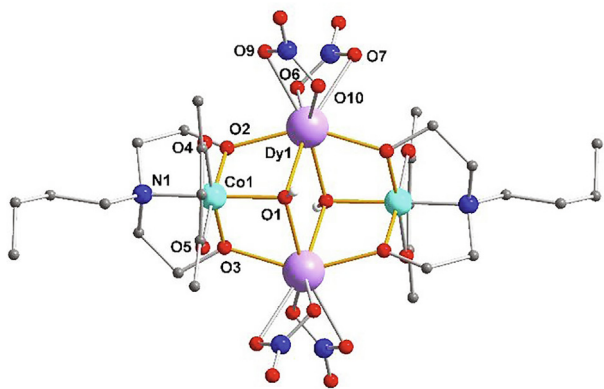
Fig. 65. molecular structure of $[Co_2^{III}Ln_2(OH)_2(^nBudea)_2(acac)_2(NO_3)_4]$ (Ln = Tb **70** and Dy **71**).

Fig. 67. Molecular structure of $[Co_2^{III}Ln_2(OMe)_2(teaH)_2(Piv)_6]$ (Ln = Dy **72**, Tb **73**, Ho **74**, Er **75** and Yb **76**).

isostructural heterometallic complexes of formula, $[Co_2^{III}Ln_2(OH)_2$ $(^nBudea)_2(acac)_2(NO_3)_4]$ (Ln = Tb **70** and Dy **71**) [73], which display a change in the acac:NO_3 ratio from 4:2 in **67** to 2:4 in **70** and **71**. Compounds **70** and **71** are isostructural, crystallizing in the monoclinic space group $P2_1/n$ (Fig. 65).

The χT product falls gradually with decreasing temperature and then rapidly at low temperature. Compound **70** {$Co_2^{III}Tb_2$} shows field-induced SMM behavior, which is similar to the {$Co_2^{III}Tb_2$} analogue compound **65**. The Dy^{III} analogue, **71**, displays typical SMM behavior under zero applied dc field (Fig. 66) with an energy barrier of 169 ± 5 K (117.5 cm^{-1}) and $\tau_0 = 1.47 \times 10^{-7}$ s. Remarkable differences were observed between compound **71** and the complexes **67**–**69** in terms of the low temperature dynamic behavior. Compound **71** shows better SMM behavior with a six times greater thermal barrier, slower relaxation and quantum tunneling (greater than 1.5 s) timescales compared with complexes **67**–**69** (Table 8). These results highlight the sensitivity of the Dy^{III} ions to the ligand field, which can thus have a large influence on the magnetic relaxation dynamics. Furthermore, this is a rare example where such a dramatic increase in U_{eff} arises from such a small perturbation of the ligand field environment.

The Alborés group reported another isostructural {$Co_2^{III}Ln_2$} family with formula $[Co_2^{III}Ln_2(OMe)_2(teaH)_2(Piv)_6]$, PivH = pivalic acid, (Ln = Dy **72**, Tb **73**, Ho **74**, Er **75** and Yb **76**) [74,76] formed by reaction of $[Co_2^{II}(\mu-H_2O)(Piv)_4(HPiv)_4]$ and $Ln(NO_3)_3 \cdot xH_2O$ with teaH$_3$ in MeCN. For example, compound **72** (Fig. 67) which crystallizes in the triclinic space group P-1, with a {$Co_2^{III}Dy_2$} butterfly core of **Type II** has a structure similar to compound **66**a but with the four PhCOO$^-$ bridging between Co^{III} and Dy^{III} ions are replaced by pivalates in
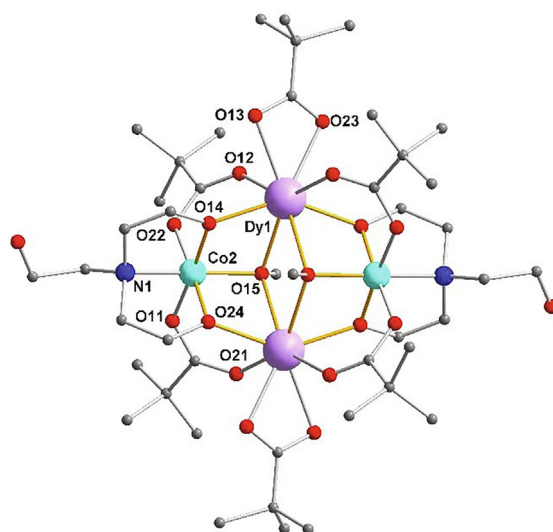
compound **72**. The pairs of terminal MeOH molecules coordinated to the Dy^{III} ion in **66** are replaced by two chelating pivalates in **72**. The Co^{III} ions are six coordinate displaying distorted octahedral coordination geometry and the Dy^{III} ions are eight coordinate with a distorted square antiprismatic coordination geometry (Table S8 for the estimated deviations for the idealized geometries).

The dc susceptibility measurements show similar decreases in χT with decreasing temperature for **72**–**76**, consistent with overall antiferromagnetic interactions. From ac susceptibility measurements it was found that compound **72** shows two well separated relaxation pathways at zero dc field with energy barriers of 51 K (35.4 cm^{-1}) and 127 K (88.3 cm^{-1}) (Fig. 68c), which is different from the observations for some of the previously reported {Co_2^{III}-Dy_2} complexes, in which a second well resolved pathway can only be observed through application of an external dc magnetic field. In order to explore the relaxation mechanisms further ac susceptibilities under different fields (0–3000 Oe) at 2 K at driving frequencies between 10 and 1500 Hz and complete frequency- and temperature-dependence measurement at 1500 Oe applied dc field were performed. Under 1500 Oe applied dc field, two relaxation processes are also seen but with lower resolution than at zero dc field and a third relaxation process is present. For the slow relaxation process (S) (Fig. 68d), two almost identical best fitting parameter sets are obtained with n = 5 or 7, that is, U_{eff} = 89 K, $\tau_0 = 5.4 \times 10^{-8}$ s, C_{Ram} =
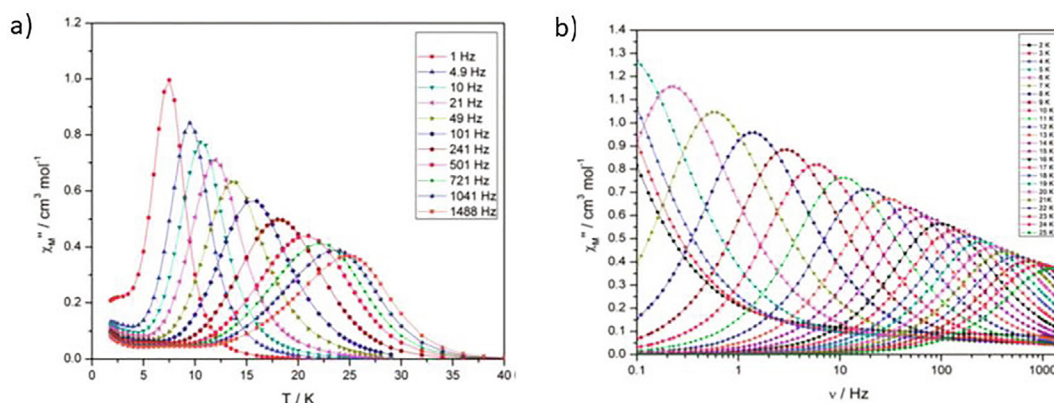
Fig. 66. Plots of χ'' vs T (a) and ν (b) for **71** under zero dc field. Reprinted with permission from [73]. Copyright (2013) The Royal Society of Chemistry.
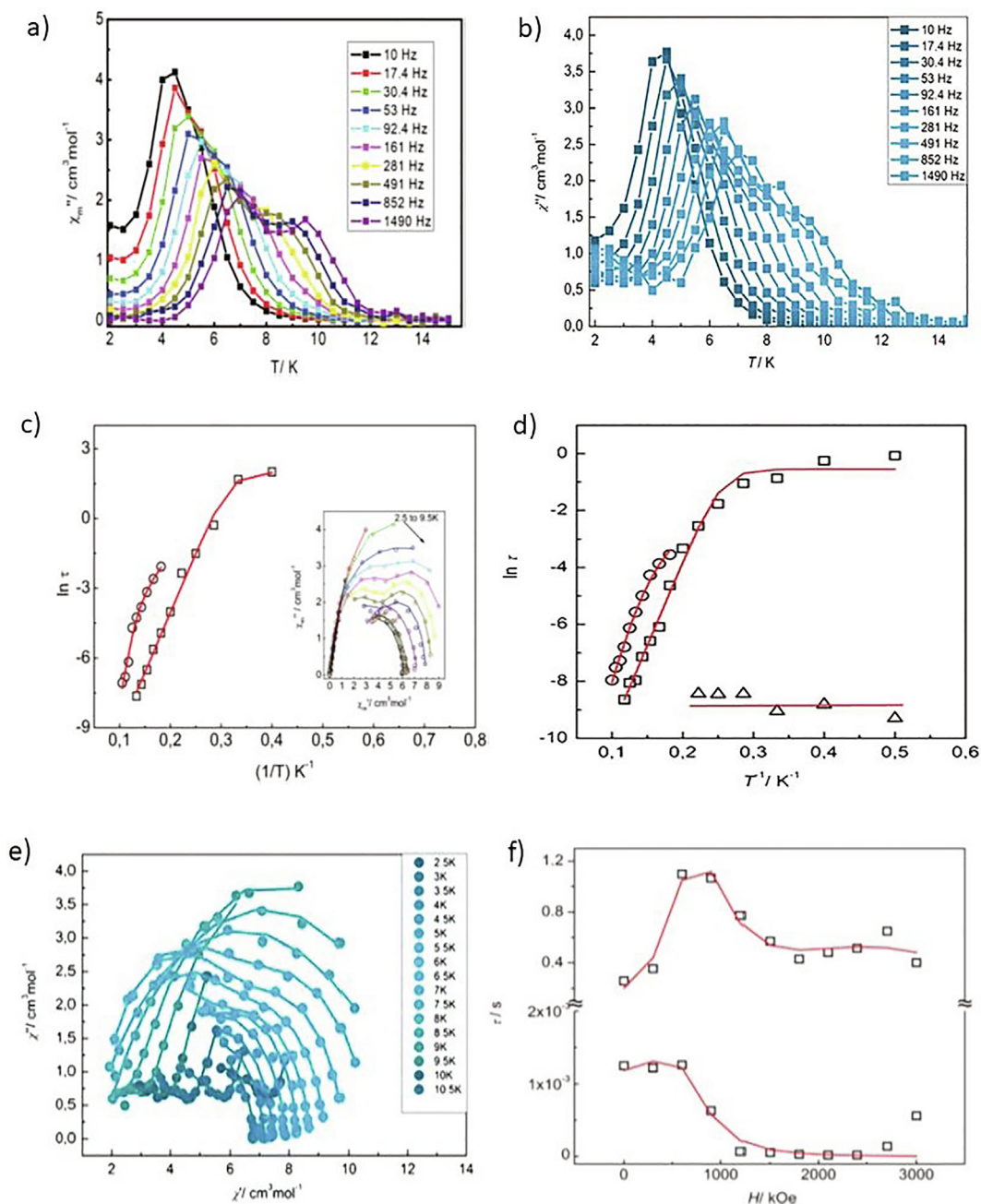
Fig. 68. Plots of χ'' vs T for **72** under zero dc field (a) and 1500 Oe dc field (b), lines are guide for eyes; ln τ vs. T^{-1} plots for **72** (open symbols for different relaxation processes under zero dc field (c) and 1500 Oe dc field (d). Circles: Slow process (S), squares: Fast process (F), triangles: temperature-independent process. Inset: Cole-Cole plots (circles) with best fitting (lines). Cole-Cole plots (circles) with best fitting under 1500 Oe dc field. Field dependence of the characteristic relaxation time at 2 K for compound **72**. Red lines is best fitting curves. Reprinted with permission from [74]. Copyright (2014) The Royal Society of Chemistry.

5.5×10^{-3} s^{-1} K^{-5} (n = 5) and U_{eff} = 104 K, τ_0 = 2.2 $\times$ 10^{-8} s, C$_{Ram}$ = 1. 7 $\times$ 10^{-4} s^{-1} K^{-7} (n = 7) (Table 8). A reasonable fit including only the Raman component with n = 7 and C$_{Ram}$ = 2.2 $\times$ 10^{-4} s^{-1} K^{-7} can be obtained. In the case of the fast relaxation process (F) a good fit is obtained with parameters of U_{eff} = 59 K, τ_0 = 1.7 $\times$ 10^{-7} s, and τ_{QT} = 0.58 s (Table 8) and in this case, a linear Arrhenius regime without Raman contribution describes the data. The third temperature-independent relaxation process was attributed to magnetization quantum tunnelling with τ_{QT} = 2.0 $\times$ 10^{-4} s.

The field dependence of the relaxation times also can be evaluated. For the fast process a reasonable fitting can be obtained with parameters of A$_1$ = 1.9 $\times$ 10^{-9} s^{-1} K^{-1} Oe^{-4} as well as B$_1$ = 844 s^{-1} and B$_2$ = 1.4 $\times$ 10^{-6} Oe^{-2}. The slow process is more complicated,

where two overlapping relaxation pathways are distinguished. It is possible to account for them through Equation (15) for each independent pathway: A$_1$ = 5.2 $\times$ 10^{-13} s^{-1} K^{-1} Oe^{-4}, B$_1$ = 135 s^{-1} and B$_2$ = 3.5 $\times$ 10^{-4} Oe^{-2} for the slower process and A$_1$ = 6.0 $\times$ 10^{-15} s^{-1} K^{-1} Oe^{-4}, B$_1$ = 5.1 s^{-1}, and B$_2$ = 3.8 $\times$ 10^{-7} Oe^{-2} for the faster process. These results are in agreement with the temperature-dependent data at 1500 Oe applied dc external field where also three independent processes were observed in the Cole-Cole plots (Fig. 68e). This makes the system a good example for analyzing multiple relaxation processes (Fig. 68f).

None of the other explored members of this {Co$_2^{III}$Ln$_2$} (Ln = Tb **73**, Ho **74**, Er **75**, Yb **76**) family shows slow relaxation of magnetization under zero dc field. However, all of them show field induced

SMM behavior. Compound **73** Tb[III] shows a very weak response without maxima. No reasonable parameters were obtained by fitting the Cole-Cole plots for the Ho[III] compound **74**, but it was possible to extract dynamic information with energy barrier of 43.2 K (30.0 cm^{−1}) and $\tau_0 = 6.2 \times 10^{-9}$ s from the maxima in the χ'' vs frequency. Complexes **75**, Er and **76**, Yb are also field-induced SMMs (Fig. 69). Two distinct relaxation processes were found for the Er[III] compound **75**, one of them essentially temperature independent. As seen from the ln τ vs T^{-1} plots (Fig. 70), there is no clear linear regime over the whole temperature range for complex **75** Er, while for **76** Yb a linear regime is seen in the high temperature range. The results indicate an Orbach regime for the compound **76** Yb, which is not the case for the **75** Er analogue. The relaxation times can be further analyzed in terms of the following general equations:

$\tau^{-1} = CT^n + \tau_{QTM}^{-1}$ for **75** Er and $\tau^{-1} = \tau_{QTM}^{-1} + \tau_0^{-1}\exp(-U_{eff}/K_BT)$ for **76** Yb. The best fitting gave parameters of $C_{raman} = 3.5 \times 10^{-2}$ s[−1] K[−7] (n = 7) and $\tau_{QT} = 5.1 \times 10^{-3}$ s for **75** Er and U_{eff} = 33.1 K (23 cm^{−1}), $\tau_0 = 2.1 \times 10^{-6}$ s and $\tau_{QTM} = 1.3 \times 10^{-2}$ s for **76** Yb (Table 8).

In order to gain a deeper understanding of the relaxation mechanism(s) in such systems, the Murray group continued to study this particular system by careful variation of the reaction conditions to isolate chemical/structural variants of compound **66**. Using the amine-based diol ligands, diethanolamine (deaH$_2$), N-methyldiethanolamine (mdeaH$_2$) and N-n-butyldiethanolamine ([n]BudeaH$_2$) in place of triethanolamine (teaH$_3$), in conjunction with benzoic acid, several related compounds could be isolated. The use of deaH$_2$ gave the cationic form of compound **66**, [Co$_2^{III}$Dy$_2$
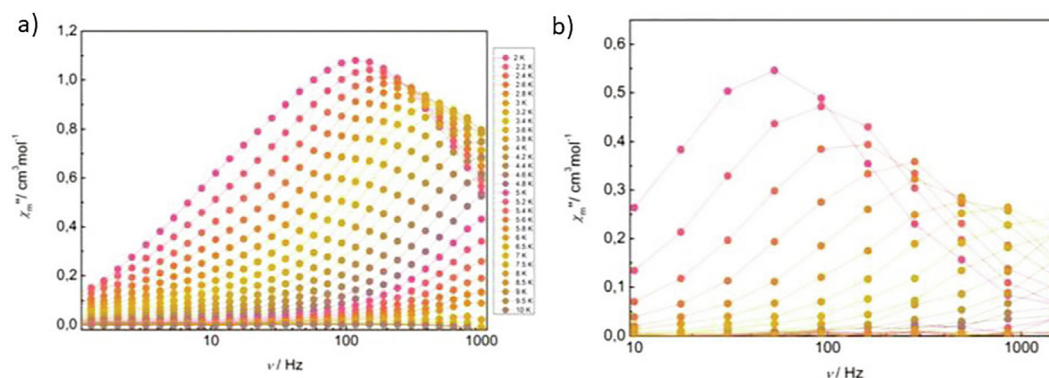
Fig. 69. Plots of χ'' vs ν for **75** Er (a) and **76** Yb (b) under 1500 Oe dc applied field. Full lines are just for guiding the eye. Frequency dependence plot is shown in logarithmic scale. Reprinted with permission from [76]. Copyright (2017) The Royal Society of Chemistry.
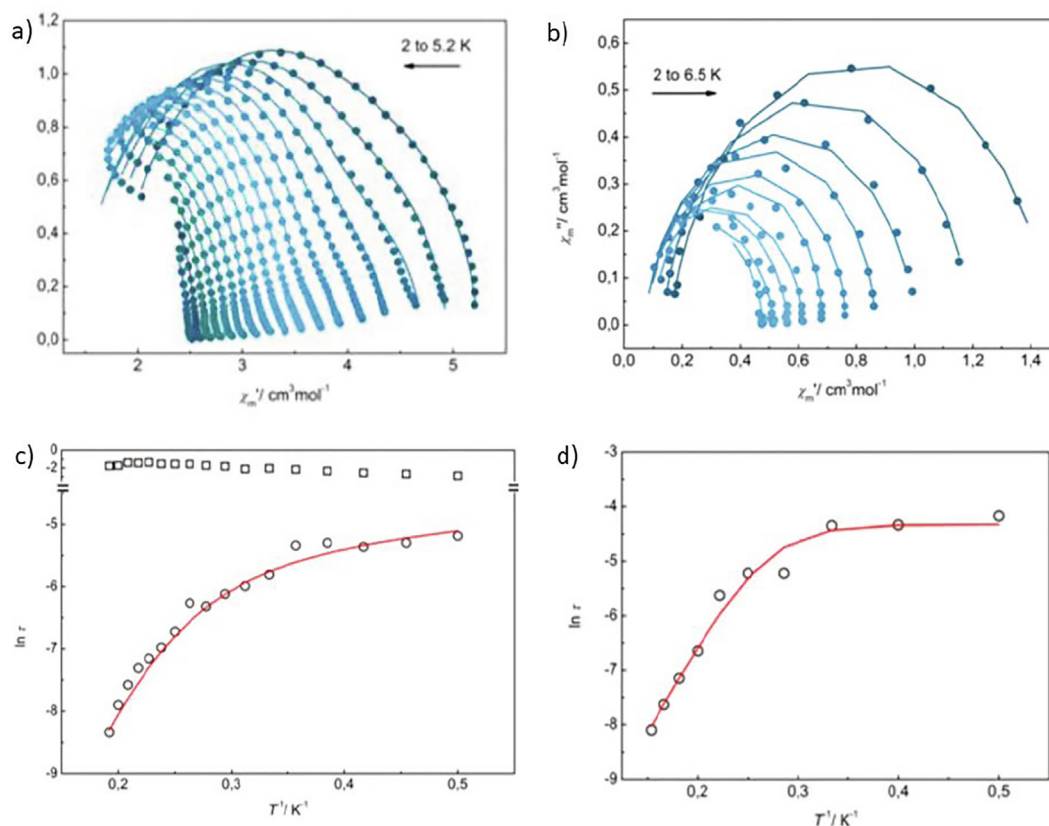
Fig. 70. Cole-Cole plots for complexes **75** Er (a) and **76** Yb (b) under 1500 Oe dc field and plots of ln τ vs T^{-1} for complexes **75** Er (c) and **76** Yb (d). Full line: best fitting. Squares: temperature independent relaxation process. Reprinted with permission from [76]. Copyright (2017) The Royal Society of Chemistry.

$(OMe)_2(dea)_2(O_2CPh)_4(MeOH)_4](NO_3)_2$ **77**. The use of mdeaH$_2$ resulted in a neutral complex with the formula $[Co_2^{III}Dy_2(OMe)_2$ $(mdea)_2(O_2CPh)_4(NO_3)_2]$ **78**. The coordination environment around the Dy^{III} centers differs from those previously seen since each carries a bidentate nitrate ligand.

The reaction utilizing ^{n}BudeaH$_2$ resulted in the isolation of two unique complexes in the asymmetric unit of formula $[Co_2^{III}Dy_2$ $(OMe)_2(^nBudea)_2(O_2CPh)_4(MeOH)_4](NO_3)_2 \cdot 0.5MeOH \cdot H_2O$ (a) and $[Co_2^{III}Dy_2$ $(OMe)_2(^nBudea)_2(O_2CPh)_4(MeOH)_2(NO_3)_2] \cdot MeOH \cdot 1.5H_2O$ (b) **79** (**79** = **79a** plus **79b**) (Fig. 71) [77], which are structurally similar to those in **66**.

The dc susceptibilities measured for **77–79** show similar behavior to that for compound $[Co_2^{III}Dy_2(OMe)_2(teaH)_2(O_2CPh)_4(MeOH)_4]$ $(NO_3)_2$ plus $[Co_2^{III}Dy_2(OMe)_2(teaH)_2(O_2CPh)_4(MeOH)_2(NO_3)_2]$ **66** (i.e. two molecules per asymmetric unit) with a steeper decrease in the χT product for **79** than for that for **66**, **77** and **78**. Ac magnetic susceptibility measurements showed that the in-phase (χ') and out-of-phase (χ'') signals are frequency (Fig. 72) and temperature dependent below 20 K for **77–79** with typical features of SMM behavior, which is not surprising, since each are closely related to **69** $[Co_2^{III}Dy_2(OMe)_2(mdea)_2(acac)_4(NO_3)_2]$. The $\ln(\tau)$ vs T^{-1} plots show differences within the dynamic magnetic behavior for **77–79**. All display a thermally activated relaxation mechanism above 8.5 K, with energy barriers of 79.14 K (55 cm^{-1}) for **78**, 87.77 K (61 cm^{-1}) for **66**, 103.60 K (72 cm^{-1}) for **77**, and 115.11 K (80 cm^{-1}) for **79** (Table 8). *Ab initio* calculations and the experimental data indicate that the variation in barrier height is related to changes in the coordination and geometric environments around the Dy^{III} ions of each complex (Table 9). The dipolar interactions are dominant (Table 9). This gives further proof that the magnetic

relaxation dynamics of Ln^{III} ions are sensitive to the ligand field. These results also indicate that the SMM properties can be fine-tuned through simple substitution of ligands both near to or distant from the magnetic centers.

In the light of the remarkable changes of the magnetic properties induced through subtle chemical modifications, the Murray group extended their exploration of these effects by studying another system in which all of the co-ligands are replaced by $[acac]^-$: $[Co_2^{III}Dy_2(OH)_2(teaH)_2(acac)_6] \cdot MeCN$ **80**, $[Co_2^{III}Dy_2(OH)_2(^n-Budea)_2(acac)_6] \cdot 2H_2O$ **81** and $[Co_2^{III}Dy_2(OH)_2(edea)_2(acac)_6] \cdot 2H_2O \cdot 4MeCN$ **82** (edeaH$_2$ = *N*-ethyldiethanolamine) (Fig. 73) [78]. These are isostructural to **17**, $[Cr_2^{III}Dy_2(OMe)_2(mdea)_2(hfacac)_6]$, and very close to the structure of $[Co_2^{III}Dy_2(OR)_2(L)_2(acac)_4(NO_3)_2]$, with L = teaH^{2-} and R = Me **68**, L = teaH^{2-} and R = H **69** and L = mdea^{2-} and R = Me **70** and $[Co_2^{III}Dy_2(OH)_2(^nBudea)_2(acac)_2(NO_3)_4]$ **71**.

Dc magnetic susceptibility measurements on complexes **80–82** show similar behavior to those of the previously discussed analogues **68–71**. Compound **80** displays classic SMM behavior with two Orbach relaxation processes of $U_{eff}1$ = 71 K (49.3 cm^{-1}) and τ_0 = 2.7 × 10^{-7} s at high temperature and $U_{eff}2$ = 45 K (31.3 cm^{-1}) and τ_0 = 3.2 × 10^{-7} s at low temperature (Fig. 74). The QTM for the slower relaxation process was fitted separately with a value of 7.6 × 10^{-2} s (see Table 8). The two processes could be due to the presence of two crystallographically unique structural species. Compound **81** shows also typical SMM behavior with a barrier of 27 K (18.8 cm^{-1}) under zero dc field and displays a single process. Complex **81** shows fast QTM below 3 K, which can be significantly reduced by applied an optimal dc field evidenced by the height increase of energy barrier (27 K (18.8 cm^{-1})) at zero dc field and 38 K (26.4 cm^{-1}) at 500 Oe dc field. Compound **82** is
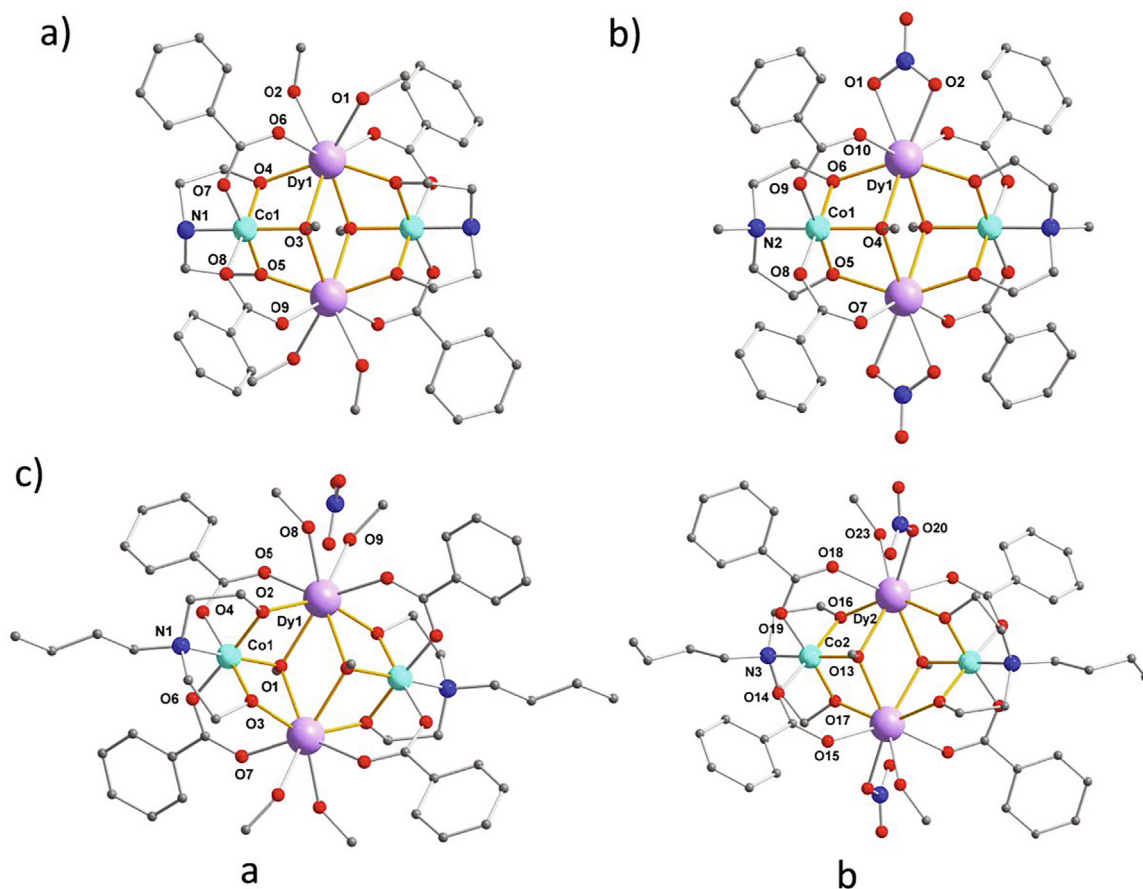
Fig. 71. Molecular structures of **77** $[Co_2^{III}Dy_2(OMe)_2(dea)_2(O_2CPh)_4(MeOH)_4](NO_3)_2$ (a), **78** $[Co_2^{III}Dy_2 (OMe)_2(mdea)_2(O_2CPh)_4(NO_3)_2]$ (b) and $[Co_2^{III}Dy_2(OMe)_2(^nBudea)_2(O_2CPh)_4 (MeOH)_4](NO_3)_2 \cdot 0.5MeOH \cdot H_2O$, **79a** plus $[Co_2^{III}Dy_2(OMe)_2(^nBudea)_2(O_2CPh)_4(MeOH)_2(NO_3)_2] \cdot MeOH \cdot 1.5H_2O$, **79b** (c).
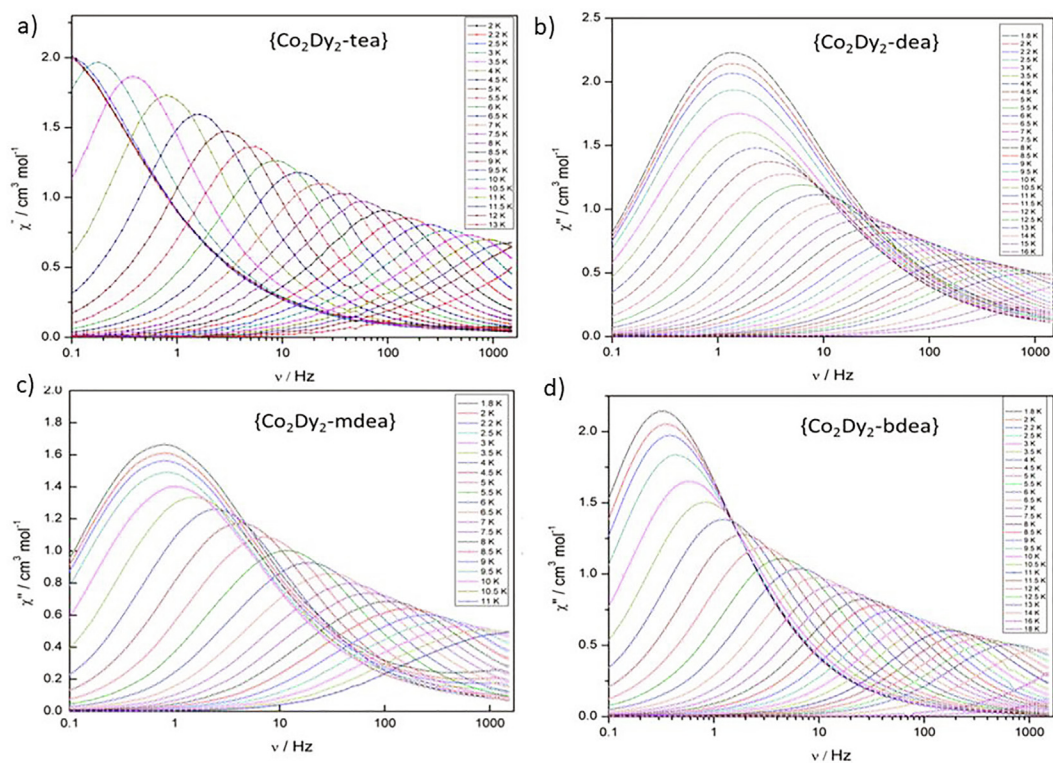
Fig. 72. Plots of χ'' vs ν for complexes **66** (a), **77** (b), **78** (c) and **79** (d) under zero dc field. Reprinted with permission from [77]. Copyright (2014) American Chemical Society.
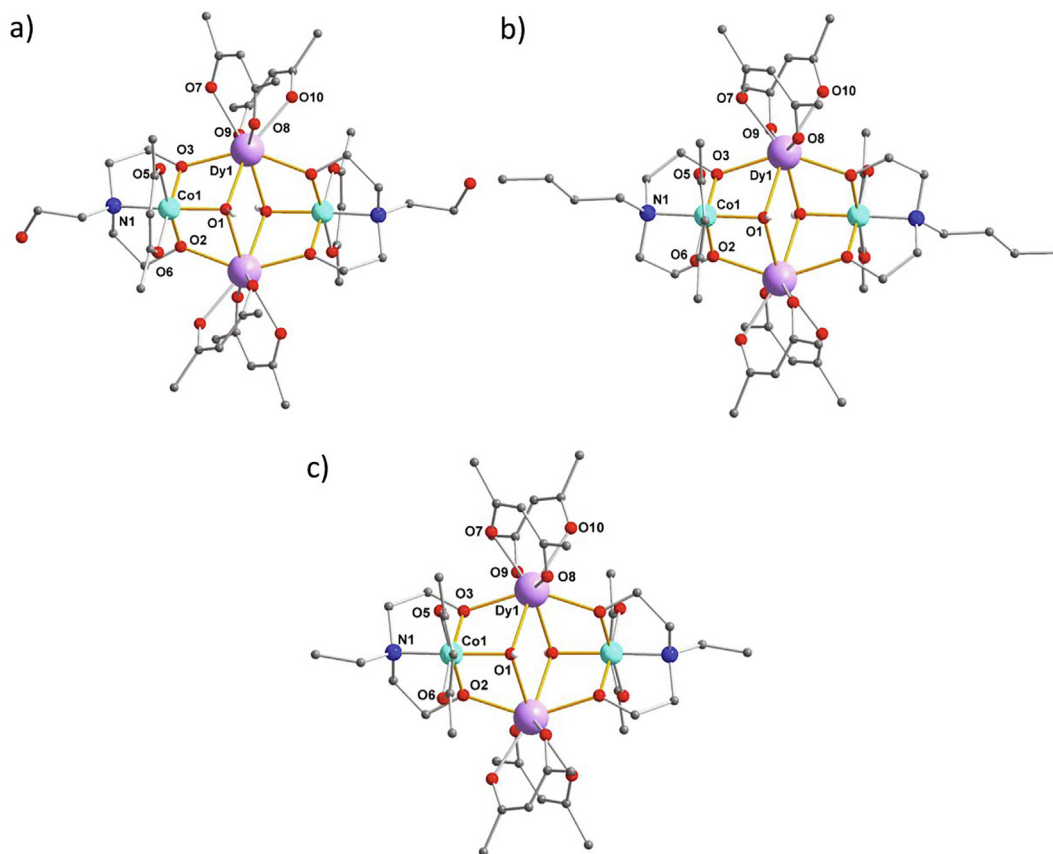
Fig. 73. molecule structures of **80** [Co$_2^{III}$Dy$_2$(OH)$_2$(teaH)$_2$(acac)$_6$]·MeCN (a), **81** [Co$_2^{III}$Dy$_2$(OH)$_2$(^{n}Budea)$_2$(acac)$_6$]·2H$_2$O (b) and **82** [Co$_2^{III}$Dy$_2$(OH)$_2$(edea)$_2$(acac)$_6$]·2H$_2$O·4MeCN (c).
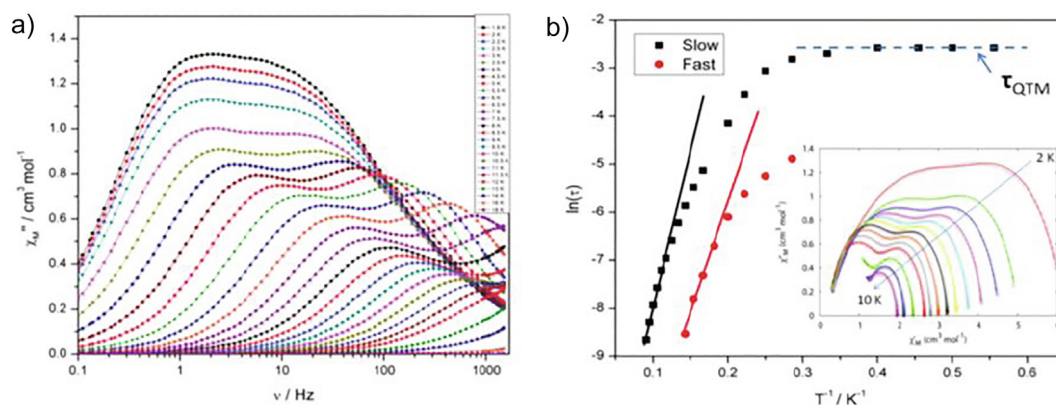
Fig. 74. Plots of χ'' vs ν (a) and plots of $\ln(\tau)$ vs T^{-1} (b) for compound **81**. (b inset) Cole-Cole plots of **81** at temperatures range 2–10 K. The solid lines are fits of the experimental data using a generalized Debye model. Reprinted with permission from [78]. Copyright (2015) The Royal Society of Chemistry.

a field-induced SMM with U_{eff} = 16 K (11.1 cm^{-1}) under applied optimal field of 1000 Oe.

Different dynamic behavior is seen for **80–82** depending on the aminopolyalcohol ligand used with the heights of the energy barriers following the trend teaH^{2-} > ^{n}Budea^{2-} > edea^{2-}. For **67** [Co$_2^{III}$Dy$_2$(OMe)$_2$(teaH)$_2$(acac)$_4$(NO$_3$)$_2$] and **69** [Co$_2^{III}$Dy$_2$(OMe)$_2$(mdea)$_2$(acac)$_4$(NO$_3$)$_2$] **69** has the larger U_{eff} value suggesting an overall trend of mdea^{2-} > teaH^{2-} > ^{n}Budea^{2-} > edea^{2-} in these systems. It was also found that swapping the two μ_3-OH$^-$ (**68**) with two μ_3-OMe$^-$ groups (**69**) had no significant effect on the relaxation dynamics.

Another interesting comparison is gauging the effect of the chelating anions coordinated to the Ln^{III} ions. The comparison of [Co$_2^{III}$Dy$_2$(OH)$_2$(^{n}Budea)$_2$(acac)$_2$(NO$_3$)$_4$] **71** (NO$_3^-$/NO$_3^-$) with

[Co$_2^{III}$Dy$_2$(OH)$_2$(^{n}Budea)$_2$(acac)$_6$] **81** (acac$^-$/acac$^-$) and [Co$_2^{III}$Dy$_2$(OMe)$_2$(teaH)$_2$(acac)$_4$(NO$_3$)$_2$] **67** (NO$_3^-$/acac$^-$) with [Co$_2^{III}$Dy$_2$(OH)$_2$(teaH)$_2$(acac)$_6$] **80** (acac$^-$/acac$^-$) reveals huge differences in dynamic magnetic behaviors, e.g. Fig. 66 for **71** vs Fig. 74 for **81** arising from the subtle changes in the ligand field around the Ln^{III} ion. These results show that here the most important consideration for modulating the dynamic properties is the choice of the coordinated anion. It also reveals that the U_{eff} value can be tuned by selection of the organic R group on the bridging aminopolyalcohol ligand.

The differences in the dynamic properties of the complexes **80–82** and the related complexes **67–69**, compared with those of **71** have been shown to originate from the presence of acac$^-$ ligands in **67–69** and **80–82** and their absence in **71**. Further possible
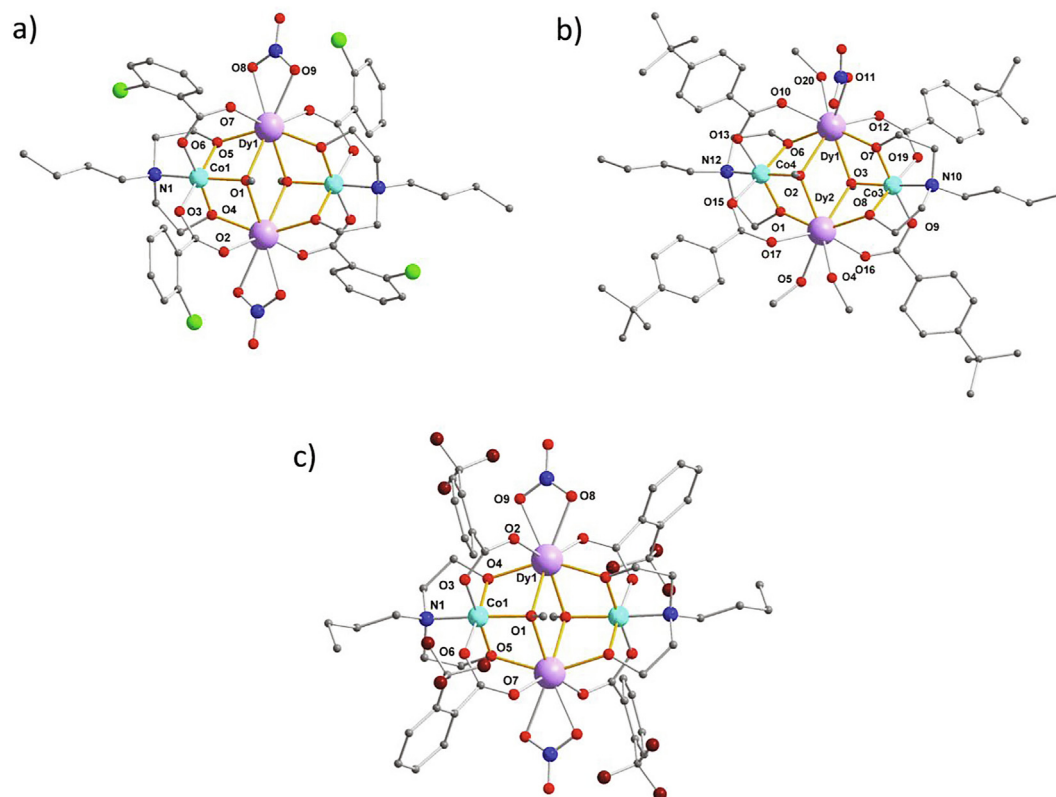
Fig. 75. Molecular structures of **83** [Co$_2^{III}$Dy$_2$(OMe)$_2$(o-Cl-PhCO$_2$)$_4$(^{n}Budea)$_2$(NO$_3$)$_2$] (a), **84** [Co$_2^{III}$Dy$_2$ (OMe)$_2$(p-^{t}Bu-PhCO$_2$)$_4$(^{n}Budea)$_2$(NO$_3$)(MeOH)$_3$](NO$_3$)·H$_2$O·MeOH (b) and **85** [Co$_2^{III}$Dy$_2$(OMe)(OH)(o-CF$_3$-PhCO$_2$)$_4$(^{n}Budea)$_2$(NO$_3$)$_2$]·MeOH (c).

methods to improve and explore the influences on the SMM properties of the core unit could be to replace the bridging OMe⁻ ligands with differently substituted OR⁻ groups with and to test the effect of adding various electron-donating or withdrawing groups on the aminopolyalcohol.

Following on from previous work, Murray explored the properties of $[Co_2^{III}Dy_2(OMe)_2(o\text{-}Cl\text{-}PhCO_2)_4(^nBudea)_2(NO_3)_2]$ **83**, $[Co_2^{III}Dy_2(OMe)_2(p\text{-}^tBu\text{-}PhCO_2)_4(^nBudea)_2(NO_3)(MeOH)_3](NO_3)\cdot H_2O\cdot MeOH$ **84** and $[Co_2^{III}Dy_2(OMe)(OH)(o\text{-}CF_3\text{-}PhCO_2)_4(^nBudea)_2(NO_3)_2]\cdot MeOH$ **85** [43], in order to investigate the carboxylic acid and β-diketonate ligands' effect on the magnetic dynamics. Compounds **83** and **85** (Fig. 75) crystallize in the triclinic space group *P-1* and are isostructural to $[Co_2^{III}Dy_2(OMe)_2(mdea)_2(O_2CPh)_4(NO_3)_2]$ **78** with the differences that the mdea²⁻ in **78** is $^nBudea^{2-}$ for **83** and **85** and the carboxylate is PhCOO⁻ for **78** and *o*-Cl-PhCOO⁻ for **83** and *o*-CF₃-PhCOO⁻ for **85**) (Fig. 67). Compound **85** crystallizes in the monoclinic space group *P2₁/n*. The difference for **85** lies in the terminal ligands on the central Dy^III ions and the substituents on the bridging benzoates. As shown in Fig. 75, Dy1 is coordinated by a chelating nitrate and a MeOH ligand whereas Dy2 has two MeOH ligands. Thus, the complex is a monocation with one nitrate counteranion per cluster in the crystal lattice. All the Dy^III in this series are eight-coordinate with distorted square antiprismatic geometries and all the l. s. Co^III ions are six-coordinate with octahedral geometries (Table S8).

Ac susceptibility measurements for **83–85** reveal that all three compounds are typical SMMs with barriers of 115.7 K (80.4 cm⁻¹) for **83**, 110.6 K (76.9 cm⁻¹) for **84** and 126.8 K (88.1 cm⁻¹) for **85** (Fig. 76). Experimental results and theoretical calculations on complexes **83** and **85** indicate that subtle chemical changes can lead to a significant enhancement of the barrier height. The differences can be attributed to the *ortho*-substituents on the benzoate ligands (Cl, **83** versus CF₃, **85**), which is consistent with the observations in the {Fe₂^IIIDy₂} butterfly complexes [42]. The effect of *ortho*-substituted groups on benzoate ligands has also recently been highlighted by Murugesu and co-workers, especially for electron withdrawing groups on ligands that are directly coordinated to the Ln^III ion [80]. For compound **84**, two distinct relaxation processes are observed, which are ascribed to the two different Dy^III ions with their two distinct coordination environments in terms of the terminal ligands. This leads to different low lying electronic structures with their different relaxation timescales confirmed by *ab initio* calculations.

More recently, the Murray group reported the $[Co_2^{III}Ln_2(OH)_2(o\text{-}Me\text{-}PhCO_2)_4(mdea)_2(NO_3)_2]$ (Ln = Dy **86**, Tb **87**, Ho **88**) butterfly clusters (Fig. 77) [79]. This family contains relatives of the previously reported {Co₂^IIILn₂} butterfly compound **77** with R changed from H to Me on the μ₃-OR group.

Dc magnetic susceptibility measurements reveal antiferromagnetic exchange coupling between the two Ln^III ions for all three
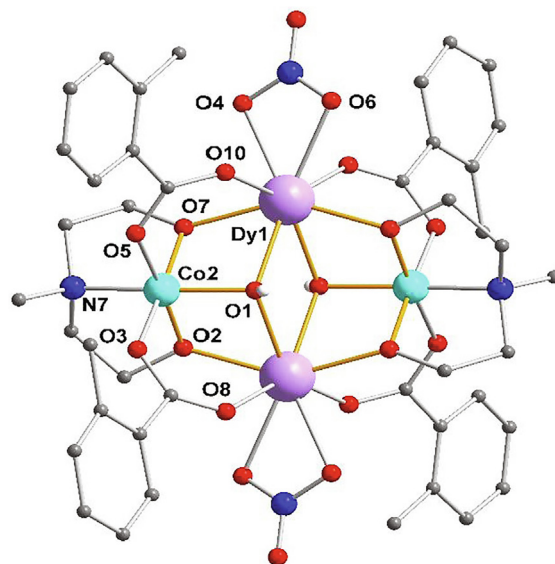
Fig. 77. Molecular structure of compound **86** $[Co_2^{III}Ln_2(OH)_2(o\text{-}Me\text{-}PhCO_2)_4(mdea)_2(NO_3)_2]$.

complexes. Ac magnetic susceptibility measurements reveal classic single-molecule magnet (SMM) behavior for complex **86** with U_{eff} = 116.8 K (81.2 cm⁻¹) under zero dc field (Fig. 78). Complexes **87** and **88** exhibit field-induced SMM behavior, however only compound **87** shows maxima with U_{eff} = 49.2 K (34.2 cm⁻¹). The relaxation processes can be fitted combining Orbach and QTM processes for **86** (Table 8). The diamagnetic Co^III ion effect on the magnetic dynamic was probed via *ab initio* and DFT calculations. The results strongly suggest that the Co^III ions are integral to the observation of SMM behavior in these systems and in silico i. e. K⁺ or Zn^II in place of diamagnetic Co^III ions was found to increase the transverse anisotropy of the ground state, leading to a significant QTM relaxation process. Furthermore, the calculations also predict other diamagnetic metal ions such as K⁺ and Zn^II in the place of diamagnetic Co^III can affect the relaxation behavior. The results indicate replacement with these ions may yield better-performing SMMs with longer relaxation times since their electrostatic charge polarizations are larger than that for Co^III ions. They are also 'properly' diamagnetic with $4s^0$ and $4s^03d^0$ configurations rather than $4s^03d^6$. Low spin Co^III also has accessible paramagnetic excited states with Pauli magnetism. The local dipolar field of Dy^III could easily be enough to populate the excited states of Co^III.

Summary: Since the purpose of exploring replacement of paramagnetic 3d ions with diamagnetic alternatives is to keep all the other variables of the system the same in the two cases to be compared, in this section on {Co₂^IIILn₂} butterflies (Co^III is d^6 l.s
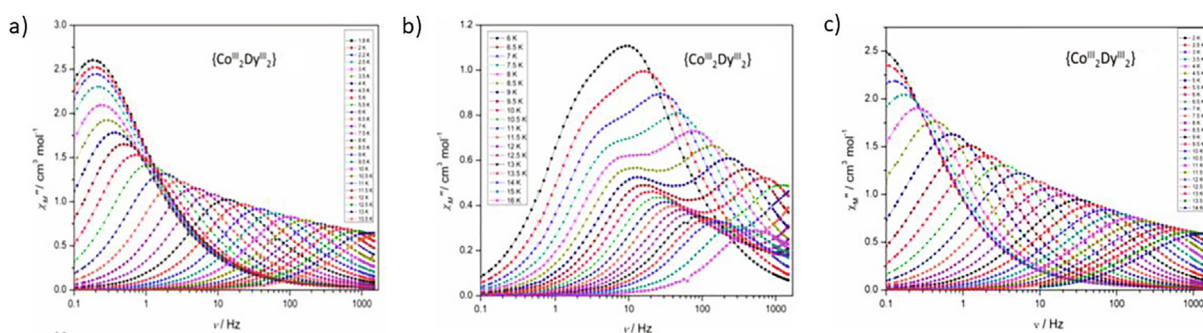
Fig. 76. Comparison of plots of χ″ vs ν for **83** (a), **84** (b) and **85** (c). Adopted with permission from [43]. Copyright (2015) American Chemical Society.
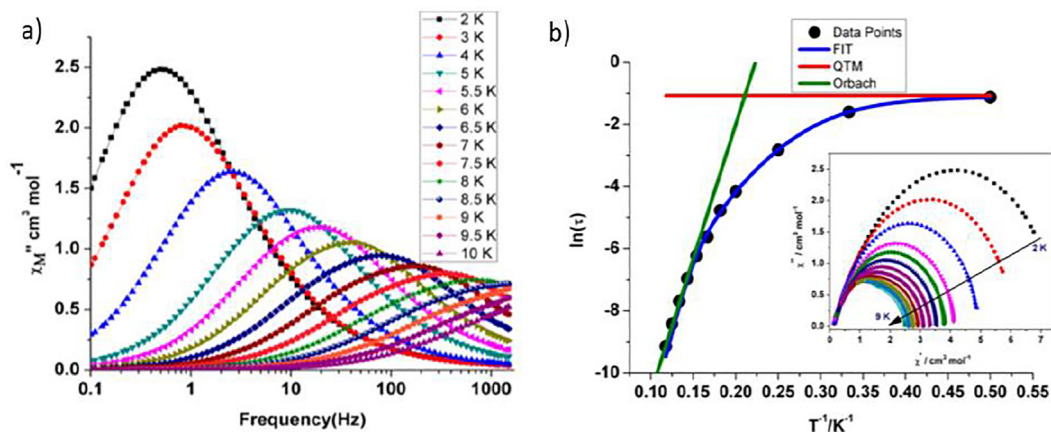
Fig. 78. Plots of χ'' vs ν (a) and plots of ln (τ) vs T^{-1} (b) for compound **86** under zero dc field. The horizontal red line represents the QTM relaxation time. (b inset) Cole-Cole plots between 2 and 9 K. Reprinted with permission from [79]. Copyright (2017) American Chemical Society.

and diamagnetic) we only compare the examples for ({Co$_2^{III}$Ln$_2$} vs {Cr$_2^{III}$Ln$_2$}) where this is the case. Specifically, we can compare the magnetic behavior of **1** (U_{eff} = 54 cm^{-1} and τ_0 = 5.1 × 10^{-8} s) and **78** (U_{eff} = 55 cm^{-1} and τ_0 = 1.03 × 10^{-7} s), **2** (U_{eff} = 43.2 cm^{-1} and τ_0 = 2.3 × 10^{-7} s) and **77** (U_{eff} = 72 cm^{-1} and τ_0 = 6.05 × 10^{-8} s), **6** (U_{eff} = 24 cm^{-1} and τ_0 = 1.2 × 10^{-7} s) and **69** (U_{eff} = 26.4 cm^{-1} and τ_0 = 2.6 × 10^{-6} s) (Table 8). Note that although compound **66**b corresponds to compound **5**, the presence of **66**a in the lattice makes direct comparison impossible and will not be discussed. All the results indicate that the interactions between Cr^{III} and Dy^{III} ions partly suppress the ZF-QTM leading to open hysteresis loops. As seen in Table 9, *ab initio* calculations were performed by three different groups. Compounds **66**, **77–79** and **82** were analyzed using two strongly anisotropic centers (Ising exchange) Lines model [81]. Antiferromagnetic interactions dominate for these complexes. For compounds **72** and **86**–**88**, only an exchange Hamiltonian was analyzed, which makes the comparison between these complexes tricky and the magneto-structural correlations impossible. However, it is obvious that the interaction between Dy^{III} ions plays an important role in the SMM behavior.

3.3. Other M (diamagnetic)/4f systems

3.3.1. {Mg$_2^{II}$Ln$_2$} systems

The Winpenny group reported the **Type I** {Mg$_2^{II}$Ln$_2$} butterfly SMM compounds, [^{i}PrNH$_2$]$_2$[Mg$_2^{II}$Ln$_2$(OH)$_2$(Piv)$_{10}$], (Ln = Dy **89** and Er **90**) (Fig. 79). [50] These crystallize in the monoclinic space group $P2_1/c$ and are isostructural to compound **46** [^{i}Pr$_2$NH$_2$]$_2$ [Co$_2$Dy$_2$(OH)$_2$(Piv)$_{10}$].

Ac susceptibility measurements indicate **89** is a typical SMM under zero dc field with clear peaks in the out-of-phase susceptibility (χ'') (Fig. 80a and b) with U_{eff} = 44 K and τ_0 = 7.8 × 10^{-7} s (Fig. 80d). A fit to the Cole-Cole plots in the temperature range 1.8–9.5 K gives α parameters between 0.05 and 0.30 (Fig. 80c), indicating a distribution of relaxation times. For **90** {Mg$_2$Er$_2$}, clear peaks (Fig. 81a and b) could be observed with the optimal applied dc field of 1000 Oe. An Arrhenius fit to the high-temperature range gave U_{eff} = 23 K and τ_0 = 6.6 × 10^{-7}s (Fig. 81d). Cole-Cole plots show similar behavior to those for {Mg$_2^{II}$Dy$_2$}, with α = 0.035 at higher temperatures increasing to α = 0.2 at the lowest temperatures (Fig. 81c). For these two complexes, the low temperature region is dominated by QTM, which is typical for pure 4f based SMMs. No further analysis of the non-linear part of the ln (τ) vs T^{-1} plots was undertaken in this study.

Summary: This system provides a **Type I** core example where the central divalent 3d ions are replaced by diamagnetic Mg^{II}.
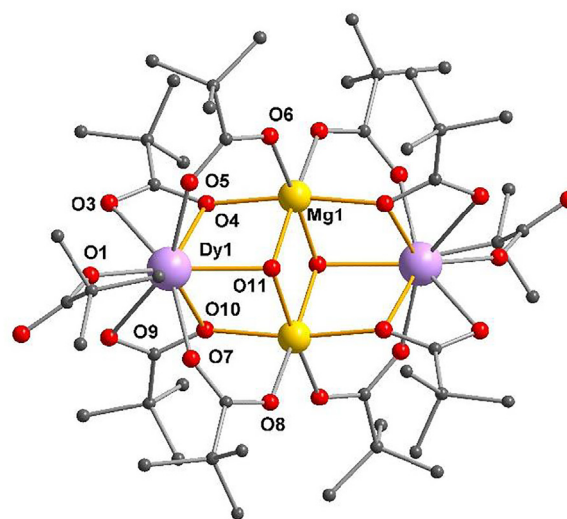
Fig. 79. Molecular structure of compound **89** [^{i}PrNH$_2$]$_2$[Mg$_2^{II}$Dy$_2$(OH)$_2$(Piv)$_{10}$].

The Ln^{III} ions are thus more isolated through the deletion of the paramagnetic M^{II} and the Ln^{III} single ion contribution can be seen. This allows for an ordering of influence of the nature of the 3d ion electron configuration to be assessed in terms of observed magnetic properties, backed up by *ab initio* and *DFT* calculations. The ordering of the 3d ions d^8 > d^9 > d^7 (Ni^{II}, Cu^{II}, Co^{II}) was established in terms of observation of maxima for the out-of-phase ac signals for compounds **54**, **56** and **46**. Moreover, the Mn^{III} analogue also shows SMM behavior which is better than that of the Ni^{II}, Cu^{II} and Co^{II} analogues. However, since the μ_3-OH$^-$ is replaced by μ_3-O^{2-} in this system, it is not possible to directly compare these compounds. Probably the Mn^{III} h.s ion "adds value" through the anisotropic contribution as a result of the axial J-T distortion.

In the case where Dy^{III} ions replaced by Er^{III} in the {Mg$_2^{II}$Ln$_2$} system, the slow relaxation can only be analyzed under applied dc field. The Dy^{III}-Dy^{III} dipolar interaction is clearly ferromagnetic in **89** {Mg$_2^{II}$Dy$_2$}, however in **90** {Mg$_2^{II}$Er$_2$} the Er^{III}-Er^{III} interaction becomes ambiguous.

3.3.2. {Al$_2^{III}$Ln$_2$} systems

Two {Al$_2^{III}$Ln$_2$} butterfly SMMs, [Al$_2^{III}$Ln$_2$(OH)$_2$(pdea)$_2$(p-Me-PhCO$_2$)$_6$], (Ln = Dy **91** and Er **92**) with the **Type I** core were reported by the Powell group [23,25]. Both compounds crystallize in the
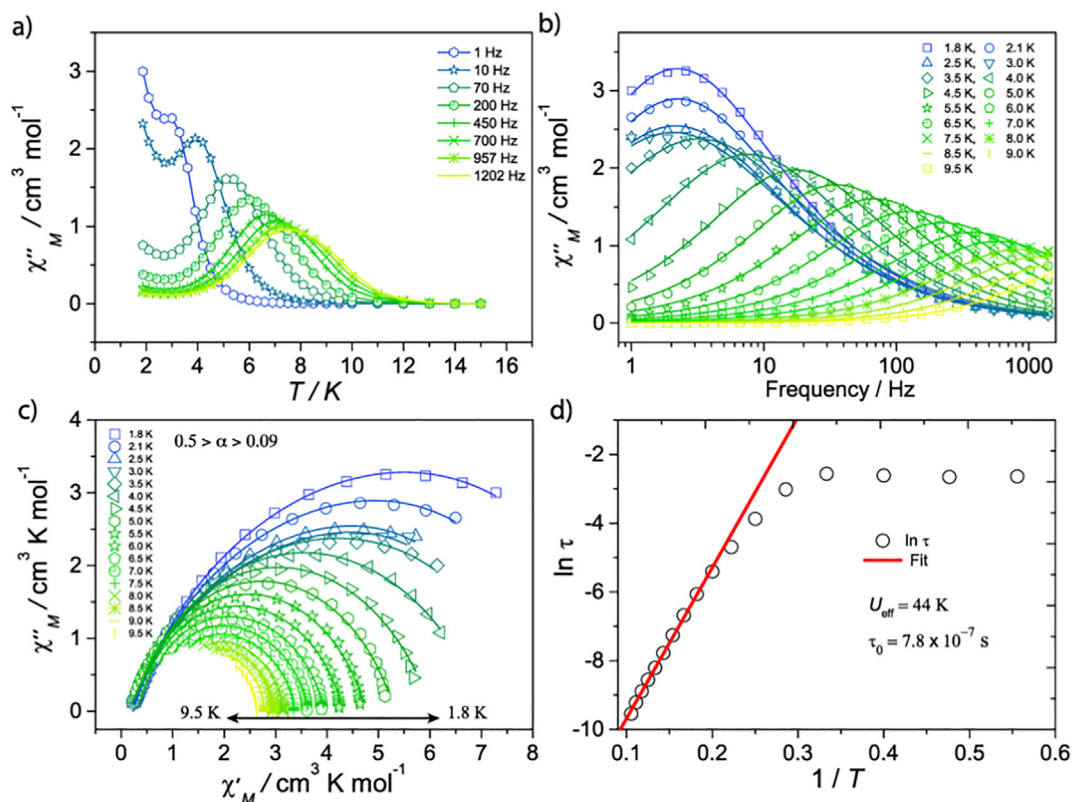
Fig. 80. (a) Plots of χ'' vs T, (b) plots of χ'' vs ν, (c) Cole-Cole plots, and (d) of ln (τ) vs T^{-1} for **89** {Mg$_2^{II}$Dy$_2$} under zero dc field. Reprinted with permission from [50]. Copyright (2015) American Chemical Society.
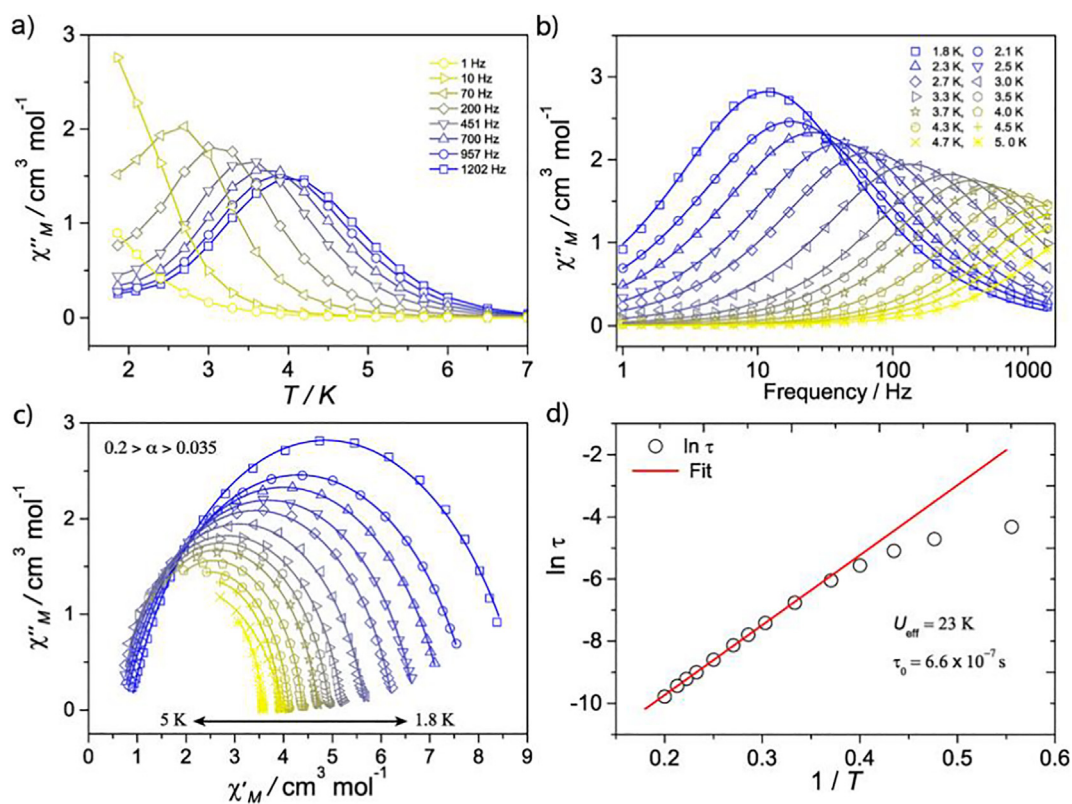
Fig. 81. (a) Plots of χ'' vs T, (b) plots of χ'' vs ν, (c) Cole-Cole plots, and (d) plots of ln (τ) vs T^{-1} for **90** {Mg$_2^{II}$Er$_2$} under 1000 dc field. Reprinted with permission from [50]. Copyright (2015) American Chemical Society.
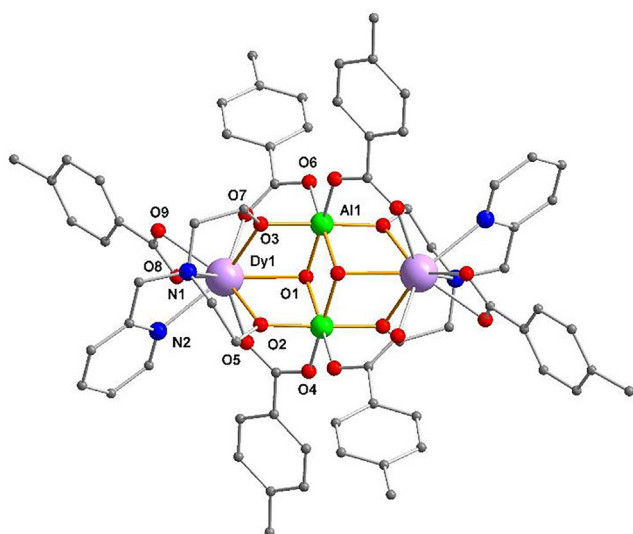
Fig. 82. Molecular structure of **91** [Al$_2^{III}$Dy$_2$(OH)$_2$(pdea)$_2$(p-Me-PhCO$_2$)$_6$].

monoclinic space group C2/c and have a similar core motif to that of the previously reported {Fe$_2^{III}$Ln$_2$} Ln = Dy **37** or Er **38** coordination clusters, and also similar to [Fe$_2^{III}$Dy$_2$(OH)$_2$(teaH)$_2$(p-Me-PhCO$_2$)$_6$] **36** with teaH$_3$ ligands of **Type I**. As shown in Fig. 82, for compound **91** the chelating alcohol arm of the triethanolamine ligand attached to the Dy centers has been replaced by a picolyl group.

Dc susceptibility measurements indicate there is a weak dipolar ferromagnetic interaction between the Dy^{III} ions indicated by *ab intio* calculations (Table 9), which is in line with the **Type I** {Zn$_2$-Dy$_2$} compounds **61–64**. Ac susceptibility measurements reveal classic SMM behavior under zero dc field with clear maxima observed in the temperature and frequency dependent χ″ data (Fig. 83a) along with QTM. At temperatures above 6 K the relaxation data is roughly linear and can be analyzed using the Arrhenius law (Fig. 83b) with a thermal energy barrier of U_{eff} = 38.7 K and τ_0 = 1.06 × 10^{-6} s under zero field (Table 8).

For compound **92**, [Al$_2^{III}$Er$_2$(OH)$_2$(pdea)$_2$(p-Me-PhCO$_2$)$_6$], dc susceptibility measurements indicate there is a weak dipolar antiferromagnetic interaction between the Er^{III} ions. Ac susceptibility measurements require an applied dc field of 1000 Oe to give maxima. It is noteworthy that the plot of ln(τ) versus T^{-1} (Fig. 84) shows a crossover at ~4 K, which indicates the presence of dual relaxation processes. A fit to the Arrhenius law, gives the effective energy barriers of U_{eff} = 4.54 K (τ_0 = 4.85 × 10^{-4} s) and U_{eff} = 28.73 K (τ_0 = 1.54 × 10^{-6} s) for low- and high-temperature dynamics, respectively. No further analysis of these data was performed for **91**. Furthermore, under dc magnetic fields over 3000 Oe, both compounds show at least two relaxation processes.

Summary: This system provides a **Type I** core example where the central trivalent *3d* ions are replaced by diamagnetic Al^{III}. The Dy^{III} ions are thus more isolated through the deletion of the paramagnetic M^{III} and the Dy^{III} single ion contribution can be seen. This allows for an ordering of influence of the nature of the trivalent *3d* ion electron configuration in the M^{III} = Cr, Mn **29**, Fe **37** analogues ([M$_2^{III}$Dy$_2$(OH)$_2$(pdea)$_2$(p-Me-PhCO$_2$)$_6$]) to be assessed in terms of
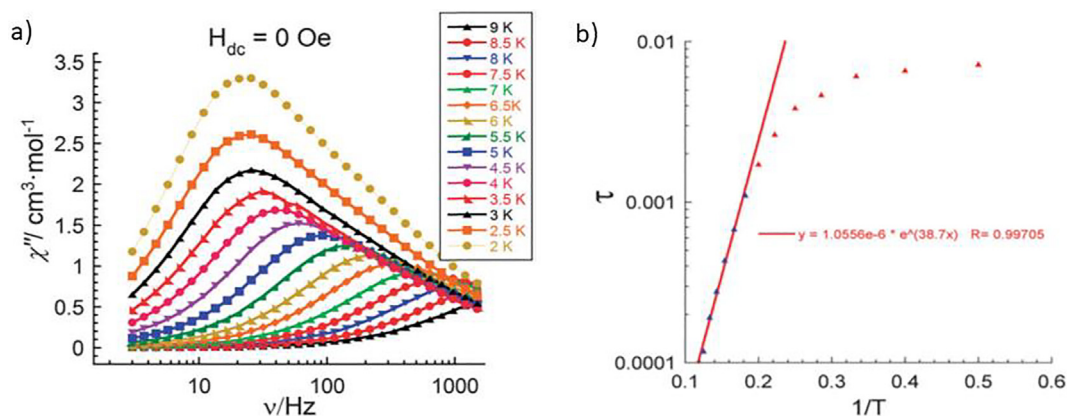
Fig. 83. Plots of χ″ vs ν (a) and plots of ln (τ) vs T^{-1} (b) for **91** {Al$_2^{III}$Dy$_2$} under zero dc field. Reprinted with permission from [25]. Copyright (2018) The Royal Society of Chemistry.
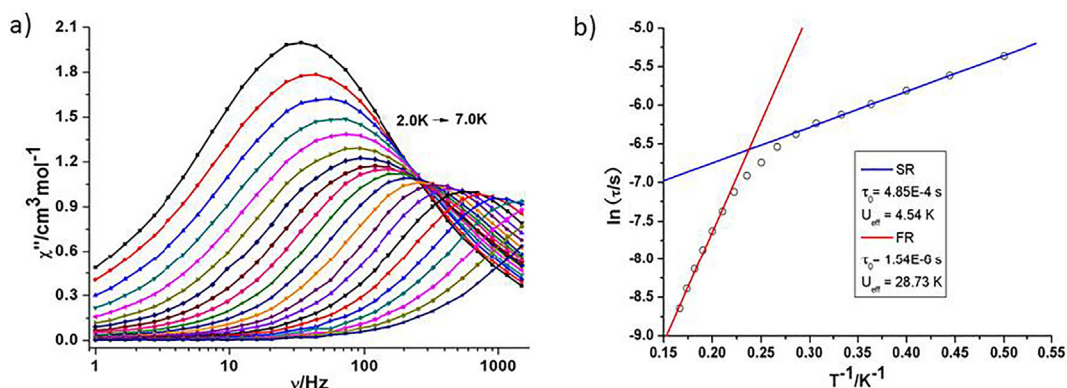
Fig. 84. Plots of χ″ vs ν (a) and plots of ln (τ) vs T^{-1} (b) for complex **92**{Al$_2^{III}$Er$_2$} under 1000 Oe dc field. Adapted with Reprinted with permission from [23]. Copyright (2018) American Chemical Society.

observed magnetic properties, backed up by *ab initio* and DFT calculations (Tables 4 and 9). An ordering of the ions as $d^4 > d^5 > d^3$ (Mn^{III}, Fe^{III}, Cr^{III}) was established in terms of observation of maxima for the out-of-phase ac signals. Note that the isostructural Cr^{III} compound does not show any slow relaxation of the magnetization. Again the Mn^{III} h.s ion also provides added value through a contribution to the overall anisotropy as a result of the axial J-T distortion.

Furthermore, in this system, in the case where Dy^{III} ions are replaced by Er^{III} the slow relaxation can only be analyzed under applied dc field. The Dy^{III}-Dy^{III} dipolar interaction is clearly ferromagnetic in **91** {$Al_2^{III}Dy_2$}, but in **92** {$Al_2^{III}Er_2$} the nature of the Er^{III}-Er^{III} interaction becomes ambiguous as was also observed in the {$Mg_2^{II}Ln$} system (Ln = Dy **89** and Er **90**).

As shown in Table 8, for the energy barrier for the {M_2Ln_2} M = diamagnetic ions system, it is possible to see the ranking of U_{eff} for all complexes with a wide range between 10 and 117.5 cm^{-1}. However, for most of the results, the dynamic magnetic data have been analyzed using only the Orbach process. It should be noted that firstly, fitting the data to a straight line can lead to errors [35]. Secondly, recent studies on relaxation processes indicate the additional relaxation mechanisms, especially the Raman process [34,82–84], can affect the energy barrier. Thus, the energy barriers for most of the reported complexes showing multiple relaxation processes but only fitted using the Orbach process are not accurate. More detailed study of relaxation mechanisms for the multiple relaxation process systems must be done.

Table 10
Summary of the available paramagnetic and diamagnetic analogues for *3d/4f* butterflies.

	Space group	Applied dc Field/ Oe	Relaxation process		Raman	direct	QTM	Ref
			Orbach					
			U_{eff}/K (cm^{-1})	τ_0/s				
[Cr$_2^{III}$Dy$_2$(OMe)$_2$(mdea)$_2$ (O$_2$CPh)$_4$(NO$_3$)$_2$] **1**	P2$_1$/n	0	77 (ca. 54)	5.1×10^{-8}	–	–	–	[32]
[Co$_2^{III}$Dy$_2$(OMe)$_2$(mdea)$_2$ (O$_2$CPh)$_4$(NO$_3$)$_2$] **78**	P2$_1$/n	0	79.1 (55)	1.03×10^{-7}	+	+	0.2	[77]
[Cr$_2^{III}$Dy$_2$(OMe)$_2$(mdea)$_2$ (acac)$_4$(NO$_3$)$_2$] **6**	P-1	0	34.6 (24)	1.2×10^{-7}	–	–	–	[36]
[Co$_2^{III}$Dy$_2$(OMe)$_2$(mdea)$_2$ (acac)$_4$(NO$_3$)$_2$] **69**	P-1	0	38 (26.4)	2.6×10^{-6}	+	+	2.5×10^{-3}	[72]
[Cr$_2^{III}$Dy$_2$(OMe)$_2$(edea)$_2$ (acac)$_4$(NO$_3$)$_2$] **7**	P-1	0	41.6 (29)	9.2×10^{-8}	–	–	–	[36]
[Cr$_2^{III}$Dy$_2$(OMe)$_2$(^{n}Budea)$_2$ (acac)$_4$(NO$_3$)$_2$] **8**	P-1	0	37.5 (26)	3.1×10^{-7}	–	–	–	[36]
[Co$_2^{III}$Dy$_2$(OMe)$_2$(teaH)$_2$ (acac)$_4$(NO$_3$)$_2$] **67**	P-1	0	27 (18.8)	8.1×10^{-6}	+	+	5.8×10^{-4}	[72]
[Co$_2^{III}$Dy$_2$(OH)$_2$(teaH)$_2$ (acac)$_4$(NO$_3$)$_2$] **68**	P2$_1$/c	0	28 (19.5)	7.4×10^{-6}	+	+	5.8×10^{-4}	[72]
[Mn$_2^{II}$Dy$_2$(L2)$_4$(NO$_3$)$_2$ (DMF)] **20**	P-1	0	11* (7.6)	1×10^{-8}*	–	–	–	[45]
[Co$_2^{II}$Dy$_2$(L2)$_4$(NO$_3$)$_2$ (DMF)$_2$] **45**	P-1	0	88.8 (61.7) 125.1$^\epsilon$ (86.8)	2.29×10^{-6} $2.67 \times 10^{-6\epsilon}$	C = 0.301 n = 3.16	–	1000	[45]
[Zn$_2^{II}$Dy$_2$(L2)$_4$(NO$_3$)$_2$ (MeOH)$_2$] **60**	P-1	0	115 (79.9)	2.35×10^{-6}	C = 0.116 n = 3.26	–	9.2×10^{-3}	[45]
[Co$_2^{II}$Dy$_2$(L1)$_4$(NO$_3$)$_2$ (MeOH)$_2$] **43**	P2$_1$/c	0	17.9 (12.4) 104.8 (72.8)	2.3×10^{-4} and 9.2×10^{-7}	–	–	–	[60]
[Ni$_2^{II}$Dy$_2$(L1)$_4$(NO$_3$)$_2$ (MeOH)$_2$] **48**	P2$_1$/c	0	21.3 (14.8)	1.5×10^{-6}	–	–	–	[61]
		4000	28.5 (19.8)	2.8×10^{-6}	–	–	–	
[Zn$_2^{II}$Dy$_2$(L1)$_4$(NO$_3$)$_2$ (MeOH)$_2$] **59**	P-1	0	140.4 (97.6)	1.4×10^{-7}	C = 2.1×10^{-2} n = 4.1	–	1.50×10^{-2}	[60]
[Et$_3$NH]$_2$[Mn$_2^{III}$Dy$_2$(O)$_2$ (piv)10] **28**	P-1	0	29 (20.2)	4.6×10^{-6}	+	+	+	[50]
[^{i}Pr$_2$NH$_2$]$_2$[Co$_2^{II}$Dy$_2$(OH)$_2$ (Piv)$_{10}$] **46**	P-1	0	–	–	–	–	–	[50]
[Et$_3$NH$_2$]$_2$[Ni$_2^{II}$Dy$_2$(OH)$_2$ (Piv)$_{10}$] **54**	C2/c	0	20 (13.9)	6×10^{-7}	+	+	+	[50]
[^{i}Pr$_2$NH$_2$]$_2$[Cu$_2^{II}$Dy$_2$(OH)$_2$ (Piv)$_{10}$] **56**	P-1	–	–	–	–	–	–	[50]
[^{i}Pr$_2$NH$_2$]$_2$[Mg$_2^{II}$Dy$_2$(OH)$_2$ (Piv)$_{10}$] **89**	P2$_1$/c	0	44 (30.6)	7.8×10^{-7}	+	+	+	[50]
[Cr$_2^{III}$Dy$_2$(OH)$_2$(pdea)$_2$ (p-Me-PhCO$_2$)$_6$]$^\#$	C2/c	0	–	–	–	–	–	[24]
[Mn$_2^{III}$Dy$_2$(OH)$_2$(pdea)$_2$ (p-Me-PhCO$_2$)$_6$] **29**	P-1	0	19.32 (13.4)	5.64×10^{-8}	–	–	–	[24]
[Fe$_2^{III}$Dy$_2$(OH)$_2$(pdea)$_2$ (p-Me-PhCO$_2$)$_6$] **37**	C2/c	1000	24.0 (16.7)	1.71×10^{-7}	–	–	–	[25]
[Al$_2^{III}$Dy$_2$(OH)$_2$(pdea)$_2$ (p-Me-PhCO$_2$)$_6$] **91**	P-1	0	38.7 (26.9)	1.06×10^{-6}	+	+	+	[25]
		1000	41.5 (28.8)	9.95×10^{-7}	+	+	+	

Lattice solvent molecules are not listed. + Means multiple relaxation processes were observed but not analyzed. – means multiple relaxation processes were not observed. $^\epsilon$ fitted only Orbach process. $\#$ means related compound for comparison. * means the energy barriers obtained by fitting the equation bellow:
$$\ln(\chi''/\chi') = \ln(\omega\tau_0) + U_{eff}/K_B T \text{ (eqn 3)}.$$

Finally, it might be instructive to try to draw direct comparisons between systems with paramagnetic 3d metal ions for which there are physical diamagnetic analogues. Candidates for such a comparison are given in Table 10. In particular, for the analogues with Cr^{III} replaced by low spin Co^{III}, the reported energy barriers are rather similar and only small contributions to the QTM are observed for the Co^{III} cases. When diamagnetic ions with full shells of 3d electrons or else no 3d electrons are used, there is an overall trend in increasing relaxation pathways compared with their paramagnetic analogues. Particularly noteworthy are the Co^{II} butterflies which can be analyzed satisfactorily in terms of two Orbach processes, whereas the Zn^{II} cases show clear QTM in the low temperature regime. This suggests that both diamagnetic l.s. Co^{III} and paramagnetic Co^{II} are effective in reducing fast and multiple relaxation processes of Dy^{III} ions and in forcing the system to surmount rather than short-circuit the overall energy barrier. Put colloquially, travelling by train from Northern Europe to, for example, Italy, is significantly easier if the option of "going over the top" has alternative tunnel routes through the Alpine barrier at lower energies.

4. Conclusion and perspective

Research into 3d-4f coordination clusters has seen rapid development in the past 15 years with the research on SMM examples progressing extensively since the first examples were identified in 2004. Although the synthesis of a wide range of 3d-4f complexes has been explored, enlarging the database of structural topologies as well as new magnetic materials, it remains a significant challenge to understand the magnetic properties of 3d-4f complexes. This relies on quantifying both the exchange and dipolar interactions between 3d and 4f ions. With improved computational facilities as well as improved understanding of how to handle evaluation of the static and dynamic magnetic properties, it is becoming increasingly helpful to support physical analysis with high level calculations to model the observed magnetic behavior. This also opens the possibility to propose magnetostructural correlations.

In present this review of 3d-4f butterflies SMMs reported prior to July 2019, we have surveyed the variation of both 3d and 4f ions as well as their position within the butterfly. The magnetic properties of 3d-4f complexes are largely dominated by the nature of metal ions as well as the symmetry of the ligand field, which in turn is tuned by the precise molecular geometry. Through conducting this review on the restricted set of 3d-4f butterflies where the core motif is always $\{M_2Ln_2(\mu_2\text{-O})_4(\mu_3\text{-OR})_2\}$, in which the position of M and Ln can be swapped between body and wing-tip positions, it is possible to draw some general conclusions regarding the state-of-the-art:

a) The coordination environments around the metal ions, the alignments of uniaxial-anisotropy axes, such as the Ising axes of Ln^{III} ions and J-T axes of Mn^{III} ions, and the exchange coupling between metal centers are the key tuning handles for the magnetic properties.
b) For most 3d-4f SMMs, the primary contribution to the slow relaxation of the magnetization is from highly anisotropic Ln^{III} ions. The direction of the easy axis of magnetization may not necessarily coincide with the obvious molecular symmetry axis. The 3d-4f interaction can also play a key role in suppressing QTM.
c) Up to now, it has proved more challenging to exert the high degree of control over local ion coordination geometry which has been achieved for the 3d-SMMs and 4f-SMMs within the 3d-4f systems.

d) It was found that in the **Type I** 3d-4f butterfly systems (Ln in wingtips) simple substitutions around the Dy^{III} ions have little influence on the barrier height. This is in contrast to the **Type II** $\{Co_2^{III}Dy_2\}$ complexes (Ln in body), in which the nature of the slow magnetic relaxation is a consequence of the single-ion Dy^{III} anisotropy being influenced by subtle changes to the ligand field.
e) Introducing electron withdrawing groups in the butterfly system can help in enhancing the magnetic properties, such as increasing the barrier height to magnetization reversal.
f) The 3d paramagnetic metal ions play an important role in determining the resulting static and dynamic magnetic properties. From *ab initio* calculations deleting the 3d contribution using diamagnetic metal ions can reduce QTM in favorable cases.
g) Clearly, the role of magnetic exchange and dipolar interactions between metal centers in 3d-4f SMMs should be further studied both experimentally and theoretically.

In conclusion, the magnetism of 3d-4f complexes is so complicated that even in a low nuclearity motif it is still challenge to gain a clear understanding of the magnetic properties. In particular, the magnetic interactions between 3d and 4f ions seems to be a key component for steering the resulting magnetic behavior. Analyzing this is made challenging as a result of the combination of 3d ions, where orbital contributions are mostly quenched, with 4f ions, where the large orbital and therefore spin–orbit coupling contributions become a dominant factor. With the continuous developing of sophisticated physical measurements and computational methods, the perspective is to gain a deeper understanding of the magnetic properties of 3d-4f SMMs which could be expected in the near future. Meanwhile, it is still necessary to gather physical data on new examples to identify the factors leading to enhanced magnetic properties as well to establish magneto-structural correlations in these fascinating systems.

References

[1] T.D. Pasatoiu, C. Tiseanu, A.M. Madalan, B. Jurca, C. Duhayon, J.P. Sutter, M. Andruh, Inorg. Chem. 50 (2011) 5879–5889.
[2] X. Yang, Z. Li, S. Wang, S. Huang, D. Schipper, R.A. Jones, Chem. Commun. 50 (2014) 15569–15572.
[3] J. Jankolovits, C.M. Andolina, J.W. Kampf, K.N. Raymond, V.L. Pecoraro, Angew. Chem., Int. Ed. 50 (2011) 9660–9664.
[4] S. Handa, V. Gnanadesikan, S. Matsunaga, M. Shibasaki, J. Am. Chem. Soc. 129 (2007) 4900–4901.
[5] K. Griffiths, G.E. Kostakis, Dalton Trans. 47 (2018) 12011–12034.
[6] G. Karotsis, M. Evangelisti, S.J. Dalgarno, E.K. Brechin, Angew. Chem., Int. Ed. 48 (2009) 9928–9931.
[7] J.-D. Leng, J.-L. Liu, M.-L. Tong, Chem. Commun. 48 (2012) 5286–5288.

[8] K.S. Pedersen, G. Lorusso, J.J. Morales, T. Weyhermüller, S. Piligkos, S.K. Singh, D. Larsen, M. Schau-Magnussen, G. Rajaraman, M. Evangelisti, J. Bendix, Angew. Chem., Int. Ed. 53 (2014) 2394–2397.

[9] J.-B. Peng, Q.-C. Zhang, X.-J. Kong, Y.-Z. Zheng, Y.-P. Ren, L.-S. Long, R.-B. Huang, L.-S. Zheng, Z. Zheng, J. Am. Chem. Soc. 134 (2012) 3314–3317.

[10] J. Masternak, M. Zienkiewicz-Machnik, M. Kowalik, A. Jabłońska-Wawrzycka, P. Rogala, A. Adach, B. Barszcz, Coord. Chem. Rev. 327–328 (2016) 242–270.

[11] K. Liu, W. Shi, P. Cheng, Coord. Chem. Rev. 289–290 (2015) 74–122.

[12] H.L.C. Feltham, S. Brooker, Coord. Chem. Rev. 276 (2014) 1–33.

[13] A. Bencini, C. Benelli, A. Caneschi, R.L. Carlin, A. Dei, D. Gatteschi, J. Am. Chem. Soc. 107 (1985) 8128–8136.

[14] S. Osa, T. Kido, N. Matsumoto, N. Re, A. Pochaba, J. Mrozinski, J. Am. Chem. Soc. 126 (2004) 420–421.

[15] Z. Zhang, Y. Zhang, Z. Zheng, Lanthanide Hydroxide Cluster Complexes via Ligand-Controlled Hydrolysis of the Lanthanide Ions, in: Z. Zheng (Ed.), Recent Development in Clusters of Rare Earths and Actinides: Chemistry and Materials, Springer Berlin Heidelberg, Berlin, Heidelberg, 2017, pp. 1–49.

[16] X.Y. Zheng, X.J. Kong, L.S. Long, Synthesis and Structures of Lanthanide-Transition Metal Clusters, in: Z. Zheng (Ed.), Recent Development in Clusters of Rare Earths and Actinides: Chemistry and Materials, Springer, New York, 2017, pp. 51–96.

[17] X.-Y. Zheng, X.-J. Kong, Z. Zheng, L.-S. Long, L.-S. Zheng, Acc. Chem. Res. 51 (2018) 517–525.

[18] M.A. Sørensen, H. Weihe, M.G. Vinum, J.S. Mortensen, L.H. Doerrer, J. Bendix, Chem. Sci. 8 (2017) 3566–3575.

[19] L. Sorace, M.E. Boulon, P. Totaro, A. Cornia, J. Fernandes-Soares, R. Sessoli, Phys. Rev. B. 88 (2013) 104407.

[20] A. Caneschi, L. Cianchi, F.D. Giallo, D. Gatteschi, P. Moretti, F. Pieralli, G. Spina, J. Condens, Matter Phys. 11 (1999) 3395–3403.

[21] O. Waldmann, G. Carver, C. Dobe, A. Sieber, H.U. Güdel, H. Mutka, J. Ollivier, N.E. Chakov, Appl. Phys. Lett. 88 (2006) 042507.

[22] K. Balinski, L. Schneider, J. Wöllermann, A. Buling, L. Joly, C. Piamonteze, H.L.C. Feltham, S. Brooker, A.K. Powell, B. Delley, K. Kuepper, Phys. Chem. Chem. Phys. 20 (2018) 21286–21293.

[23] Y. Peng, V. Mereacre, C.E. Anson, A.K. Powell, ACS Omega. 3 (2018) 6360–6368.

[24] Y. Peng, M.K. Singh, V. Mereacre, C.E. Anson, G. Rajaraman, A.K. Powell, Chem. Sci. 10 (2019) 5528–5538.

[25] Y. Peng, V. Mereacre, C.E. Anson, A.K. Powell, Phys. Chem. Chem. Phys. 18 (2016) 21469–21480.

[26] Y. Peng, A.K. Powell, in review.

[27] S. Alvarez, D. Avnir, M. Llunell, M. Pinsky, New J. Chem. 26 (2002) 996–1009.

[28] D. Casanova, P. Alemany, J.M. Bofill, S. Alvarez, Chem. Eur. J. 9 (2003) 1281–1295.

[29] S. Alvarez, P. Alemany, D. Casanova, J. Cirera, M. Llunell, D. Avnir, Coord. Chem. Rev. 249 (2005) 1693–1708.

[30] A. Amjad, A. Figuerola, L. Sorace, Dalton Trans. 46 (2017) 3848–3856.

[31] K.S. Cole, R.H. Cole, J. Chem. Phy. 9 (1941) 341–351.

[32] S.K. Langley, D.P. Wielechowski, V. Vieru, N.F. Chilton, B. Moubaraki, B.F. Abrahams, L.F. Chibotaru, K.S. Murray, Angew. Chem., Int. Ed. 52 (2013) 12014–12019.

[33] S.K. Langley, D.P. Wielechowski, B. Moubaraki, B.F. Abrahams, K.S. Murray, Aust. J. Chem. 67 (2014) 1581–1587.

[34] A.K. Boudalis, Quantum. Mater. Res. 1 (2020) e200004.

[35] C. Lampropoulos, S. Hill, G. Christou, ChemPhysChem 10 (2009) 2397–2400.

[36] S.K. Langley, D.P. Wielechowski, V. Vieru, N.F. Chilton, B. Moubaraki, L.F. Chibotaru, K.S. Murray, Chem. Sci. 5 (2014) 3246–3256.

[37] S.K. Langley, D.P. Wielechowski, N.F. Chilton, B. Moubaraki, K.S. Murray, Inorg. Chem. 54 (2015) 10497–10503.

[38] J.D. Rinehart, J.R. Long, Dalton Trans. 41 (2012) 13572–13574.

[39] J. Vallejo, A. Pascual-Álvarez, J. Cano, I. Castro, M. Julve, F. Lloret, J. Krzystek, G. De Munno, D. Armentano, W. Wernsdorfer, R. Ruiz-García, E. Pardo, Angew. Chem., Int. Ed. 52 (2013) 14075–14079.

[40] J.M. Zadrozny, D.J. Xiao, M. Atanasov, G.J. Long, F. Grandjean, F. Neese, J.R. Long, Nat. Chem. 5 (2013) 577.

[41] S.K. Langley, D.P. Wielechowski, B. Moubaraki, K.S. Murray, Chem. Commun. 52 (2016) 10976–10979.

[42] V. Mereacre, A. Baniodeh, C.E. Anson, A.K. Powell, J. Am. Chem. Soc. 133 (2011) 15335–15337.

[43] S.K. Langley, C. Le, L. Ungur, B. Moubaraki, B.F. Abrahams, L.F. Chibotaru, K.S. Murray, Inorg. Chem. 54 (2015) 3631–3642.

[44] L. Sun, H. Chen, C. Ma, C. Chen, Inorg. Chem. Commun. 70 (2016) 132–135.

[45] J. Li, R.-M. Wei, T.-C. Pu, F. Cao, L. Yang, Y. Han, Y.-Q. Zhang, J.-L. Zuo, Y. Song, Inorg. Chem. Front. 4 (2017) 114–122.

[46] A. Mishra, W. Wernsdorfer, S. Parsons, G. Christou, E.K. Brechin, Chem. Commun. (2005) 2086–2088.

[47] M.N. Akhtar, Y. Lan, V. Mereacre, R. Clérac, C.E. Anson, A.K. Powell, Polyhedron 28 (2009) 1698–1703.

[48] C. Papatriantafyllopoulou, K.A. Abboud, G. Christou, Inorg. Chem. 50 (2011) 8959–8966.

[49] G.P. Guedes, S. Soriano, L.A. Mercante, N.L. Speziali, M.A. Novak, M. Andruh, M. G.F. Vaz, Inorg. Chem. 52 (2013) 8309–8311.

[50] E. Moreno Pineda, N.F. Chilton, F. Tuna, R.E.P. Winpenny, E.J.L. McInnes, Inorg. Chem. 54 (2015) 5930–5941.

[51] L. Lecren, W. Wernsdorfer, Y.-G. Li, O. Roubeau, H. Miyasaka, R. Clérac, J. Am. Chem. Soc. 127 (2005) 11311–11317.

[52] M. Murugesu, A. Mishra, W. Wernsdorfer, K.A. Abboud, G. Christou, Polyhedron. 25 (2006) 613–625.

[53] A. Baniodeh, Y. Lan, G. Novitchi, V. Mereacre, A. Sukhanov, M. Ferbinteanu, V. Voronkova, C.E. Anson, A.K. Powell, Dalton Trans. 42 (2013) 8926–8938.

[54] A. Baniodeh, V. Mereacre, N. Magnani, Y. Lan, J.A. Wolny, V. Schünemann, C.E. Anson, A.K. Powell, Chem. Commun. 49 (2013) 9666–9668.

[55] V. Vieru, L. Ungur, V. Cemortan, A. Sukhanov, A. Baniodeh, C.E. Anson, A.K. Powell, V. Voronkova, L.F. Chibotaru, Chem. Eur. J. 24 (2018) 16652–16661.

[56] G. Peng, V. Mereacre, G.E. Kostakis, J.A. Wolny, V. Schünemann, A.K. Powell, Chem. Eur. J. 20 (2014) 12381–12384.

[57] H. Xiang, V. Mereacre, Y. Lan, T.-B. Lu, C.E. Anson, A.K. Powell, Chem. Commun. 49 (2013) 7385–7387.

[58] J.-P. Costes, L. Vendier, W. Wernsdorfer, Dalton Trans. 40 (2011) 1700–1706.

[59] K.C. Mondal, A. Sundt, Y. Lan, G.E. Kostakis, O. Waldmann, L. Ungur, L.F. Chibotaru, C.E. Anson, A.K. Powell, Angew. Chem., Int. Ed. 51 (2012) 7550–7554.

[60] Y. Peng, V. Mereacre, C.E. Anson, A.K. Powell, Dalton Trans. 46 (2017) 5337–5343.

[61] K.C. Mondal, G.E. Kostakis, Y. Lan, W. Wernsdorfer, C.E. Anson, A.K. Powell, Inorg. Chem. 50 (2011) 11604–11611.

[62] S. Mandal, S. Ghosh, D. Takahashi, G. Christou, S. Mohanta, Eur. J. Inorg. Chem. 2018 (2018) 2793–2804.

[63] H.-H. Zou, L.-B. Sheng, F.-P. Liang, Z.-L. Chen, Y.-Q. Zhang, Dalton Trans. 44 (2015) 18544–18552.

[64] I.A. Kühne, K. Griffiths, A.-J. Hutchings, O.P.E. Townrow, A. Eichhöfer, C.E. Anson, G.E. Kostakis, A.K. Powell, Cryst. Growth Des. 17 (2017) 5178–5190.

[65] D.N. Woodruff, R.E.P. Winpenny, R.A. Layfield, Chem. Rev. 113 (2013) 5110–5148.

[66] P. Zhang, Y.-N. Guo, J. Tang, Coord. Chem. Rev. 257 (2013) 1728–1763.

[67] P. Zhang, L. Zhang, J. Tang, Dalton Trans. 44 (2015) 3923–3929.

[68] J.-L. Liu, Y.-C. Chen, M.-L. Tong, Chem. Soc. Rev. 47 (2018) 2431–2453.

[69] H. Ke, W. Wei, Y. Yang, J. Zhang, Y.Q. Zhang, G. Xie, S. Chen, Dalton Trans 48 (2019) 7844–7852.

[70] H. Ke, W. Wei, Y.-Q. Zhang, J. Zhang, G. Xie, S. Chen, Dalton Trans. 47 (2018) 16616–16626.

[71] S.K. Langley, N.F. Chilton, L. Ungur, B. Moubaraki, L.F. Chibotaru, K.S. Murray, Inorg. Chem. 51 (2012) (1881) 11873–11875.

[72] S.K. Langley, N.F. Chilton, B. Moubaraki, K.S. Murray, Inorg. Chem. 52 (2013) 7183–7192.

[73] S.K. Langley, N.F. Chilton, B. Moubaraki, K.S. Murray, Chem. Commun. 49 (2013) 6965–6967.

[74] A.V. Funes, L. Carrella, E. Rentschler, P. Alborés, Dalton Trans. 43 (2014) 2361–2364.

[75] A.V. Funes, L. Carrella, E. Rentschler, P. Alborés, Chem. Eur. J. 22 (2016) 14308–14318.

[76] A.V. Funes, L. Carrella, Y. Rechkemmer, J. van Slageren, E. Rentschler, P. Alborés, Dalton Trans. 46 (2017) 3400–3409.

[77] S.K. Langley, L. Ungur, N.F. Chilton, B. Moubaraki, L.F. Chibotaru, K.S. Murray, Inorg. Chem. 53 (2014) 4303–4315.

[78] S.K. Langley, N.F. Chilton, B. Moubaraki, K.S. Murray, Inorg. Chem. Front. 2 (2015) 867–875.

[79] K.R. Vignesh, S.K. Langley, K.S. Murray, G. Rajaraman, Inorg. Chem. 56 (2017) 2518–2532.

[80] F. Habib, G. Brunet, V. Vieru, I. Korobkov, L.F. Chibotaru, M. Murugesu, J. Am. Chem. Soc. 135 (2013) 13242–13245.

[81] M.E. Lines, J. Chem. Phy. 55 (1971) 2977–2984.

[82] D. Reta, N.F. Chilton, Phys. Chem. Chem. Phys. 21 (2019) 23567–23575.

[83] V.S. Parmar, F. Ortu, X. Ma, N.F. Chilton, R. Clérac, D.P. Mills, R.E.P. Winpenny, Chem. Eur. J. 26 (2020) 7774–7778.

[84] Y.-S. Ding, T. Han, Y.-Q. Zhai, D. Reta, N.F. Chilton, R.E.P. Winpenny, Y.-Z. Zheng, Chem. Eur. J. 26 (2020) 5893–5902.